FACULTÉ DES SCIENCES
DÉPARTEMENT DE PHYSIQUE - UNITÉ DE RECHERCHE CESAM
GROUP FOR RESEARCH AND APPLICATIONS IN STATISTICAL PHYSICS

Self-assembly of superparamagnetic colloids induced by a rotating magnetic field

DISSERTATION PRÉSENTÉE PAR

FLORENCE MIGNOLET

EN VUE DE L'OBTENTION DU TITRE DE
DOCTEUR EN SCIENCES PHYSIQUES

ANNÉE ACADÉMIQUE 2024-2025

Jury Members

Dr. Eric Bousquet	President
Dr. Stéphane Dorbolo	Secretary
Pr. Geoffroy Lumay	Supervisor
Pr. Anke Lindner	
Dr. Alexis Darras	
Dr. François Damanet	

Acknowledgments

Je tiens par ces quelques lignes à remercier les membres de mon jury, Eric Bousquet, Stéphane Dolorbo, Anke Lindner, Alexis Darras, François Damanet, et mon promoteur, Geoffroy Lumay. Merci de prendre le temps de lire ma thèse, et de faire partie de mon jury ! J'espère que vous passerez un moment agréable et instructif en ma compagnie.

J'aimerais spécialement profiter de cet espace pour souligner le rôle essentiel de mon promoteur, Geoffroy. Toujours présent, il a su allier prévenance et suivi régulier, tout en me laissant beaucoup d'indépendance et de libertés. Ce n'était pourtant pas chose facile, au cours des ces années entrecoupées par la crise du Covid. Quand j'étais démotivée, tu as su trouver de nouveaux projets pour me donner un nouveau souffle et réveiller mon enthousiasme; Quand je manquais de confiance en moi, tu as su me soutenir; Quand je me perdais dans ce qu'il me restait à faire, tu as su m'encourager et me guider. Pour tout ça, je te remercie tout particulièrement.

J'en profite également pour remercier Alexis, avec qui j'ai eu la chance de travailler au début de ma thèse, et avec qui nous avons continué de collaborer après son départ. Ta bienveillance et ton esprit scientifique aiguisé m'auront beaucoup apporté, et j'espère que tu pourras continuer à en faire profiter d'autres jeunes doctorants.

Ces années qui m'ont vues évoluer au sein du troisième étage du B5a resteront à jamais fondatrices, et je mesure la chance que j'ai eue de tomber sur de si formidables collègues. J'ai d'abord débarqué avec mes deux co-Super Nanas, Ylo et Jo, toute fringante et innocente (pour ma part en tout cas), et l'accueil nous a tout de suite mises à l'aise. Merci donc à Ylo pour ses muscles saillants, son sens de la fête et sa magnifique lampe à mon effigie (je sais que c'était un travail d'équipe mais c'est ta tête quand je suis rentrée dans votre bureau dont je me souviendrai haha). Merci à Galien pour m'avoir introduite à l'art du montage photo, à Gimp et aux groupes de fans de loups et d'indiens. Merci aussi d'avoir loué ce château gonflable inoubliable, et d'avoir permis à Geoffroy d'entamer en beauté notre collaboration en me jetant une patate à la figure lors de ta raclette de thèse. Merci à Martin pour son humour inimitable, son amour du vert et sa flemme légendaire. Tu resteras à jamais le champion des arrivées tardives, je m'incline respectueusement. Merci à Floriane pour son sarcasme percutant, son sens de l'esthétique inimitable, son soutient indéfectible et son talent au crossfit. Notre "maman" de la physique (tu n'étais pas si vieille que ça tout de même) ! Merci à tous pour les vendredis après-midis à jouer à Overcooked, à Worms, ou au pictionnary (j'en profite pour rappeler le dauphin d'Ylona, c'est cadeau). Merci aussi à Julien, Martial, Maxime, Salvatore, Alain, Jean-Yves, Eric, et à tous ceux qui ont su nous faire une place au sein de l'étage.

Parmi tout ces collègues, certains sont devenus des amis sans qui je n'imagine plus aller au restaurant désormais. Merci donc à Jean pour son flegme caractéristique qui nous fait toujours relativiser, son humour parfois involontaire mais efficace (la plupart du temps), pour toutes ses plantes mais surtout son magnifique jardin zen. Merci à Charlotte, notre grand soleil, merci pour ton sourire, ta chaleur, tes rires. Un grand merci à Joséphine, avec qui j'ai pu partager toutes les étapes de mon parcours universitaire, de la première année de bachelier à l'ultime semaine de notre thèse, que l'on présente à quelques semaines d'intervalle. Merci d'être toujours présente pour chanter à tue-tête avec moi sur de la chanson française, merci pour ton grain de folie et ta joie de vivre ! Merci pour tes flèches assassines à Kintargo et ton talent pour la menuiserie sur le chemin du Tian Xia. Et enfin, félicitations pour ta thèse (oui je m'avance un peu mais je suis sûre que la défense sera géniale) ! On pourra dire "On l'a fait bordel !". Enfin, merci à mon irremplaçable collègue de bureau, Sébastien. On aura insisté jusqu'au bout pour rester ensemble, pour pouvoir passer plus de temps à discuter qu'à vraiment travailler, et pour s'amuser à éteindre notre magnifique soufflerie. Merci pour toutes les discussions, scientifiques ou non, merci d'avoir répondu à toutes mes questions, merci de m'avoir donné confiance en moi dans des moments où je remettais tout en question. Merci pour les verres du vendredi après-midi (et tous les autres, oups). Merci pour ta relecture de certains chapitres, qui ont su me rassurer, et pour ton avis toujours précis autant au niveau esthétique que scientifique. A toutes et à tous, je vous souhaite de grandes et belles choses dans le futur.

Arrivent enfin les ”nouveaux”, Nicolas, Nathan, Megan, Adrien, Mattéo, Cyril et Thomas (oui je vous mets tous dans le même sac car vous êtes plus jeunes). Merci d'avoir rendu mes dernières années si vivantes et de m'avoir donné envie de venir au bureau le matin ! Merci particulièrement à mon dernier collègue de bureau, Nico, que j'ai pris plaisir à ennuyer avec les perles des mes élèves ou avec les dédales administratifs universitaires. Courage, Gabriel va finir par arriver ! Merci à Cyril pour le vent de fraîcheur qu'il nous a apporté, et courage pour supporter Thomas tout le temps qu'il te reste. Merci à Thomas de nous avoir initié au Pedantix, malgré le peu de talent qu'il y a montré (sérieusement, Tian'anmen ??).

J'aimerais aussi remercier Stephen, toujours plein d'imagination, toujours prêt à boire un verre, toujours une blague à la bouche. J'espère que j'ai bien écrit ton nom cette fois. Merci aussi à Hervé, qui m'aura beaucoup inspirée sur le plan scientifique mais aussi pédagogique, et qui m'impressionne dans sa gestion des chats errants de l'aquarium. Merci à l'atelier, pour les vendredis après-midis mais aussi pour votre expertise précieuse.

En-dehors du troisième étage, il y avait des gens bien aussi, je vous rassure. Je pense notamment à Christophe, qui nous a fait profiter de toutes ses indiscrétions croustillantes sur les affaires de l'université (fais attention aux ulcères tout de même), mais qui m'a aussi ouvert le monde du jeu de rôle. J'avoue qu'un petit TGCM aurait bien été utile à certains moments dans la rédaction de cette thèse, mais ça avait peu de chance de passer malheureusement ... Je pense aussi à Jacqueline, qui s'occupait si bien de nous, et qui profite désormais d'une retraite bien méritée. Merci à Christelle, Anne, Chouaib et tous les autres, qui ont contribué à faire de mon passage à l'Université de Liège ce qu'il a été. Je pense enfin à tous ceux que j'ai peut-être oublié de citer, mais qui restent au chaud dans mes souvenirs.

En-dehors de l'université, ils ont aussi été nombreux à me soutenir et à m'encourager.

Je pense forcément tout d'abord à mon époux, Alex, qui m'aura ”supportée” dans le sens français et surtout anglais du terme. Pas facile de gérer mes périodes de concentration intense, quand je suis hermétique à toute perturbation extérieure (oui, la perturbation c'était toi, désolée). Pas facile de gérer le stress de la fin de rédaction, quand toutes les deadlines convergent et que la fin se concrétise. Tu sais l'amour que je te porte, et l'enthousiasme que je ressens à l'idée de ces nouvelles portes qui s'ouvrent dans nos vies maintenant que je passe à une autre étape de ma vie professionnelle.

Ce stress et cette concentration, je sais que les membres de ma famille ont aussi eu la chance de les expérimenter. Désolée ! Et merci d'être toujours à mes côtés, merci de me soutenir, d'être toujours si aimants. Merci d'être si fiers de moi. Merci Maman, Papa, Juju, Antoine, Gene et Eva. Peut-être bientôt deux docteurs dans la famille hehe ! Je vous aime plus que tout.

Pour décompresser et me confier, j'ai aussi la chance d'avoir un groupe d'amies incroyables, qui sont là depuis tant d'années maintenant. Merci donc aux Bestiiies ! Merci pour toutes les soirées de folie, les chapis, les petits américains à 7h du matin alors que ”toi tu vas à l'école, moi je vais dormir!”. Merci pour les nouvels ans, merci pour les fêtes au CJBB, pour les balades covid, les voyages, les week-ends, et tout le reste. Merci pour toutes nos conversations, pour votre écoute, pour votre compréhension. On m'aurait dit quand j'étais adolescente que j'aurai une telle place dans un tel groupe, je n'y aurais jamais cru, donc merci de m'avoir fait cette place. Merci Manon, Julie, Jessica, Marie, Aurou, Claire et Valérie. Merci aussi à Tup, qui sait combien elle est chère à mon cœur, et à quel point notre amitié compte pour moi.

Je garde avec moi pour tout le reste de ma vie la trace de ces relations précieuses qui m'ont forgées et ont fait de moi la personne que je suis. MERCI A VOUS !!

Contents

Abstract

If you asked someone on the street about magnetism, they might claim to know little about it. Yet, we all rely on magnets in our daily lives, from swiping a credit card to listening to music on speakers or hanging a picture on the fridge. Beyond these familiar solid magnets, magnetism can also be harnessed in fluids, which are used in applications such as medical devices and dynamic seals. Since melting solid magnets to create magnetic fluids is not an option, magnetic control is achieved by suspending microscopic particles in a fluid, resulting in suspensions like superparamagnetic colloids.

Superparamagnetic colloids are microscopic particles suspended in a fluid, typically water, that remain non-magnetic until an external magnetic field is applied. Under such fields, the particles exhibit magnetic behavior, causing them to form structures that depend on the characteristics of the magnetic field. In two-dimensional systems, with a rotating uniform magnetic field, particles align in chains that rotate at low speeds. As the field's rotational speed increases, disk-like clusters form due to isotropic interactions. Focusing experimentally on the early stages of this aggregation process, we model the transition between these structures, revealing its dependence on the magnetic field's frequency and the colloidal suspension's volume fraction. In three-dimensional systems, these microscopic structures impact macroscopic processes such as sedimentation. From macroscopic observations, we establish that similar aggregates likely form in these conditions, and that the rotational speed of the magnetic field significantly influences the sedimentation rate. Additionally, we identify three distinct regimes corresponding to different sedimentation behaviors.

By understanding these fundamental mechanisms, we hope to open the door for developing advanced systems for applications such as fluid mixing, pollutant capture, or targeted drug delivery.

Résumé

Si vous arrêtez une personne lambda dans la rue pour lui parler de magnétisme, il vous répondra très certainement qu'il n'y connaît rien. Pourtant, nous utilisons tous des aimants au quotidien, que ce soit en utilisant notre carte de crédit, en écoutant de la musique sur des haut-parleurs ou en accrochant des photos sur la porte de notre frigo. Au-delà de ces aimants solides familiers, le magnétisme s'utilise également sous forme liquide, dans les IRM par exemple, ou encore pour créer des joints d'étanchéité dynamiques. Puisque faire fondre des aimants solides pour créer des fluides magnétiques n'est pas envisageable, on utilise des particules microscopiques en suspension dans un fluide, par exemple des colloïdes superparamagnétiques.

Ces colloïdes acquièrent des caractéristiques magnétiques quand on leur applique un champ magnétique extérieur, ce qui les amène à former des structures dont la forme dépend du champ. En 2D et avec un champ magnétique uniforme en rotation, les particules s'alignent et forment des chaînes qui tournent à faible vitesse avec le champ. À mesure que la vitesse de rotation du champ augmente, des agrégats circulaires apparaîssent en raison du caractère isotropique de leurs interactions. Une étude expérimentale de ce processus d'agrégation nous a permis de modéliser la transition entre ces structures, révélant l'influence de la fréquence du champ magnétique ainsi que de la fraction volumique. En 3D, ces structures microscopiques influencent les processus macroscopiques tels que la sédimentation. Nos expériences montrent que des agrégats similaires se forment probablement dans ces conditions et que la vitesse de rotation du champ magnétique influence considérablement le temps de sédimentation. De plus, nous distinguons trois régimes de fréquence correspondant à différents modes de sédimentation.

En étudiant ces mécanismes fondamentaux, nous espérons ouvrir la voie au développement de nouvelles applications telles que le mélange de fluides, la capture de polluants ou la délivrance ciblée de médicaments.

Publications

This thesis is based on work that has been peer-reviewed and published, as well as on another that is in preparation. They are listed below:

F. Mignolet, A. Darras, and G. Lumay. *Superparamagnetic colloids in a rotating field: Transition state from chains to disks.* Phys. Rev. E **106**, 2022.

A. Darras, F. Mignolet, N. Vandewalle, and G. Lumay. *Remote-controlled deposit of superparamagnetic colloidal droplets.* Phys. Rev. E **98**, 2018.

1

Introduction

From stone sools to tiny robots

As you begin to read this thesis, take a moment to reflect on the day that has led you here. Whether you are sitting at a desk or perhaps commuting on public transport, you have already interacted with numerous tools, often without even thinking about it. From the alarm clock that woke you up this morning to the the computer you may be using to read these lines, your day has been shaped by tools designed to extend your abilities, making your tasks more manageable.

You likely started your day by brushing your teeth with a toothbrush, then perhaps brew some coffee with a machine. You may have traveled to work by car or on a bike, possibly guided by a GPS on your phone. Each of these tools is designed to simplify or optimize daily activities. These objects, seamlessly integrated into our lives, are the result of humanity's long history of tool development, which has driven our progress for millennia. Humanity's use of tools has indeed shaped our civilization, transforming how we live, work, and interact with the environment. From the simplest stone tool made by Homo Habilis to the advanced smartphones of today, tools have been at the core of human progress.

The first tools crafted by our prehistoric ancestors [1, 2] were notably made of stone, and designed to accomplish tasks that were difficult or impossible with bare hands alone, such as hunting or cutting (with handaxes or sharp stone flakes). These evolved into more complex tools requiring other tools for their fabrication, such as spears or scrapers, and incorporated materials like bone or ivory. The concept of ”tool” extends beyond utility, as they also played a crucial role in the development of art and culture. For instance, musical instruments dating back 35,000 years have been discovered, highlighting the cultural significance of early tools [3].

Figure 1.1: Prehistoric tools and musical instruments. On the left, acheulan handaxes from Kent. On the right, bone flutes of nearly 9000 years old found in China modified from [3].

As human society advanced, so did our tools. From axes and scrappers, we moved to engines and mechanical machines during the industrial revolution. This marked a pivotal shift, as those machines could perform tasks faster and more accurately than ever before. This era saw the emergence of the concept of automation, where machines began to replace human labour rather than simply assist it. This concepts gave rise to a new kinf of tool: **robots**.

Initially popularized in science fiction, such as in the works of Isaac Asimov [4], robots made their industrial debut in the early 1950s when George C. Devol invented Unimate. This robot, first used on a General Motors assembly line in 1961, was designed to **mimic a human arm**, only stronger and tireless. As robots evolved, these machines revolutionized industries, particularly manufacturing, by taking over repetitive, dangerous, or highly precise tasks. Beyond industry, robots have found applications in surprising areas, such as medicine, where they are used as sophisticated prosthetic limbs for instance [5–8].

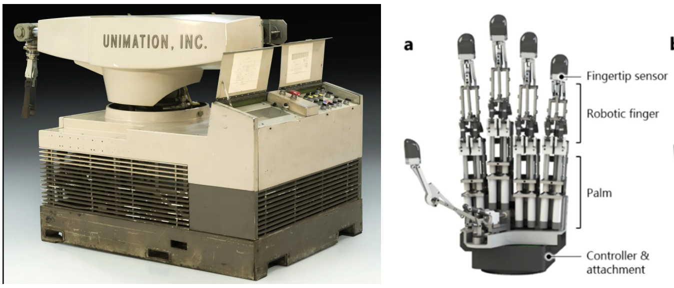

Figure 1.2: Robot inspired by the human body. On the left, first Unimate robot ever installed on an assembly line in 1961, from the Collections of The Henry Ford. On the right, a recent (2021) anthropomorphic robotic hand [8].

As robotics technology progressed, engineers began to look beyond human anatomy for inspiration, turning their attention to the animal kingdom [9–11]. This led to the emergence of **bio-inspired robotics**. Animals move efficiently in a variety of different environments, adapting to specific challenges. Depending on the species and context, they can run, slither, climb, jump, fly, or swim, and so can bio-inspired robots. These robots expanded the potential of robotics, enabling machines to operate in environments that were previously thought to be inaccessible, from disaster zones to the surface of Mars. Understanding the complex movements of animals and replicating them with machines is thus a hot topic in contemporary research [12–14].

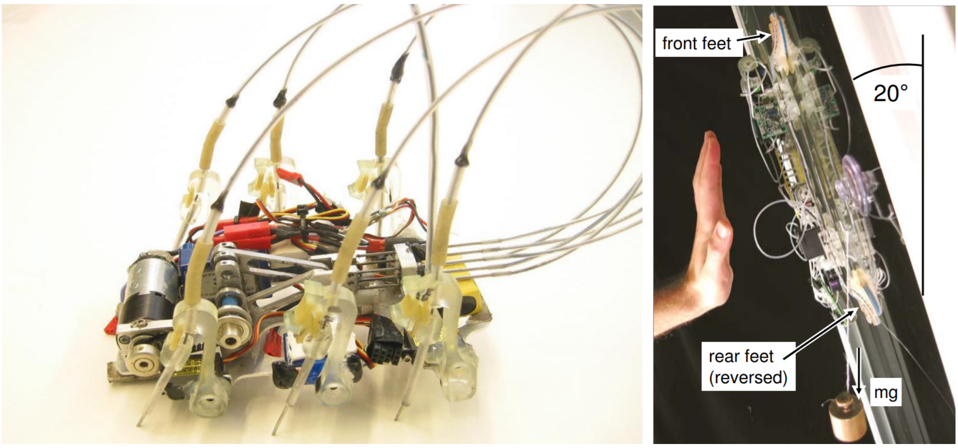

Figure 1.3: Robot inspired by the animal kingdom. On the left, iSprawl, a small autonomous hexapod inspired from running cockroaches, driven by an electric motor and flexible push-pull cables [10]. On the right, StickyBot, a robot using frictional adhesion inspired by gecko lizards, able to climb vertical walls [11].

However, the most exciting frontier of robotics today lies at the **microscopic** and **nanoscopic** scales. Indeed, after modeling robots on human limbs and animal locomotion, the latest generation of robots draws inspiration from bacteria and other microorganisms [15–22]. These tiny robots operate at a scale that allows them to navigate within the human body, capture small impurities, or monitor the environment. This could allow such robots to deliver drugs directly to corrupted cells, perform minimally invasive surgeries, or to detect and neutralize microscopic pollutants for instance.

To achieve these goals, **colloids** appear to be outstanding candidates. Colloids consist of a mixture of two phases, one continuous containing another dispersed phase, either in solid, liquid, or gaseous states. For a mixture to be classified as a colloid, the size of the dispersed phase should be around the micrometer.

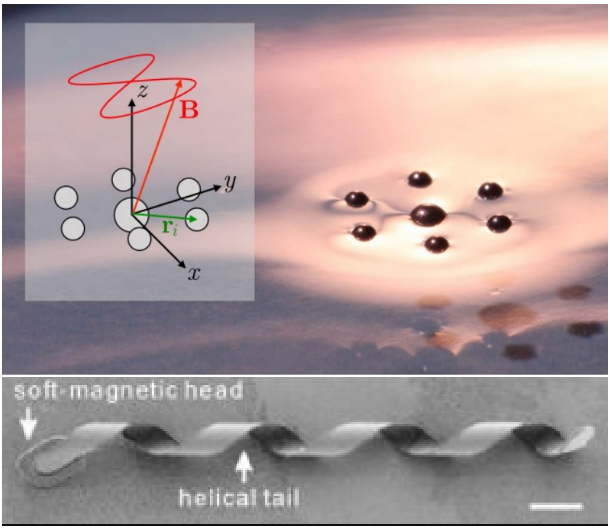

Figure 1.4: Micro-robots inspired by microorganisms. On the left, assembly of micrometric magnetic beads at the water-air interface manipulated with a magnetic field $\vec{B}$, reproducing the metachronal waves used by ciliates for locomotion [17]. On the right, an artificial flagella controlled by magnetic fields and inspired by bacterial flagella [16].

Examples include blood, which is composed of plasma (a continuous liquid phase) and red blood cells (a dispersed solid phase) measuring less than 10 µm, or milk, an emulsion of liquid fat globules dispersed in water. Inks, paints, fogs, clouds, coffee, wine, foam rubber, whipped cream, ... The examples from every day life are countless [23]. Their size and commonness make them ideal for uses in biological systems, in addition to the possibility to control them externally, for instance with magnetic or electric fields. This remote control can lead to **self-assembly** of complex structures and **locomotion** [22, 24–27]. Understanding the challenges of such control is thus crucial in order to further develop micro-robots [28–31].

In this thesis, we experimentally explore the interactions and the resulting microscopic structures of magnetic colloids controlled by an external magnetic field, as well as their repercussions on the macroscopic scale. The dispersed phase of this one-of-a-kind colloid consist of superparamagnetic particles, which are highly responsive to external magnetic fields.

In Chapter 2, we begin by introducing the fundamentals of magnetism in the context of magnetic colloids dispersed in water, before detailing the effective interactions between the magnetic particles. Chapter 3 then describe the **microscopic structures** that arise in two dimensions due to the application of both constant and time-varying magnetic fields. In this specific case, we unveil through experiments a **transition phase** between two distinct structures and relate these microscopic structures to **three-dimensional macroscopic effects**, such as sedimentation.

More precisely, we start in Chapter 5 by conducting experiments in 2D systems at the **microscopic scale** in order to characterize the influence of the magnetic field **rotational frequency** and the colloidal **volume fraction** on the microscopic structures. We focus on the early-stage of the clusters aggregation and identify a transition phase between two expected structures.

We then examine the **macroscopic 3D effects** of this microscopic aggregation with respect to sedimentation. After introducing the state of the art regarding colloidal 3D assemblies and sedimentation in Chapter 4, we present our findings in Chapter 6. Notably, we show that the sedimentation time increases with the magnetic field rotational frequency, and we draw strong parallels between the microstructures observed in 2D and their macroscopic effect on sedimentation.

For those eager to preview the results, an accompanying visual card summarizes both the 2D and 3D structures, along with the applied magnetic field and its characteristics, as well as the resulting macroscopic effects. The front side of the card provides an overview of the existing knowledge prior to this thesis, while the reverse side highlights its contributions.

2

Magnets and Fluids

A journey between ferrofluids and magnetic colloids

Most of us are used to play with small magnets, for instance to display pictures and notes on fridges or whiteboards. While this is a fairly noticeable way to use them, they also play a more subtle role in various other common devices like credit card stripes, door catches, or loudspeakers. All these magnets share a fundamental characteristic : their solid state. But would it be useful to design fluid magnets, and if so, by what means could it be achieved ?

Magnets are particularly fun to play with, mainly because their motion can be controlled without direct contact, using another magnet. This feature makes them extremely interesting to physicists, since it opens up the perspective of externally controlled interactions. It also makes them quite useful, in the mechanical field for example. However, certain situations require a flexible material, to prevent the obstruction of internal motions or to be injected in the human body for instance, leading to the idea of a magnetic fluid [32–35]. Such fluids can commonly be used as dynamic seals [33, 34, 36, 37], hermetically sealing a hole while allowing the passage of a rotation axis, as seen in computers hard disks. On the medical side, these fluids can also be employed to target specific areas when injecting drugs, confining chemotherapy drugs in a cancerous tumor [33, 35, 37]. The answer to the earlier question ”Would it be useful to design a liquid magnet?” thus appear to be a resounding **”Yes”**.

The remaining question is how to achieve it. Natural magnets are mostly made of metals [1], which are solid at room temperature, implying the need of a phase transition in order to reach the goal of a liquid magnet. This is highly problematic, given the fact that the solid to liquid transition for metals occurs at high temperatures, and those temperatures always exceed the Curie temperature. Once the Curie temperature is exceeded, the magnetic properties of the object are greatly affected, as described here after in section 3, implying the non-existence of magnetic homogeneous liquid. Furthermore, even if this where not the case, using molten metal for a medical application - or for any other application actually - would not be practical. The opposite issue arises when considering for instance liquid oxygen, which exhibits a strong magnetic response, since it exists only at cryogenic temperatures.

Because the fluid cannot be magnetic itself, magnetic fluids consist mainly of a ”normal” fluid such as water or oil, which have a very weak response to magnetic fields. In order to confer significant magnetic properties to this ordinary fluid, small magnetic particles (typically around the nanometer or the micrometer scale) are dispersed in it. The properties of the magnetic fluid thus depend on both of its components, namely the **dispersed particles** [38] and the **medium fluid** [39, 40]. To properly comprehend the behavior of magnetic fluids and to differentiate their various types, it is necessary to investigate each of these characteristics.

The following sections provide an overview of magnetism, with a particular focus on the dispersed particles. In the next chapter, we will look into the interactions between these magnetic particles and the resulting self-assembly.

---

[1] Note that plastic magnets can be manufactured, but also in the solid state.

2.1 Magnets: the Fundamentals

A magnet such as those used on fridge doors both responds to an external magnetic field and produces its own magnetic field. It is characterized by its **magnetic dipole moment** $\vec{\mu}$. This vector translates the orientation and strength of the magnetic field produced by the magnet, which is described by the following equation [41] :

$$\vec{B}_\mu = \frac{\mu_0}{4\pi}\frac{3(\vec{\mu} \cdot \vec{e_r})\vec{e_r} - \vec{\mu}}{r^3}, \tag{2.1}$$

with $\vec{e_r}$ the unit vector pointing from the magnet to the considered point in space, and viewing the magnet as a point dipole [42]. In this equation, μ_0 stands for the vacuum magnetic permeability, which sets the scale for the strength of magnetic interactions in vacuum.

The magnetic dipole moment also directly influences the amplitude of the magnet's response when exposed to an external magnetic field, which can be divided in two types of motion: translation and rotation. **Translation** only occurs when the magnet is subjected to an **inhomogeneous** magnetic field, resulting in a **force** applied to the magnet. On the other hand, **rotation** is due to a **torque** that tends to align the magnetic dipole with the external field, irrespective of its homogeneity. These force and torque are expressed as follows.

$$\vec{F} = \vec{\nabla}(\vec{\mu} \cdot \vec{B}) \text{ and } \vec{\tau} = \vec{\mu} \times \vec{B} \tag{2.2}$$

That is considering one magnet. Yet, in the context of magnetic fluids, **numerous small particles** are dispersed within the fluid, meaning that each particle generates its own magnetic field and interacts with the magnetic fields of surrounding particles. This leads to the translation and/or rotation of the particles within the fluid, and quickly results in their **aggregation**, which is less than ideal for a magnetic fluid.

One solution would be to use particles so small that the thermal energy would be large enough to break the agglomerates. Another solution would be to have the ability to control whether or not the particles interact.

For example, we may want to avoid aggregation while injecting the particles into the human body but enhance interactions once they have reached the cancerous tumor. This level of control can be achieved by using non-permanent magnets. From those two different options (permanent or non-permanent magnets) result two different magnetic fluids, respectively **ferrofluids** and **superparamagnetic colloids** [38, 41].

2.2 Ferrofluids

Ferrofluids are perhaps the most widely recognized type of magnetic fluid, known for the captivating dynamic structures they exhibit when exposed to an external magnetic field. Indeed, this external stimulation often results in a global movement of the entire fluid, giving the impression that it comes to life, as it reacts and morphs in real-time to changes in the magnetic environment, forming spikes, ripples and intricate patterns. This unique behavior arises from the dispersion of small permanent magnets in the fluid, typically oil, with a size in the nanometer scale. These small magnets are referred to as *ferromagnetic* (or, in some cases, *ferrimagnetic*).

Figure 2.1: Ferrofluid under an external magnetic stimulation. Free picture from ACS [32].

2.2.1 Ferromagnetism or permanent magnets

In ferromagnetism, the magnetic dipole moment $\vec{\mu}$ is **permanent**, meaning that it exists at all time, independently of any external magnetic field. In a ferrofluid however, although each constitutive particle exhibits a magnetic dipole moment at all time, the mean magnetic moment by volume unit or **magnetization** $\vec{M}$ **remains null** while no external magnetic field is applied.

This phenomenon arises from the fact that the particles in ferrofluids are small enough to exhibit Brownian motion, driven by the fluid thermal energy. Consequently, each magnetic moment associated with the particles assumes a different orientation, resulting in the absence of overall magnetization. In contrast, upon the application of an external magnetic field, all magnetic moments align with it, leading to a net fluid magnetization. This magnetization returns to zero when the external magnetic field is turned off, and the ferrofluid reverts to its previous typical fluid behavior [33, 41, 43].

2.2.2 Stability

To clearly identify what is necessary to achieve the particles dispersion stability in ferrofluids, three energies per particle can be written as follows [41]

$$E_T = kT \tag{2.3}$$

$$E_M = \mu_0 MHV \tag{2.4}$$

$$E_G = \Delta\rho V g h. \tag{2.5}$$

E_T stands for the **thermal energy**, whith k the Boltzmann's constant and T the absolute temperature in degrees Kelvin ; E_M is the **magnetic energy**, with H the magnetic field strength (related to $\vec{B}$ as $\vec{B} = \mu_0\vec{H}$) and V the particle's volume ; E_G refers to the **gravitational energy**, with h the elevation in the gravitational field.

Looking at ratios between those three energies will provide conditions to reach overall stability, considering both the case of an in-homogeneous external magnetic field and the case where no external field is applied [41].

The first competition to consider occurs between the thermal energy and the magnetic one, when **no external magnetic field** is applied. The particles are highly concentrated within the fluid, typically with the order of 10^{23} particles per m^3 , thus collide with one another frequently. Since their magnetization is permanent, they stick together and form aggregates. In order to avoid this aggregation, the thermal energy should be able to dismantle the aggregates.

When two particles are in contact, the energy needed to separate them is the magnetic dipole-dipole contact energy

$$E_{dd} = \frac{1}{12}\mu_0 M^2 V, \tag{2.6}$$

thus the ratio to consider is the following :

$$\frac{E_T}{E_{dd}} = \frac{12kT}{\mu_0 M^2 V} \geq 1. \tag{2.7}$$

Using the following typical values, this leads to the condition of a particle diameter smaller than 7.8 nm, with $M = 4.46.10^5\,\mathrm{A.m^{-1}}$ and $T = 298\,\mathrm{K}$.

The second competition to consider is between the thermal energy and the magnetic energy due to an **in-homogeneous external magnetic field**. When subjected to such a field gradient, particles move from the lower-intensity regions of the field to the higher-intensity region. To avoid this settling, E_T has to be larger than E_M, since the thermal gradient motion counteracts this effect. This translates as

$$\frac{E_T}{E_M} = \frac{kT}{\mu_0 MHV} \geq 1, \tag{2.8}$$

and implies, when considering typical values, that a sphere shaped particle should have a diameter smaller than 8.1 nm to ensure stability against a magnetic field gradient.

The last competition is between **gravitational and thermal energy** and is similar to the previous one, since gravity induces a field gradient that tends to attract particles downward, while thermal agitation tends to keep the particles dispersed. However, it will not give any new condition for stability, since the gravitational energy in this context is smaller than the magnetic energy. Indeed,

$$\frac{E_G}{E_M} = 0.047 \tag{2.9}$$

for a 5 cm high container and for $\Delta\rho = 4300\,\mathrm{kg.m}^3$.

To those three conditions, all leading to a maximal size for the ferrofluid particles around 10 nm, we must add a reasoning about the **van der Waals interactions**. Indeed, these interactions occur between neutral particles and are independent of their magnetic properties, since they come from electric dipole-dipole interactions, and lead to an attractive force in the case of ferrofluid particles [37, 41, 44].

To counteract this attraction between particles, it is necessary to introduce a repulsion. This is achieved by coating the particles with chemical groups that will charge in the liquid [34, 38, 44, 45]. Since the liquid is polar and includes mobile ions, two layers of opposite charge are formed at the particles surface, as those ions are attracted to the charged chemical groups, as pictured in Fig. 2.2. This **Electric Double Layer**, or EDL, shields the particles against the van der Waals attractive force, as stated by the DLVO theory [46], named after two scientific duos that independently developed it : Derjaguin with Landau and Verway with Overbeek. In this theory, each interaction is considered independent, and the total interaction potential is thus expressed as the sum of the individual potentials [44, 46].

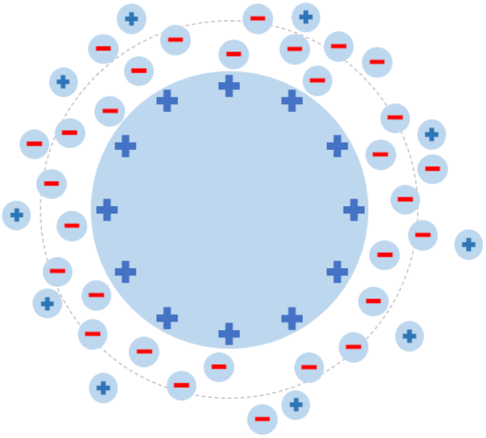

Figure 2.2: Representation of the Electric Double Layer around a particle coated with charged chemical groups.

To the van der Waals and the EDL interactions must be added a third interaction, known as the **Born repulsion**, which translates the impossibility for the particles to interpenetrate. Those 3 interactions, as well as the resulting total interaction potential, are depicted in Fig. 2.3. Instead of using the chemical groups mentioned above, the particles can be coated with polymers to prevent direct surface contact, harnessing the steric interactions to reduce the van der Waals attraction [34, 38]. The steric interactions are not taken into account in the DLVO theory.

2.3 Superparamagnetic Colloids

A less known type of magnetic fluid is magnetic colloids. Although less impressive than ferrofluids, since they do not deform as much under an external magnetic field, their unique properties make them particularly interesting in a large scope of application, ranging from water depollution to in situ drug delivery [33, 47].

Magnetic colloids are similar to ferrofluids in a lot of ways, starting with the fact that they are made of solid particles dispersed in a fluid. However, the colloidal particles are larger, typically around the

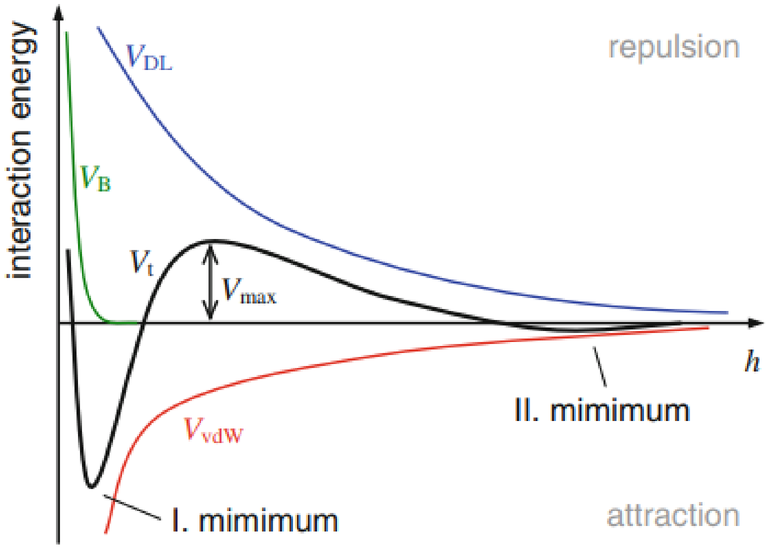

Figure 2.3: In this diagram from [44], the three interaction potentials considered in the DLVO theory are represented. In red, the van der Waals interaction potential, in blue, the potential due to the Electric Double Layer, and in green the Born repulsion. Those three potential are added to one another in the DLVO theory, leading to the global potential in black.

micrometer scale, and the most used dispersion medium is water. Moreover, in this context, the colloids are not permanent magnets, as it is the case for the dispersed particles in ferrofluids, but **non-permanent magnets**, which allows the user to avoid magnetic interactions when needed.

2.3.1 Paramagnetism or non-permanent magnets

Non-permanent magnets are very similar to the more commonly known permanent magnets, with the key distinction that their magnetic dipole moment only appears **when exposed to an external magnetic field**.

Consequently, if no external field is applied, these materials exhibit no magnetic properties. Such materials are classified as either *paramagnetic* or *diamagnetic*, with the primary difference that in paramagnetism, $\vec{\mu}$ aligns exactly with the external field, while in diamagnetism, $\vec{\mu}$ is anti-parallel to the external field.

Using para- or dia- magnetic particles in magnetic fluids then proves to be a viable option. However, paramagnetic particles are preferred due the weak magnetization associated with diamagnetic materials, resulting in weak particles interactions. Indeed, magnetization is proportional to $\vec{B}_{ext}$, the applied magnetic field, and to χ_m, the material magnetic susceptibility [41] :

$$\vec{M} = \chi_m \frac{\vec{B}}{\mu_0}. \tag{2.10}$$

The magnetic susceptibility is a non-dimensional number, positive for paramagnetic materials and negative for diamagnetic ones. Its amplitude is much larger in the paramagnetic case (ranging from 10^{-4} to 10^{-2}) compared to the diamagnetic case (with an order of magnitude of 10^{-5}).

Given the definition of magnetization, the previous equation can be re-written as following, which highlights that the smaller the magnetic susceptibility, the weaker the magnetic dipole moment, thus the weaker the magnetic interactions :

$$\vec{\mu} = \chi_m V \frac{\vec{B}}{\mu_0}. \tag{2.11}$$

Even though χ_m is larger in the paramagnetic case compared to the diamagnetic case, it is even larger in the ferromagnetic case, since it is typically above 10^4. However, as a reminder, the magnetic dipole is permanent in ferromagnetic materials, while it only exists in para- or diamagnetic materials when an magnetic field is applied. When exposed to high temperature, the magnetic susceptibility decreases due to thermal agitation, and when a critical temperature called *Curie temperature* is reached, ferromagnetic materials become paramagnetic [33, 41].

2.3.2 Superparamagnetism or the magnetic boost

In order to enhance the magnetic susceptibility of the colloids and ensure the absence of remanent magnetization even in small domains within the fluid, a combination of **ferromagnetism** and **diamagnetism** is employed [27]. This gives rise to a new type of magnetism known as *superparamagnetism*.

Superparamagnetism relies on nanometric ferromagnetic particles embedded within a diamagnetic shell to form a single colloid, as shown in Fig. 2.4. While each inclusion has a permanent magnetic dipole, thermal agitation prevents overall magnetization without an external magnetic field. This is similar to paramagnetism, but with a higher magnetic susceptibility (ranging from 10^{-2} to 1), making superparamagnetic colloids more responsive to magnetic fields. The use of ferromagnetic inclusions also induces a quasi-null magnetization remanence [27].

2.3.3 Stability

Looking at the energy ratios presented in section 2.2.2, notable differences quickly emerge.

Firstly, the competition between thermal energy and magnetic energy in the **absence of an external field** is not relevant as the particles exhibit no magnetic dipole moment in this context.

Secondly, considering the effect of a **magnetic field gradient**, it becomes evident that superparamagnetic colloids are too large to avoid settling between low-intensity and high-intensity field regions. Surprisingly, this property can be advantageous, as it enables the user to collect the particles, leaving the medium fluid pure and intact. This migration of magnetic particles is termed *magnetophoresis* [48, 49]. This separation is not achievable in the case of ferrofluids, much like separating salted water into salt and water is impossible without damaging one or another.

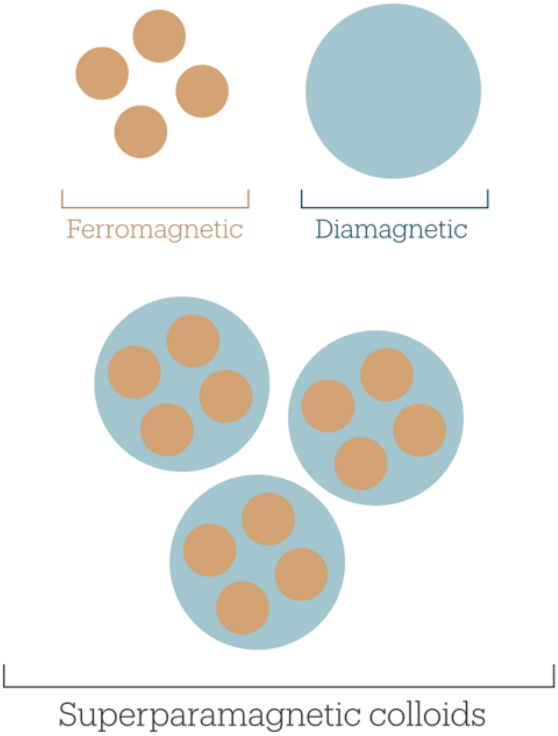

Figure 2.4: Schematic representation of superparamagnetic colloids. Each colloid consists of ferromagnetic particles (shown in orange) embedded within a diamagnetic core (shown in blue).

Lastly, the interplay between **thermal and gravitational energy** significantly influences the suspension stability regarding the sedimentation, in contrast to ferrofluids. This competition translates as follows

$$\frac{E_T}{E_G} = \frac{kT}{\Delta\rho V g h}, \tag{2.12}$$

with $\Delta\rho$ close to ρ_{eau}, thus smaller than the ferrofluid case. The larger h is, the smaller the critical diameter to sustain stability against sedimentation.

With otherwise keeping the same values as in section 2.2.2, this leads to a diameter with a magnitude of order around $10^{-7}\,\mathrm{m}$, still smaller than the size of superparamagnetic colloids.

To better look into this issue, we will consider the **Péclet Number**,

$$Pe = \frac{\tau_B}{\tau_S}, \tag{2.13}$$

which compare τ_B, the Brownian characteristic time for a particle to diffuse on a distance equivalent to its radius, and τ_S, the characteristic time for a particle to settle on the same distance [45, 50]. This comes back to comparing the thermal and gravitational effects. If R stands for the particle radius and D the diffusion coefficient, τ_B can be written as

$$\tau_B = \frac{R^2}{D}. \tag{2.14}$$

If v_s stands for the particles characteristic sedimentation speed, τ_S can be written as :

$$\tau_S = \frac{R}{v_S}. \tag{2.15}$$

This leads to this expression for the Péclet number :

$$Pe = \frac{Rv_S}{D}. \tag{2.16}$$

The **sedimentation speed** of one particle can be determined by equalizing the Stoke force F_S applying on this particle and its weight, with the Buyoncy deducted. If F_S is expressed as $F_S = 6\pi\eta R v_S$, with η the fluid viscosity and $\Delta\rho$ the difference between the solid and the fluid density, then the sedimentation speed is

$$v_S = \frac{2R^2\Delta\rho g}{9\eta}. \tag{2.17}$$

D, the diffusion coefficient, is expressed thanks to the Stokes-Einstein relation as

$$D = \frac{k_B T}{6\pi\eta R}. \tag{2.18}$$

Using those expressions for v_S and D gives this expression for the Péclet number [50] :

$$Pe = \frac{4R^4\pi\Delta\rho g}{3k_B T}. \tag{2.19}$$

The transition between a system dominated by the thermal agitation and a system driven by the sedimentation occurs theoretically at $Pe = 1$, but it is commonly considered that the brownian motion is significant when the Péclet number becomes smaller than 10. If we consider $\Delta\rho$ to be around 10^3, which is consistent with common superparamagnetic colloids and water density, we find a radius smaller than $1\,\mu$m for the colloidal particles. This indicates that **micrometric particles** suspended in a fluid would be relatively **stable** against settling.

As for ferrofluids, superparamagnetic particles are attracted to each other because of the van der Waals interactions. To prevent this aggregation, unrelated to any magnetic interactions, the particles are coated with chemical groups that will charge in the liquid, inducing an Electric Double Layer (EDL) that will shield the particles against the van der Waals attractive force [45]. This is similar to what was already described in section 2.2.2 for ferrofluids.

2.4 Overview

In summary, there are three main differences between ferrofluids and superparamagnetic colloids.

The primary and most significant difference is the composition of the particles. Ferrofluids are made with **permanent magnets**, or *ferromagnetic* particles, whereas magnetic colloids use **non-permanent**

magnets, or *superparamagnetic* particles. However, both rely on thermal agitation, which allows ferrofluids to exhibit no magnetization when no magnetic field is applied, and enables magnetic colloids to display no magnetic dipole at the colloidal scale in the same context.

The second difference lies in the size of the particles. Ferrofluid particles are **smaller** (typically around 10^{-9} in size) than magnetic colloids (typically around 10^{-6} in size), leading to distinct behaviours. In both cases, there is no aggregation when no magnetic field is applied. This is due to the ferrofluid particles having sufficient thermal energy to prevent magnetic aggregation, thanks to their size, and superparamagnetic colloids showing no magnetic dipole in the absence of an external magnetic field. When a magnetic field is applied, particle dispersion remains **homogeneous** in ferrofluids, while either **magnetophoresis** or **aggregation** is observed in magnetic colloids, depending on the field homogeneity. Regarding particle settling, it **does not** occurs in ferrofluids. Theoretically, it should not occur either in the case of superparamagnetic colloids, but sedimentation is **still observed** after a long time (several hours).

Finally, beyond distinctions related to the particles themselves, we must also consider the fluid medium. Indeed, **oils** are predominantly used in the case of ferrofluids, while **water** is preferred for magnetic colloids.

All these features contribute to distinct behaviors under the influence of an external magnetic field, both at the microscopic and macroscopic level, depending on the magnetic field characteristics. In this work, we focus on microscopic and macroscopic effects on superparamagnetic colloids through the application of a time-varying magnetic field.

3

Magnetic colloids in a Plane

Dancing particles and their dynamic Structures

As outlined in the preceding chapter, magnets in general are of considerable interest to scientists because of their ability to be externally controlled. In the specific domain of superparamagnetic colloids, managing the movements of the dispersed particles without inducing fluid body motion enables diverse applications, including water depollution [51, 52], fluid mixing [53–55], and drug targeting [56–59]. This control over particle motion is achieved thanks to specific magnetic fields [24, 60]. Each type of external magnetic field (homogeneous/inhomogeneous, constant/time-varying) leads to distinct interactions among the dispersed particles, yielding varied dynamics and assemblies [27, 61]. Our investigations primarily focus on homogeneous magnetic fields, whether constant or time-varying. In this chapter, we look further into the interactions between the dispersed particles and their microscopic consequences.

3.1 Particles interactions

When suspended in a fluid alongside numerous other particles and exposed to an external magnetic field $\vec{B}_{ext}$, superparamagnetic colloids interact with both this external field and the magnetic field produced by all of the surrounding particles. The magnetic field generated by one particle is equivalent to that of a point dipole with the same magnetic moment located at the sphere's center, and can therefore be expressed as in Eq. (2.1) [42, 48]. Note that since the particles are suspended in a medium, the term μ_0 in this expression must be replaced by the medium's magnetic permeability. However, in the case of superparamagnetic colloids, the medium is aqueous, and its magnetic permeability approximates μ_0. Consequently, a single colloid i experiences a total magnetic field $\vec{B}_{tot}$, resulting from the superposition of $\vec{B}_{ext}$ and $\vec{B}_j$, the magnetic field produced by the other particles j in the suspension. This total magnetic field is expressed as follows :

$$\vec{B}_{tot} = \vec{B}_{ext} + \sum_{j \neq i} \vec{B}_j. \tag{3.1}$$

From this surrounding magnetic field arise both a force and a torque, whose expressions were provided in Eq. (2.2). When $\vec{B}_{ext}$ is homogeneous, as will invariably be the case in our experiments, particles rotate to align with it, but do not experience any force, whereas $\vec{B}_j$ is invariably inhomogeneous, inducing a force on the particle i. The force exerted on the particle can also be expressed as $\vec{F} = -\vec{\nabla} U$, where U plays the role of the interaction potential between $\vec{\mu}$ and $\vec{B}_{tot}$:

$$U = -\vec{\mu} \cdot \vec{B}_{tot}. \tag{3.2}$$

Given this equation and the expression of $\vec{B}$ provided in Eq. (2.1), we can derive $U_{1,2}$, the interaction potential energy between two particles, with their respective magnetic moment $\vec{\mu_1}$, $\vec{\mu_2}$, and $\vec{r}$, the unit vector connecting their center :

$$U_{1,2} = \frac{\mu_0}{4\pi} \frac{-3(\vec{\mu}_1 \cdot \vec{r})(\vec{\mu}_2 \cdot \vec{r}) + \vec{\mu}_1 \cdot \vec{\mu}_2}{r^3}. \tag{3.3}$$

Substituting each magnetic moment $\vec{\mu}$ with its expression from Eq. (2.11), and considering spheres with identical radii R, the foregoing equation is rendered as :

$$U(r, \theta) = 4\pi R^6 \chi_m^2 B^2 \frac{1}{9\mu_0} \frac{(-3\cos^2\theta + 1)}{r^3}. \tag{3.4}$$

In this expression, the angle θ is measured between $\vec{B}$ and $\vec{r}$. The two magnetic moment $\vec{\mu}_1$ and $\vec{\mu}_2$ are aligned with the field, thus pointing in the same direction $\vec{e}_z$.

Since $U \sim 1 - 3\cos^2\theta$, two primary scenarios arise, depending on the values of θ. These two scenarios correspond to an **attractive** ($U < 0$) or a **repulsive** ($U > 0$) interaction between the two particles. The transition from one case to the other occurs when $U = 0$, manifesting as the *magic angle* $\theta_M = 54,7°$. These scenarios are depicted in Fig. 3.1. When the two particles are **aligned** with one another, θ is equal to 0°, meaning that U is negative and minimal, which leads to the **attraction** of the particles. Conversely, when the particles are side to side, which corresponds to $\theta = 90°$, U is positive and maximal, yielding the **repulsion** of the particles. This phenomenon gives rise to the formation of *chains* aligned with the applied magnetic field. The aggregation into chains has been both theoretically and experimentally demonstrated in several studies [27], and has been proven to be reversible, with chains disassembling once the external magnetic field is removed.

Having established **the fundamental interactions between the particles**, we now turn our attention to the behavior of the system under a **constant** and a **time-varying** magnetic field.

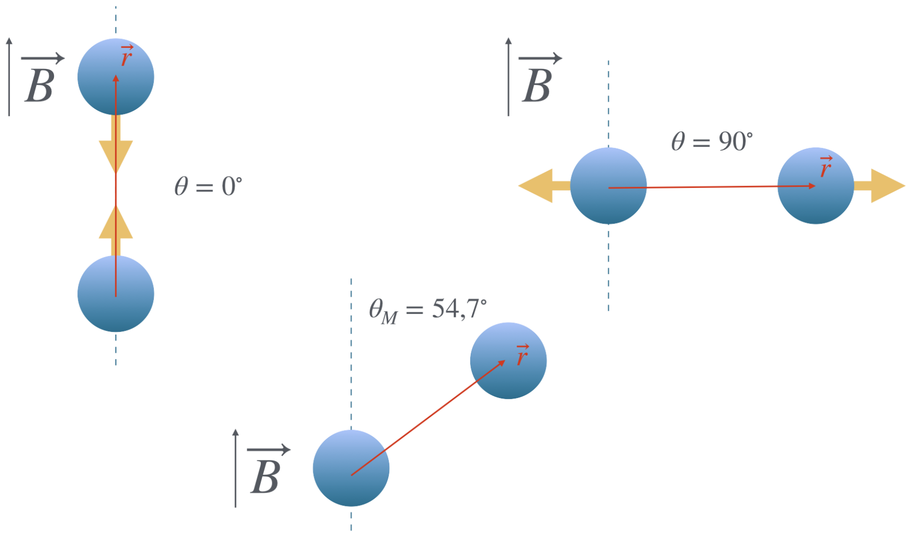

Figure 3.1: Diagram illustrating the dipolar interaction between two particles subjected to an external magnetic field $\vec{B}$. Each particle's magnetic moment is aligned with $\vec{B}$. The orange arrows denote the dipolar force experienced by each particle, while the red vector represent $\vec{r}$, the unit vector connecting the particles. The angle θ between $\vec{B}$ and $\vec{r}$ is specified for each scenario. When $\theta = 0°$, the two particles are attracted to each other. Conversely, when $\theta = 90°$, the two particles repel each other. The case where no force is experienced by the particles correspond to the magic angle, $\theta_M = 54,7°$.

3.2 Constant magnetic field

Considering the interaction potential in Eq. (3.4) in the context of an homogeneous external magnetic field constant over time, we can understand that the dispersed particles will assemble into chains oriented along $\vec{B}_{ext}$. The pair interaction potential driving this aggregation is spatially anisotropic, and results in a magnetic force exerted on the i^{th} particle by the j^{th}. Since $\vec{F} = -\vec{\nabla} U$ and given Eq. (3.2), this force can be expressed as follows, taking into account Eq. (2.1) :

$$\vec{F}_{ij} = -\vec{\nabla}(-\vec{\mu}_i \cdot \vec{B}_{\mu_j}). \tag{3.5}$$

This results in the following radial and tangential components :

$$F_{ij,\vec{e}_r} = \frac{3\mu_0\mu_1\mu_2}{4\pi r^4}(1 - 3\cos^2\theta), \tag{3.6}$$

$$F_{ij,\vec{e}_\theta} = -\frac{3\mu_0\mu_1\mu_2}{4\pi r^4}\sin 2\theta. \tag{3.7}$$

Which translates as, when considering Eq. (2.11) with spherical particles of the same radius R :

$$F_{ij,\vec{e}_r} = \frac{4\pi R^6\chi_m^2 B_{ext}^2}{3\mu_0 r^4}(1 - 3\cos^2\theta), \tag{3.8}$$

$$F_{ij,\vec{e}_\theta} = -\frac{4\pi R^6\chi_m^2 B_{ext}^2}{3\mu_0 r^4}\sin 2\theta. \tag{3.9}$$

The magnetic force described above drives the particles from a **dispersed configuration** to a **head-to-tail alignment**. The growth of these chains can be effectively described by the Smoluchowski equations, which predict that the mean size of the chains $\langle s \rangle$ follows a power law $\langle s \rangle \propto t^z$ after an initial short-time transient period where the growth is practically null [40, 62, 63]. In long-term experiments, the length of the chain eventually reaches a saturation value, depending mainly on the strength of the magnetic field, as illustrated in Fig. 3.2. The viscosity of the medium fluid also plays a role by influencing the characteristic time of the agglomeration process, although it does not significantly alter the underlying physical mechanisms [40]. Additionally, a coupling between the aggregation and the subsequent sedimentation has been observed [64], and is detailed in Section 4.4.

Below a critical value of the magnetic field, the saturation length of the chains is due to the system reaching a thermodynamic equilibrium and has been predicted by Andreu *et al.* through both numerical simulations and thermodynamic analysis [65].

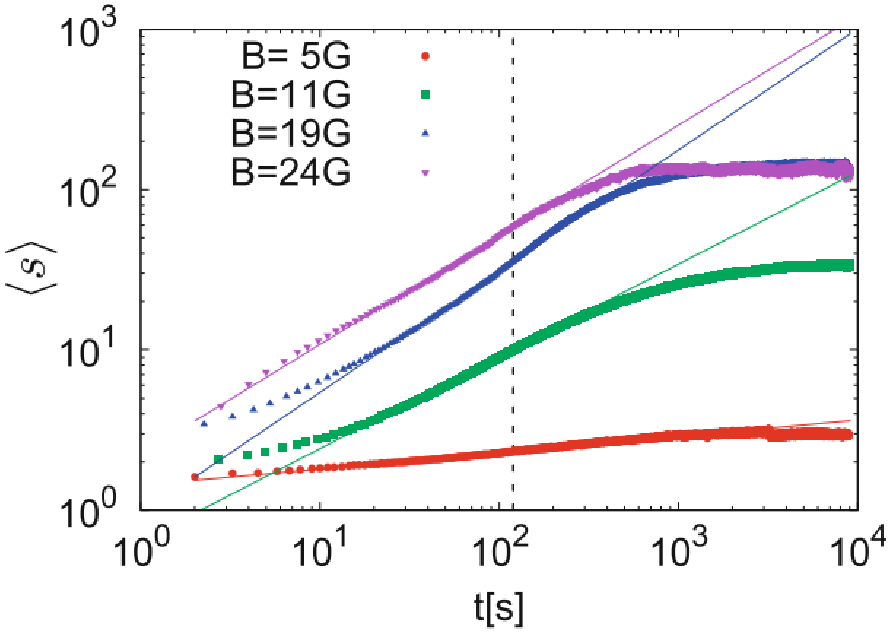

Figure 3.2: Log-log plot from Darras et al. [63] showing the evolution of $\langle s \rangle$ over time for different magnetic field intensities. Initially, growth is negligible, followed by a power-law growth period fitted by the solid lines with exponents 0.1, 0.57, 0.75, and 0.68. Beyond the dashed line, the mean length reaches a saturation value dependent on the magnetic field amplitude. Error bars indicate the size of the data points.

This equilibrium emerges from the interplay between the magnetic energy of the particles and the entropy of mixing. As indicated in Eq. (3.4), the particles magnetic energy is minimized when they are all aggregated. The entropy of mixing, on the other hand, is maximized for a mixture of different chains. In a three-dimensional system, the competition leading to the thermodynamic equilibrium results in the following expression, assuming that the particles solely aggregate into linear chains and not into other stable structures such as rings or ribbons [27, 63, 65] :

$$\langle s \rangle = \sqrt{\phi_0 \exp(\Gamma - 1)}. \tag{3.10}$$

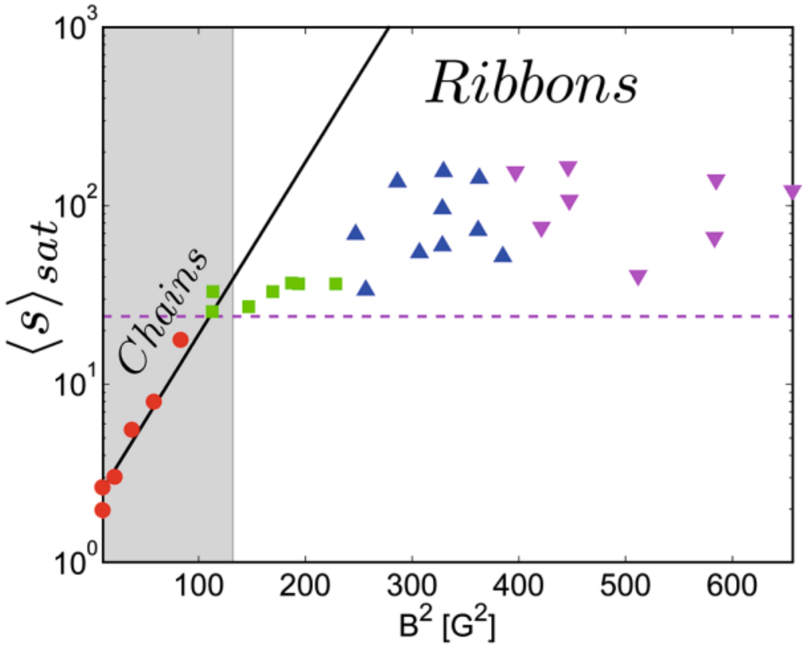

Figure 3.3: Plot from Darras et al. [63] showing mean chain length at saturation for various magnetic field amplitudes, with each color representing a different amplitude range. For each amplitude range, typical behaviors are depicted in Fig. 3.2 using the same color scheme. The solid black line fits data within the grey area to the model in Eq. (3.10). In this range, the mean saturation length aligns with the model. For stronger magnetic fields in the white area, experimental results show shorter aggregates than predicted, suggesting the need to consider chain aggregation into ribbons.

In the previous equation, ϕ_0 is the total particles volume fraction and Γ is a dimensionless parameter translating the competition between the magnetic and the thermal energy such as

$$\Gamma = -\frac{U_{min}}{k_B T} = \frac{\chi^2 \pi R^3 B_{ext}^2}{9 \mu_0 k_B T}. \tag{3.11}$$

U_{min} refers to the minimal magnetic interaction potential of a pair of colloidal particles, which is achieved when the particles are aligned head-to-tail in the direction of the external magnetic field. In this situation, $r = 2R$ and $\theta = 0$ in Eq. (3.4).

However, when investigating experimentally the saturation length of the chains with long-time experiments, a discrepancy with the theoretical expectations from Eq. (3.10) appears above a critical value of the external magnetic field, as illustrated in Fig. 3.3 with experimental results obtained by Darras *et al.* [63]. In their work, Darras *et al.* state that the fact that the saturation length is lower than expected past a critical B_{ext} is due to the formation of **ribbons**, which they observed experimentally. In this case, they found that two chains of 15 particles aggregated side by side are more stable than a single chain of 30 particles by estimating the energy barrier for lateral aggregation. The width of these ribons was observed to go up to 3 particles diameter.

To summarize, when exposed to a magnetic field, the superparamagnetic colloidal particles first **do not aggregate**, for a short transient time. After this short time, the particles start to aggregate, either into **chains** or into **ribbons**, depending on the **intensity** of the external magnetic field. Below a critical value, chains are observed, with a larger saturation length when $\vec{B}_{ext}$ is stronger. Above this critical magnetic field intensity, ribbons are rather observed, with a more or less constant saturation length.

3.3 Rotating magnetic field

The preceding reasoning describes the aggregation kinetics of colloidal particles into chains when exposed to a static magnetic field. However, keeping in mind the goal of controlling externally the particles, it appears that using a **time-varying magnetic field** is interesting, since it offers more complex interactions and a wider range of dynamics.

While a magnetic field may vary with time in a lot of different ways, one of the simpliest is the rotating magnetic field. This is by the way precisely the type of time-varying magnetic field that will be explored in this work.

A rotating magnetic field is defined by two sinusoidal waves separated by a phase of $\pi/2$:

$$\vec{B}_{ext} = B_0 \begin{pmatrix} \cos(\omega t)\, \vec{e}_x \\ \sin(\omega t)\, \vec{e}_y \end{pmatrix}, \tag{3.12}$$

with B_0 the external magnetic field intensity and ω the magnetic field angular velocity.

3.3.1 Rotating Chains

If we consider a referential system rotating at constant speed with the external magnetic field, the situation appears to be similar to the one described before, with the formation of chains in the same direction as the external field, due to magnetic interactions. However, an additional interaction must be taken into account, due to the viscosity of the surrounding medium and the fact that the chains are moving in the fluid [26, 66–69]. As a reminder, the most used medium liquid in the context of superparamagnetic colloids is water.

In the case of a static field, the chains aggregation dynamics are driven by the magnetic force experienced by a particle due to all of the other surrounding particles. The particles also experience a magnetic torque, that make them rotate to align with the external magnetic field. In the case of a rotating field, the situation is different. Indeed, the chain as a whole is first orientated as the field, but since the field is rotating, its orientation varies with time. The characteristic time for the chains to realign with the external magnetic field is non zero, inducing a phase lag angle θ_0 between the chain and the field. This phase lag induces a magnetic torque on the individual particles, leading them to rotate, and resulting in the rotation of the chain itself in a process that will be further explained in the following section. The rotation of the chain in the medium fluid is impeded by the viscous drag due to its viscosity, which further increases the phase lag angle θ_0.

The dynamics of the rotating chains are thus led by the competition between the magnetic and the viscous torques.

Considering a straight chains made of several particles and making an angle θ_0 with the external magnetic field, we can expect from Eq. (3.8) and Eq. (3.9) that each particle experiences a dipole-dipole force due to its neighbours. However, as expressed in these equations, this dipole-dipole force scales as r^{-4}, meaning that only the closest neighbours will have an influence. Therefore, all particles situated in the core of the chain and not at its extremities experience an approximately null net force, as the influence of one neighbour is balanced by the other-side neighbour. Thus, the only particles to experience a significant aligning force with the magnetic field are those at the chain extremities. This implies that the first particles to move in order to align with the magnetic field are the extreme ones, leading to the rotation of the chain and inducing a characteristic S-shaped deformation in the direction of rotation.

If the phase lag angle θ_0 between the chain and the external magnetic field remains smaller than the magic angle θ_M, the chain continues to rotate and align with the field. However, if θ_0 becomes larger than θ_M due to viscous drag, the dipole-dipole force transitions from attractive to repulsive, leading to the break-up of the chain. Given the S-shape of the chain, this break-up is expected to occur at its center, where the phase lag is the largest. This phenomenon has been observed both numerically and experimentally, confirming the theoretical predictions [26, 67–71].

3.3.2 Chains break-up frequency

In order to further look into this interplay between the magnetic effects and the viscous drag, it is decisive to formally define the **magnetic torque**, **translational friction torque**, and **rotational friction torque**. Various approaches have been explored in the literature to accomplish this task. Notably, Vazquez-Quesada *et al.* [26] have introduced in their work a multi-order drag approach, which they compare to existing theoretical frameworks and empirical findings.

First, to express the **magnetic torque**, we approximate the chain as being straight. Additionally, since the rotation of the chain is driven by the motion of the external particles, we consider that all the magnetic torque is exerted by those particles, and that the subsequent internal particles motion is due to the magnetic attraction force between them. Then, the magnetic torque can be computed as

$$\vec{\tau}_B = L\,\vec{e}_c \times \vec{F}_N, \tag{3.13}$$

with L the chain length, $\vec{e}_c$ the constant unit vector oriented in the chain direction (which corresponds to $\vec{e}_r$ in Eq. (3.6)) and $\vec{F}_N$ the magnetic force exerted on the external particle (which corresponds to $\vec{F}_{ij}$ in Eq. (3.5), the external particle being the i^{th} particle and its first neighbour the j^{th} particle). Considering that the external magnetic field rotates at an angular velocity ω with an initial phase of rotation Φ, whereas the chain rotates at an angular velocity ω' with an initial phase of rotation Φ', and assuming all particles within the chain possess the same magnetic moment μ_p, the magnetic torque can be expressed as follows :

$$\tau_B = L\frac{3\mu_0\mu_p^2}{4\pi r^4}\sin(2(\omega-\omega')t + 2(\Phi-\Phi')). \tag{3.14}$$

Moving on to the **viscosity torque** acting on the chain, it is essential to account for two distinct types of friction. The first arises from the movement of the chain within a viscous fluid, while the second originates from the rotational motion of the particles in the fluid. It's worth noting that this friction torque can also be described using the shish-kebab model [72] for long chains, with an adapted version for short chains. In our case, following the work of Vazquez-Quesada *et al.* [26], the friction experienced by a particle i due to the chain movement is expressed thanks to the Stoke's Law, as we are in the context of a low Reynolds number :

$$\vec{F}_\nu = -6\pi\eta R\,(\vec{\omega}' \times \vec{r}_i). \tag{3.15}$$

This formulation yields the translational friction torque as:

$$\vec{\tau}_{\nu,T} = -6\pi\eta R \sum_i \vec{r_i} \times (\vec{\omega}' \times \vec{r_i}), \tag{3.16}$$

On the other hand, the rotational friction torque on a single particle is expressed as

$$\vec{\tau}_{\nu,R} = -8\pi\eta R^3 \vec{\omega}'. \tag{3.17}$$

The addition of those two components gives as a result the total viscous friction torque on a chain of N particles, with the origin of coordinates located in the middle of the chain, meaning that $\vec{r_i}$ and $\vec{\omega}'$ are normal :

$$\begin{aligned} \vec{\tau}_{\nu} &= -6\pi\eta R \sum_i \vec{r_i} \times (\vec{\omega}' \times \vec{r_i}) - N\, 8\pi\eta R^3 \vec{\omega}' \\ &= -2\pi\eta R \vec{\omega}' \left(3 \sum_i r_i^2 + 4NR^2 \right). \end{aligned} \tag{3.18}$$

Now that the the magnetic and the viscous friction torques have been calculated, we are able to describe the evolution of the rotation dynamics with the following expression, introducing I, the moment of inertia of the chain :

$$I \frac{d\vec{\omega}'}{dt} = \vec{\tau}_B + \vec{\tau}_{\nu}. \tag{3.19}$$

When using Eq. (3.13), Eq. (3.14) and Eq. (3.18), this expression results in

$$\begin{aligned} I \frac{d\omega'}{dt} =& L \frac{3\mu_0 \mu_p^2}{4\pi r^4} \sin(2(\omega - \omega')t + 2(\Phi - \Phi')) \\ &- 2\pi\eta R \omega' \left(3 \sum_i r_i^2 + 4NR^2 \right). \end{aligned} \tag{3.20}$$

Given that the origin of coordinates is located at the chain center, and that the chain is made of N particles, we can deduce that $\sum_i r_i^2 = \frac{1}{2}\frac{N(N^2-1)}{6}r^2$. We can also express the chain length (center-to-center distance between the two external beads) as $L = (N-1)r$.

In order to find the **critical frequency** above which the chain will break-up, we consider the situation where the chain is able to follow exactly the external magnetic field at a constant angular velocity, meaning that a stationary state is established and that the chain will not break up. This corresponds to the case where $\omega - \omega' = 0$ and $\frac{d\omega'}{dt} = 0$, leading to an equilibrium phase $\theta_0 = \Phi - \Phi'$ such as

$$\sin(2\theta_0) = 2\pi\eta R\omega \frac{4\pi r^3}{3\mu_0\mu_p^2}\frac{N}{(N-1)}\left(\frac{1}{4}(N^2-1)r^2 + 4R^2\right). \tag{3.21}$$

The situation where the magnetic torque τ_B expressed in Eq. (3.14) is maximum corresponds to $\theta_0 = \pi/4$. As long as **the maximum** τ_B is **larger** than the **total viscous torque** τ_ν, the magnetic effects will be able to **balance** the viscous friction, and **the chain will be able to follow** steadily the external rotating field.

This condition resumes to $\theta_0 \leq \pi/4$ since if at the start $\theta_0 < \pi/4$, the viscous friction will delay the chain rotation until reaching the value where magnetic and viscous torque balance each other. However, this value will never be reached if $\theta_0 > \pi/4$, and the solution of Eq. (3.21) obtained under the steady assumption will be unstable, leading to an increasing delay of the chain compared to the external magnetic field. Once the delay will reach the value of θ_M exposed in section 3.1, the magnetic interactions will become repulsive instead of attractive, and the chain will rupture.

We can thus find the intended critical frequency at which the chain destabilizes and breaks by replacing θ_0 by its critical value, $\frac{\pi}{4}$:

$$\omega_c = \frac{1}{2\pi\eta R}\frac{3\mu_0\mu_p^2}{4\pi r^3}\frac{(N-1)}{N}\left(\frac{1}{4}(N^2-1)r^2 + 4R^2\right)^{-1}. \tag{3.22}$$

If we consider that the particles are touching each other in the chain, then $r = 2R$, r being the center-to-center distance between two adjacent particles and R the particles radius. This gives this expression for the critical break-up frequency :

$$\boxed{\omega_c = \frac{3\mu_0\mu^2}{64\pi^2R^6\eta}\frac{(N-1)}{N(N^2+3)}.} \tag{3.23}$$

Similar approaches have been conducted by Gao *et al.* [68] and Franke *et al.* [53], with slight differences in the definition of the magnetic and viscous friction torques. Both of the resulting critical break-up frequencies are quite close to the one presented above, since they all predict the decreasing of ω_c for an increasing chain length. However, all three of them also quantitatively overestimate the critical frequency compared to numerical simulations, especially for short chains, even if it seems less clear when comparing to experimental results.

To resolve this overestimation, Vazquez-Quesada *et al.* have added to the friction torque the **lubrication interaction** between two close particles. This interaction comes from the presence of a thin fluid film between the surface of two close solids, as it is the case in a chain superparamagnetic colloids. For very close particles, this interaction can be larger than the Stoke's drag, which indicates that its influence can be decisive. As it is the case for the magnetic forces on the internal particles, the net lubrication force will be null, since the influence of the two neighbours of such an internal particle will balance each other. Then, the effect of lubrication will only be relevant for the extreme particles. Furthermore, only the tangential lubrication will be considered, since we assume that the distance between the particles does not change significantly over time (before the breakup), meaning that normal lubrication is not important. On the opposite, the tangential velocity of the particles increases the further the particle is from the center, meaning that tangential lubrication will be significant [26]. Since the addition of the lubrication does not change the qualitative description of ω_c in regards to the chain length, we will not discuss it further in this work.

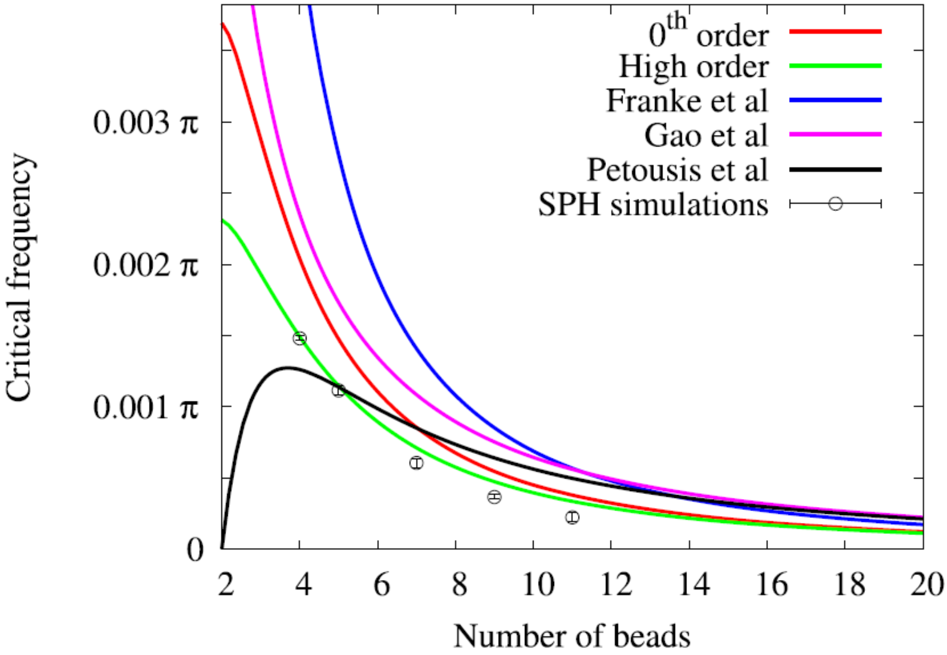

Figure 3.4: Figure from Vazquez-Quesada *et al.* [26], comparing 5 distinct models for the chain critical break-up frequency (solid curves) to simulation results (circles with errorbars). In red, the model detailed in this section, which leads to the critical frequency in Eq. (3.23). In green, the same model with the lubrication friction added. In blue, pink and black, 3 other models developed respectively by Franke *et al.* [53], Gao *et al.* [68] and Petousis *et al.* [66], with other approaches to the expression of magnetic and viscous torques.

All of the previously discussed approaches are illustrated in Fig. 3.4, which highlights the decrease in the critical breakup frequency as chain length increases. This also implies that **as the external magnetic field rotates faster, the chains in the suspension become shorter**.

3.3.3 Rotating disk-like clusters

As discussed in the previous section, the angular velocity of the magnetic field is the critical parameter governing the length of the chains. However, when this angular velocity surpasses the translation speed of the particles, the interaction potential becomes **isotropic**, leading to significantly different assembly dynamics and resulting structures. Indeed, in this conditions, the potential expressed in Eq. (3.4) can be averaged over one period or rotation, considering that the magnetic dipoles are rotating at the same speed as the field with a constant phase lag angle θ_0 [73, 74]. This leads to the following expression, with the crucial assumption that the translational motion of the particles over one rotational period of the field is negligible :

$$U_{iso} = -\frac{\mu^2}{2r^3}. \tag{3.24}$$

Given the fact that this potential is **attractive**, the particles are no longer assembling into chains directed in the same direction as the magnetic field, as it was the case for smaller rotation speeds, but rather clustering into **disk-like structures**. Such structures are indeed observed both experimentally [70, 75] and numerically [73, 74]. These nondirectional interactions are frequently likened to intermolecular forces. Consequently, cluster assemblies exhibit configurations and dynamics reminiscent of those observed in molecular systems, and can be used as experimental thermodynamic models for molecular phase transitions [24].

As it is the case for smaller rotational frequencies, the magnetic interactions lead the movements of the colloidal particles, and since the particles are moving in a viscous fluid, they also experience hydrodynamic effects. The aggregation dynamics are thus driven by the competition between the **magnetic interactions** and the **hydrodynamic interactions**. The magnetic interaction potential in this case has already been described in the preceding paragraph (see Eq. (3.24)), and leads the particles to move and gather into isotropic clusters. Please note that those clusters also rotates, with varying rotational speeds.

This constitutes a main difference compared to the chain aggregation case. Indeed, not only the magnetic interactions, which lead the particles and clusters motion, but also the consequent hydrodynamic interactions both differ from the previous case. It is thus necessary to study the hydrodynamic interactions and their impact on the aggregation process as well as on the final clusters.

To do so, we can introduce hydrodynamic interactions between particles by means of the configuration-dependent $3N \times 3N$ diffusion tensors $\mathbf{D}^{tt}$, $\mathbf{D}^{tr}$, $\mathbf{D}^{rr}$. The two tensors $\mathbf{D}^{tt}$ and $\mathbf{D}^{rr}$ account for, respectively, the translational diffusion and the rotational diffusion, while the tensor $\mathbf{D}^{tr}$ stands for the coupling of rotational and translational motions. This last tensor is equal to zero when hydrodynamics interactions, or **HIs**, are neglected. In this case, $\mathbf{D}^{tt}$ and $\mathbf{D}^{rr}$ become diagonal and constant matrices. Their eigenvalues are then equal to D_0^t and D_0^r, the translational and rotational diffusion coefficients at infinite dilution. Those diffusion coefficients are related to the particles diameter by Stokes laws. Those three tensors are subtensors of the grand diffusion tensor :

$$\mathbf{D} = \begin{pmatrix} \mathbf{D}^{tt} & \mathbf{D}^{tr} \\ \mathbf{D}^{rt} & \mathbf{D}^{rr} \end{pmatrix}. \tag{3.25}$$

By considering those diffusion tensors and the magnetic interaction potential, Brownian dynamics simulations were used to investigate the system with and without HIs, notably by Jäger *et al.* in 2013 [74]. This allows for highlighting the specific impact of hydrodynamic interactions. In this context, the positions of the particles regarding time can be expressed as following

$$\begin{aligned} \vec{r}_i(t+\Delta t) =& \vec{r}_i(t) + \frac{1}{k_B T}\sum_j \mathbf{D}_{ij}^{tt}\vec{F}_j\Delta t \\ &+ \frac{1}{k_B T}\sum_j \mathbf{D}_{ij}^{tr}\vec{T}_j\Delta t + \vec{R}_i(\mathbf{D},\Delta t)\times\vec{e}_i(t), \end{aligned} \tag{3.26}$$

while their orientation $\vec{e}_i$ evolves as

$$\begin{aligned}\vec{e}_i(t+\Delta t) =&\vec{e}_i(t) + \left(\frac{1}{k_B T}\sum_j \mathbf{D}^{tt}_{ij}\vec{F}_j\Delta t + \frac{1}{k_B T}\sum_j \mathbf{D}^{tr}_{ij}\vec{T}_j\Delta t\right) \times \vec{e}_i(t) \\ &+\vec{R}_i(\mathbf{D},\Delta t)\times\vec{e}_i(t).\end{aligned} \tag{3.27}$$

In these equation, $\vec{F}$ and $\vec{T}$ refer respectively to the magnetic force coming from the surrounding particles, and to the magnetic torque coming both from the surrounding particles and the external magnetic field. Those forces and torques are the same as investigated before in the previous subsections. $\vec{R}_i$ stands for the random displacements and behave as

$$\langle \vec{R}_i \rangle = 0, \tag{3.28}$$

$$\langle \vec{R}_i(\Delta t)\vec{R}_j(\Delta t)\rangle = 2\vec{D}_{ij}\Delta t. \tag{3.29}$$

From Eq.(3.26), it is noteworthy that $\mathbf{D}^{tr}$ allows for the coupling of torques acting on the particles, or their rotational motion, to their translational motion. Specifically, the particles rotational motion induces a fluid flow that impacts the translational motion of surrounding particles. Simulations incorporating these equations, both with and without hydrodynamic interactions, highlight the distinctive effects of such interactions.

These results suggest that HIs do not prevent cluster formation. However, they do appear **to reduce the maximum frequency** at which aggregation occurs, as illustrated in Fig. 3.5, from Jäger *et al.* [74]. Moreover, HIs **accelerate the clustering process** and are the primary cause of **cluster rotation**. More precisely, it is the coupling between the rotational and translational motion that drives this rotation. Indeed, the magnetic torque-induced rotation of a particle leads to the translation of its neighbours through hydrodynamic coupling, resulting in the collective rotation of the entire cluster [76].

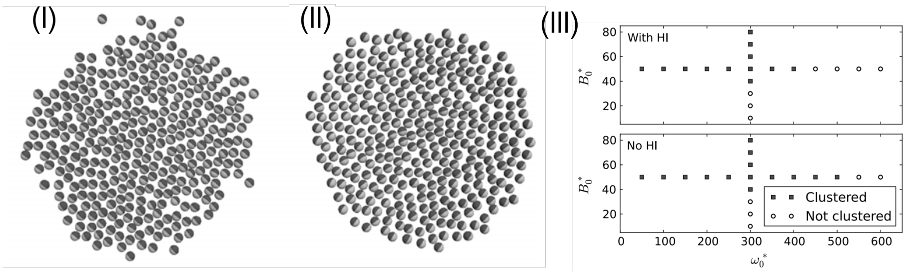

Figure 3.5: Figures modified from Jäger *et al.* [74]. (I) and (II) show snapshots of the simulation results, illustrating the aggregation into disk-like clusters and the influence of hydrodynamic interactions on the system. In (I), no HIs are computed, while in (II), all hydrodynamic couplings are considered. In (III), the comparison between the case with HIs on top and with no HIs below show that the maximum frequency of clustering is reduced with HIs.

Those two hydrodynamic effects are depicted in Fig. 3.6, also from Jäger *et al.*. Lastly, HIs also impact **the structure of the cluster** itself, although this aspect will not be discussed further here [76, 77].

3.3.4 Transition from chains to disk-like clusters : experimental observations

The aggregation into rotating disk-like clusters has been observed **experimentally** by many research teams [24, 30, 76, 77], including Nagaoka *et al.* [75], wich confirm that the magnetic field's rotational frequency plays a major role regarding the resulting structure.

To investigate the cluster formation, they used a high-speed video camera and superparamagnetic particles with an average diameter of $1.82 \pm 0.59\,\mu$m. Those particles were suspended in water, with a volume fraction of 0.081, and confined in a 2D configuration between two glass plates. During the experiments, they applied first a constant magnetic field in the plane of the suspension for 20 min, then made it rotate in the same plane at a frequency of 0.1 Hz for another 20 minutes.

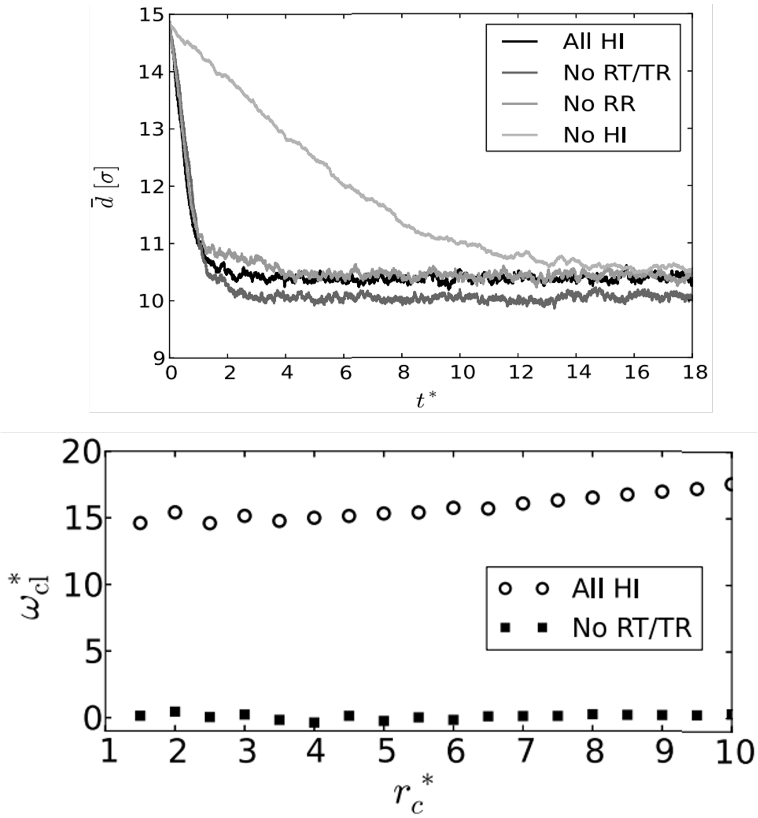

Figure 3.6: Figures modified from Jäger *et al.* [74]. The top plot shows the mean distance between particles over time, highlighting that HIs accelerate the aggregation process. The bottom plot represents the mean angular velocity of the particles around the cluster center as a function of their distance from the center. This demonstrates that HIs are entirely responsible for the cluster global rotation.

The rotational field frequency was then increased to 2 Hz and 10 Hz, each for 20 minutes. The resulting structures are displayed in Fig. 3.7 and indicate that in these conditions, the transition from chains to disk-like clusters occurs around a critical frequency of 2 Hz. Besides the **rotational frequency**, other key factors found to influence aggregation and clustering dynamics include **magnetic permeability**, solvent **viscosity**, and colloid **magnetization**.

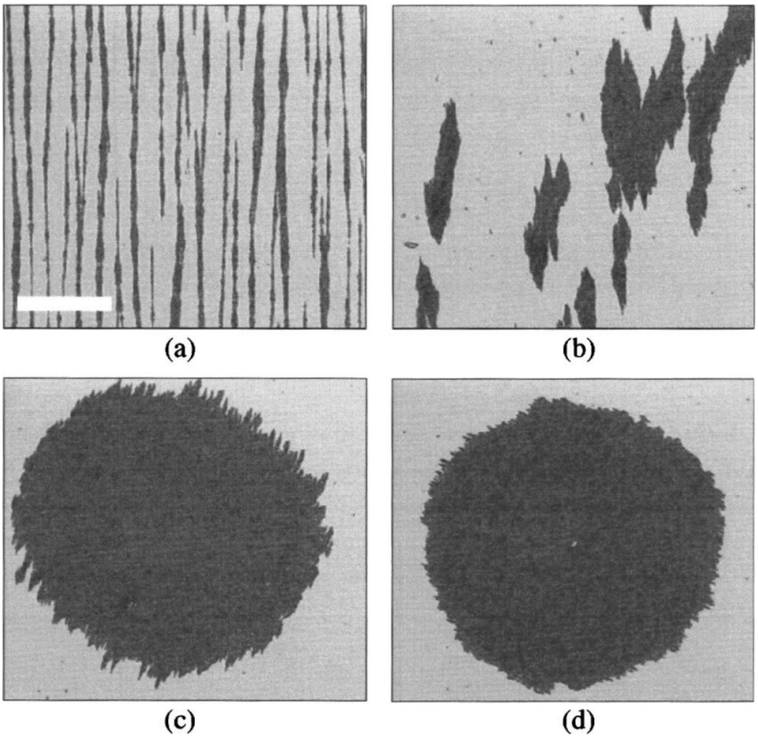

Figure 3.7: Figure from Nagaoka *et al.* [75]. Experimental snapshots showing the diversity of structures induced by a rotating magnetic field applied to superparamagnetic colloids. In (a), the magnetic field is constant and oriented upward. The magnetic field is rotating at a frequency of 0.1 Hz in (b), 2 Hz in (c) and 10 Hz. The inset scale bar represents 100 μm.

In parallel, Melle *et al.* [67, 70, 78] observed a **crossover frequency** between chains and disk-like clusters using dichroism experiments, and estimated its value between 1 Hz and 10 Hz, as depicted in Fig. 3.8. In those experiments, the magnetic particles were prepared into suspensions with 50% glycerol and volume fraction ranging from $\phi \sim 0.001$ to $\phi \sim 0.02$. The use of the scattering dichroism allow to measure time evolution of both the dichroism, $\Delta n''(t)$, and the orientation of the aggregates, $\theta''(t)$.

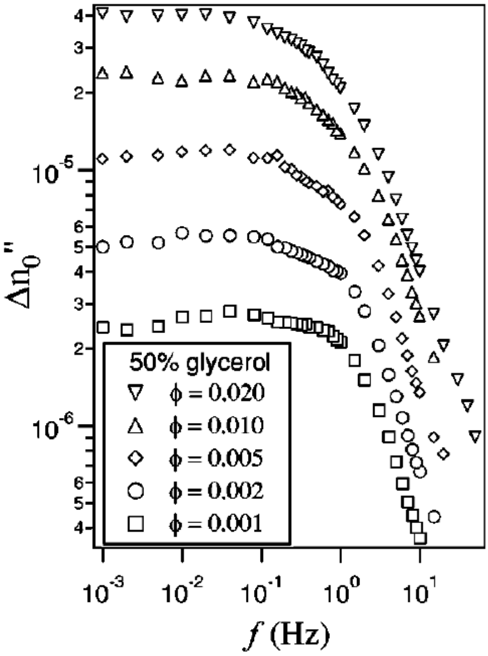

Figure 3.8: Figure adapted from Melle *et al.* [78], showing the variation of steady dichroism with the magnetic field's rotational frequency for different superparamagnetic colloids volume fractions. Before the crossover frequency, the dichroism does not vary with the magnetic field's rotational frequency. Beyond this point, the dichroism decreases significantly with frequency, indicating the break up of the chains.

The measure of $\Delta n''(t)$ gives the difference between the extinction of the incident light with polarization parallel or perpendicular to the long axis of the aggregates, and $\Delta n_0''$ correspond to the dichroism when the equilibrium is reached, or steady dichroism, which is shown in Fig. 3.8. This steady dichroism is constant regarding the field frequency below f_c, the crossover frequency. However, it suddenly decreases once the field frequency surpasses f_c. This sudden decrease in steady dichroism is due to the **break up** of the chains and the formation of **isotropic clusters**, which appear to rotate at a slower rate than the external magnetic field. Melle *et al.* also showcased a linear dependence on the magnetization squared and the inverse of the viscosity.

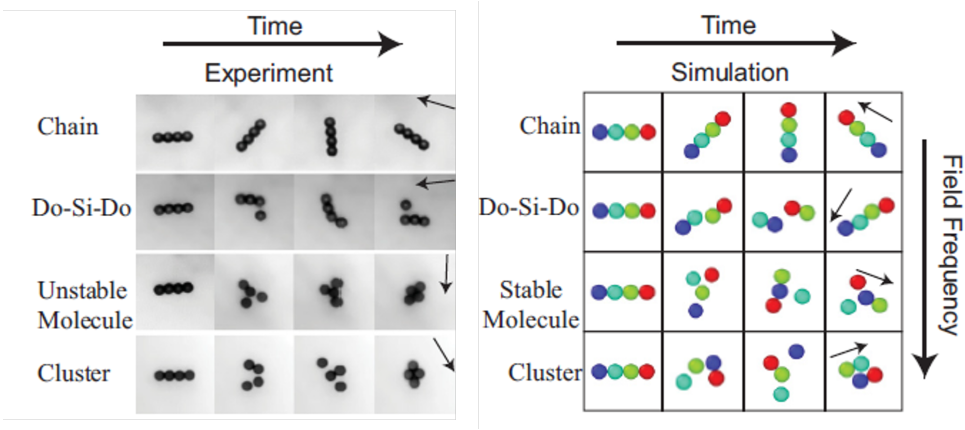

Figure 3.9: Figure adapted from Abdi *et al.* [79], with on the left snapshots of long-term experiments. On the right, the corresponding simulations. Each row from top to bottom corresponds to an increasing rotational frequency, while time increases in each column. A transient chaotic behavior is captured in the last two rows, leading to two different configurations after a long time : the (un)stable molecule and the close-packed cluster.

However, the crossover frequency does not seem to depend on the volume fraction. Both Nagaoka *et al.* and Melle *et al.* used colloidal systems comparable to those used in this thesis, and their work therefore constitutes a valuable benchmark for our experiments.

The transition mechanism from chains to clusters has been studied in detail by Abdi *et al.* [79] for short chains made of four colloids at intermediate rotational frequencies, using both experimental and numerical approaches. This system of isolated chains made of four colloids constitutes the simplest scenario in which the dynamics remain rich and nontrivial. The colloids used in their study have a slightly larger diameter of 2.8 μm and are suspended in a water-glycerol solution.

By tracking the chains through optical microscopy and numerical simulations, they identified two distinct dynamics that occur above a critical rotational frequency : the **(un)stable molecule** and the **close-packed cluster**. These two dynamics are illustrated in Fig. 3.9, with results from both experiments and simulation. The top row corresponds to frequencies at which the chain follows the magnetic field rotation, while the second row depicts the chain breaking apart due to hydrodynamic forces. In this case, the main chain breaks into two smaller chains that continue to rotate periodically with the field, thus reforming periodically the main chain. In the third and fourth rows, the rotational frequency is high enough to render the magnetic interactions isotropic. As previously stated, the long-term resulting structures in this situation are **disk-like clusters**. However, the short-time response of the chain consists of a **transient chaotic motion**. The molecule configuration (third row) was observed as stable only with the simulations and not in the experiments, where it remains unstable. The only stable structure when the magnetic interactions are isotropic is thus the closely packed clusters.

3.4 Overview

Superparamagnetic colloids suspended in an aqueous medium and exposed to an external magnetic field are influenced by both **magnetic** and **hydrodynamic** interactions. The magnetic interactions, due to the applied magnetic field, tend to **aggregate the particles into clusters**, while the hydrodynamic interactions arise from the **particles motion into a viscous fluid**. The structure of the clusters mainly depends on the characteristics of the magnetic field, such as its intensity or frequency if it varies periodically over time. The hydrodynamic interactions vary with the motion of the particles in the fluid, driven by the magnetic interactions.

For a **constant** magnetic field, the particles aggregate into **chains oriented along the external field**. For a magnetic field that rotates over time, the resulting cluster structure depends primarily on the rotation frequency.

Below 1 Hz, the particles form **chains that rotate along with the magnetic field**. As the rotational frequency increases, the viscous drag on the extreme particles of the chain causes the chain to break at a certain length. The breakup frequency is thus inversely proportional to the medium viscosity, and **the chain length decreases with increasing rotational frequency**.

Above the estimated value of 1 Hz, the magnetic interactions become **isotropic**, leading to the formation of **disk-like clusters** instead of chains, as the magnetic field rotates too fast for the particles to follow. Before aggregating into closely-packed clusters, the particles undergo a transient chaotic behavior. The hydrodynamic interactions also play a major role in clustering, as they accelerate the aggregation. Moreover, they cause the clusters to **rotate** through the coupling between the rotation of one particle and the translation of its neighbours.

All possible structures arising from the application of a rotating external magnetic field are represented in Fig. 3.10. The main parameter governing the form of the resulting aggregates being **the magnetic field rotational frequency**, the different structures are classified based on the frequency at which they occur.

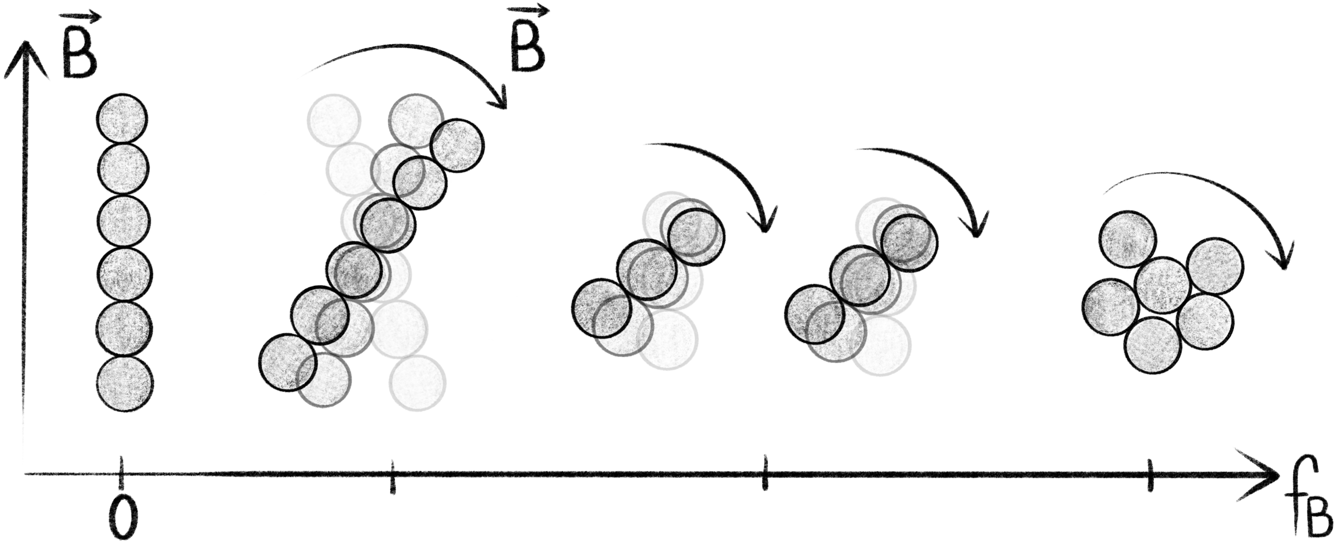

Figure 3.10: Schematic drawing of the various structures formed when a rotating magnetic field is applied to superparamagnetic colloids. On the far left, the case where the magnetic field is constant over time is illustrated. When the magnetic field is rotating, the observed structures change with its rotational frequency. They go from long chains rotating with the frequency to shorter chains, due to the viscous drag in the surrounding fluid. When the frequency exceeds 1 Hz, the magnetic interactions become isotropic, leading to the formation of disk-like clusters that rotate slower than the magnetic field.

4

Beyond the Plane

Expanding 2D structures to the 3D realm

As described in the previous chapter, superparamagnetic colloids subjected to a homogeneous external magnetic field in a 2D configuration aggregate depending on the characteristics of the applied field. At the microscopic level, this leads to different structures such as chains or disk-like clusters. The remaining question is whether these structures persist in a **3D configuration**. If they do, they could induce **macroscopic effects**, since suspension instability against settling could occur, as particle size is a crucial parameter regarding stability. Aggregates in a 3D configuration would be larger than individual particles, potentially leading to **sedimentation**. Conversely, intricate **networks** could form, and these structures may be useful once pinned by polymerizing or freezing the continuous liquid phase to produce composites called ”field-structured”. These materials exhibit distinctive behaviors regarding their permittivity, conductivity, and optical attenuation, making them valuable for applications like chemical sensors or thermal switches [80–82]. In this chapter, we will provide an overview of the current knowledge in this area.

4.1 Constant magnetic field

Starting first with considering an **homogeneous static magnetic field**, as we did while investigating the microscopic 2D configuration, both simulations and experiments [80, 83–85] result in **chain-column** structures. These structures exhibit a dual-scale organization: local crystalline order at a smaller scale and mesomorphic order at a larger scale. The chain-column structures align with the direction of the magnetic field, as depicted in Fig. 4.1.

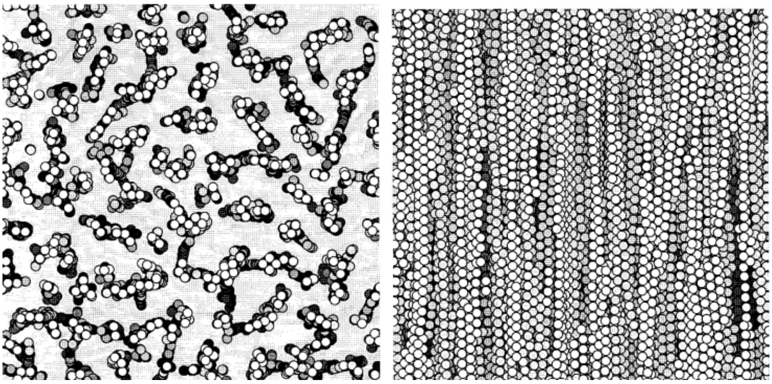

Figure 4.1: Simulation results from Martin *et al.* [80] depicting chain-column structures for $\phi = 0.1$ under a uniaxial field. Left: view parallel to the field axis; Right: view perpendicular to the field axis.

Simulation results particularly highlight that low-concentration systems, such as those examined in this thesis, display well-defined columnar structures. As concentration increases, there is a transition to a branched network with cavities. Detailed analysis of particle arrangements reveals the formation of short chains at low concentrations, which coalesce into complex structures such as cruciform defects and small hexagonal sheets aligned with the z-axis. This merging of chains into columns has been experimentally observed as well [86]. Another notable feature is the ”zippering” phenomenon, where chains align and merge, forming small sheets and bridges between the columns. These ”small hexagonal sheets” can be considered analogous to the ribbons observed in 2D (see Section 3.2).

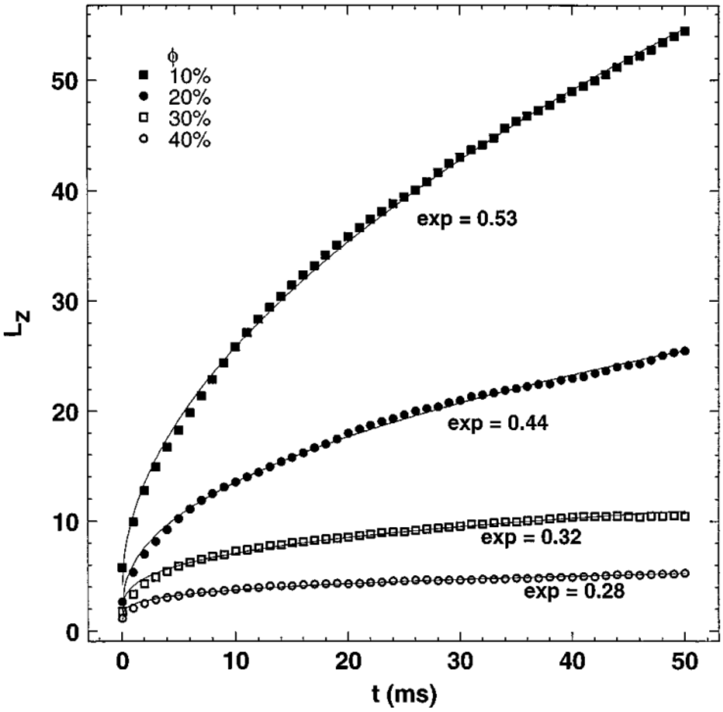

Figure 4.2: Figure from Martin *et al.* [80] picturing the optical attenuation length in the direction of the field plotted as a function of time, in the case of a uniaxial field. The slow growth is effectively described as a power law in time, with an exponent depending on the colloidal volume fraction.

An interesting consequence of this coarsening at low concentrations is the increase in the **optical attenuation length** L_z along the field axis. Indeed, as columns form over time, the sample becomes more transparent, implying a gradual increase in the optical attenuation length, which evolves as a power law. The exponent of this power law depends on the concentration: the lower the concentration, the higher the exponent, thus the quicker the increase of L_z. This phenomenon is easily probed experimentally and provides a convenient method for verifying the formation of chain-column structures.

4.2 Rotating magnetic field

Having described the uniaxial field and its resulting structures, we now consider the case of a **homogeneous rotating fiel**d in a biaxial configuration. In this scenario, the potential introduced in Eq. 3.24 has to be modified. Indeed, in 3D, we must account for θ_{ij}, the angle between $\vec{r}_{ij}$, i.e the vector linking the particles i and j, and the z-direction, i.e the direction perpendicular to the magnetic field plane [87]. This leads to a new time-averaged potential, derived under the same assumptions as Eq. 3.24 and based on the same dipole-dipole potential:

$$U_{iso}^{3D} = -\mu^2 \frac{1 - 3\cos^2\theta_{ij}}{2r_{ij}^3}. \tag{4.1}$$

This potential is attractive if $\cos^2\theta_{ij} < 1/3$, which corresponds to particles i and j being close to the same plane as the field. On the opposite, if $\cos^2\theta_{ij} > 1/3$, the potential is repulsive, causing particles to repel each other. Consequently, a particle will be attracted to others in the field plane, but repelled by those outside this plane, leading to the formation of **layers** in the field plane. This layering has been observed in experiments [88] and simulations [81, 89] across a wide concentration range, provided the magnetic field intensity is strong. As in the 2D configuration, the structures exhibit local crystalline order at small length scales and mesomorphic order at larger length scales. They also have a strong tendency to align with the field, and "staircases" connect the sheets as well, similarly to how bridges connect columns in the uniaxial case.

An interesting observation from the simulations is that chains initially form within the sample [81]. These chains are rapidly incorporated into hexagonal sheets and, therefore, do not appear to play a significant role in the overall structure formation. However, their lifetime seems to be longer at lower concentrations. For reference, the chains life-time is of the order of 1 ms in the simulation time scale, whereas hexagonal sheets are maximized after 75 ms in the simulation time scale.

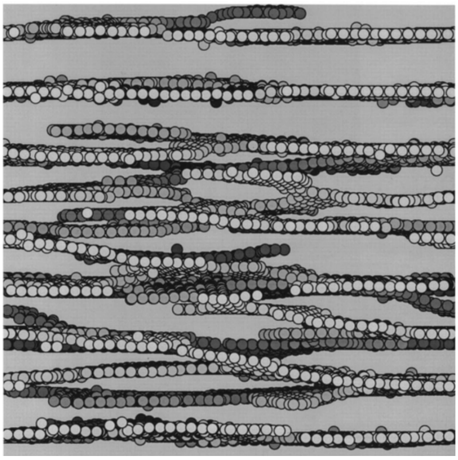

Figure 4.3: Figure from Martin *et al.* [81] showing a view parallel to the plane of the field of the sheet structures observed for $\phi = 0.1$ in the case of a biaxial field.

Similar to the uniaxial field case, the optical attenuation length increases over time, and is larger for lower concentrations. Here, the coarsening kinetics differ from the uniaxal case, as indicated by the larger exponents for the fitted power laws shown in Fig. 4.4. This discrepancy may be attributed to the fact that the sheets are weakly connected to each other, which facilitate a faster flattening of the layers.

As in the 2D case, the formation of structures, specifically layering, depends on the rotational frequency and field strength. It also varies with the dipole moment of the particles, their concentration within the surrounding fluid, and the fluid's density. More precisely, simulations show that layering occurs only within a **specific frequency range** and does not appear outside of that range [89–91]. The upper limit of this frequency range and the corresponding field intensity for layering are depicted in the phase diagram of Fig. 4.5 from Jäger *et al.* [90]. Considering the size of the particles used in this thesis, this upper limit appears to be over 1 kHz. It should be noted that hydrodynamic interactions were not considered in this diagram, and the authors anticipate these interactions to lower the upper limit.

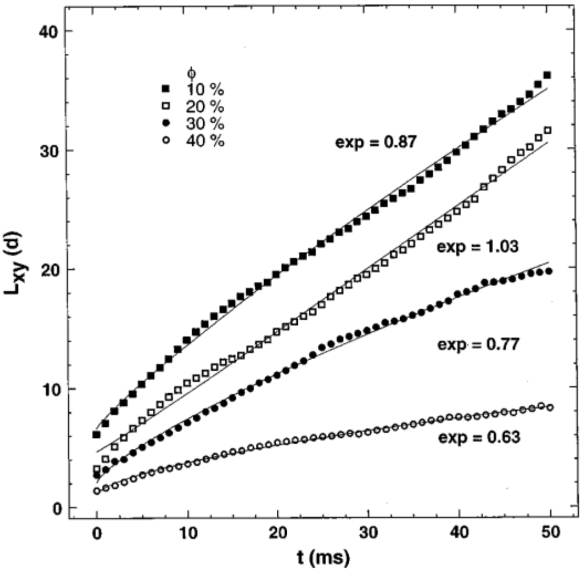

Figure 4.4: Figure from Martin *et al.* [81] picturing the optical attenuation length in the plane of the field plotted as a function of time, in the case of a biaxial field. The optical attenuation length progressively increases with time, as it was the case for a uniaxial field.

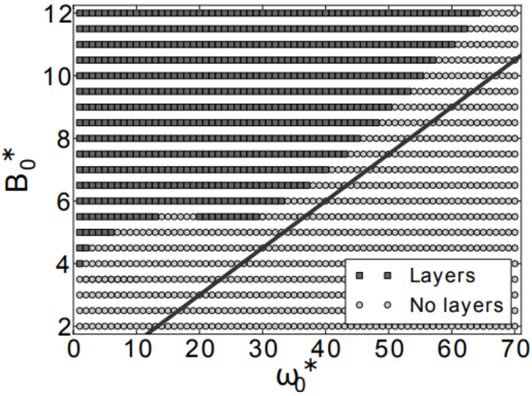

Figure 4.5: Figure from Jäger *et al.* [90] representing the configurations of magnetic field intensities and rotational frequencies where layers are formed (full squares) or not (empty circles).

The lower limit of the frequency range, investigated through similar simulations [91], is estimated around 500 Hz, although its interaction with magnetic field intensity has not been studied. Given the frequencies examined in this thesis, layering is not expected to occur, although the hydrodynamic interactions and the magnetic field intensity could challenge this assumption. The dipole moment, colloidal concentration and fluid density on the other hand seem to influence the structure of the sheets and their number. Indeed, strong dipole moments, low concentrations and low densities correlate with enhanced layering [91].

4.3 The case of rotating rods

If the rotation frequency is insufficient to allow the interaction potential to be time-averaged, as presented in the previous section, we can expect **rotating chains**, or more likely rotating columns, to form in 3D, similarly to the 2D configuration. Should this occur, the observations would resemble those of rod-shaped particles suspended in a fluid and rotating in three dimensions. This specific scenario has been investigated both experimentally and numerically, and the corresponding conclusions are presented hereafter.

Klein *et al.* and others experimentally studied the light transmission through a cell containing a suspension of Ni nanorods when applying a **constant** magnetic field [92, 93]. These nanorods, obtained through electrodeposition of nanoparticles, exhibit a single magnetic domain with a predominantly uniaxial shape anisotropy. This characteristic implies that their magnetic moment aligns preferentially along their long axis, as it is the case for chains of superparamagnetic colloids under an external magnetic field. Their findings are comparable to those presented in Section 4.1 for spherical colloids submitted to a uniaxial field.

Similar rods were studied for the case of a biaxial **rotating** magnetic field, notably by Günther *et al* through experiments with magnetic fields rotating at frequencies from 10 to 500 Hz and intensities from 10 to 80 G.

When rotating in 2D, the nanorods exhibit the exact same behavior as the chains described in Section 3.3. Specifically, they follow the rotating field as long as the rotation rate remains below a critical frequency but fail to follow the field's rotation once this critical frequency is exceeded [94–96]. The primary difference between the chains and the rods is that the chains break up when they can no longer follow the magnetic field rotation, as the phase lag angle becomes larger than θ_M. In contrast, the break-up is not an option for the rods; instead, θ fluctuates periodically with time while increasing [95, 96].

In a three-dimensional configuration, the orientation of the rods can be tracked by monitoring the **light transmission** through the sample. Indeed, in a setup such as the one represented in Fig. 4.6 from [97], light transmission is maximal when the nanorods are aligned with the longitudinal pair of coils, while the nanorods block the light when they are perpendicular to these coils.

The results of light detection in this setup are represented in Fig. 4.7, showing the normalized transmitted light intensity $I(t)/I_{max}$. This transmitted light intensity varies periodically with time with a doubled frequency compared to the field. Assuming all the nanorods in the sample are aligned within the x-y plane and their long axis forms an angle β with the magnetic field, the polarizability α can be expressed as [92, 97]

$$\alpha(\beta) = \cos^2(\beta)\,\alpha_1 + \sin^2(\beta)\,\alpha_2. \tag{4.2}$$

For a rotating magnetic field, this becomes

$$\alpha(t) = \cos^2(\omega t - \theta)\,\alpha_1 + \sin^2(\omega t - \theta)\,\alpha_2, \tag{4.3}$$

This is highlighted in Fig. 4.7 by representing the sinusoidal current going through the longitudinal coils (LC1-LC2), which is maximal when the magnetic field is maximal in the longitudinal direction, along with the light transmission, which is maximal when α is.

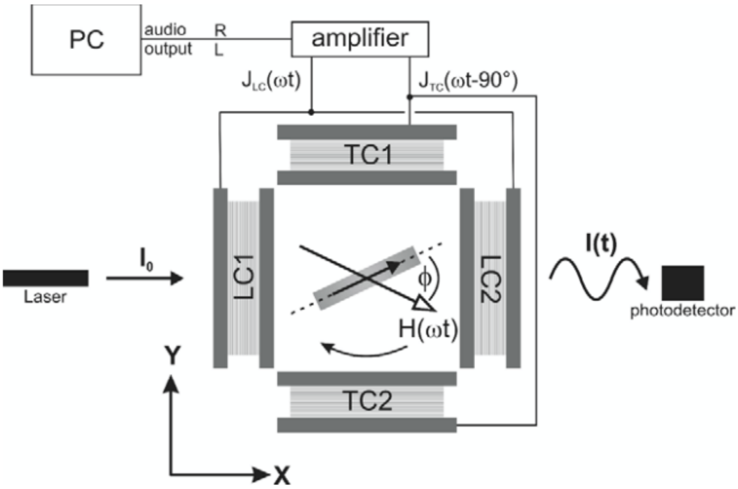

Figure 4.6: Figure from Günther *et al.* [97] representing an experimental setup for measuring light transmission. Two pair of coils, LC1/LC2 (longitudinal direction) and TC1/TC2 (transverse direction), generate a homogeneous rotating magnetic field at their center. The resulting nanorods rotation causes a periodic variation in transmitted light, which is detected by a photodetector.

By comparing these two signals, the **phase lag angle** between the nanorods and the magnetic field (noted ϕ in the figure and θ in our equations) can be measured. This phase lag angle increases linearly with the magnetic field rotational frequency, as shown in the second part of Fig. 4.7, for rotational frequencies up to 1200 Hz. Beyond this value, the phase lag saturates [98, 99]. On the opposite, increasing the magnetic field amplitude decreases the phase lag [98]. These two tendencies result from the competition between the magnetic and viscous drag torques detailed in Section 3.3. When the rotational frequency increases, the rotation speed of the rods increases, leading to a larger viscous drag torque and an increased phase lag. Conversely, a larger magnetic field amplitude increases the magnetic torque, therefore reduces the phase lag. If this behavior is observed when investigating the aggregation of superparamagnetic colloids in a three-dimensional sample, it would confirm the formation of rotating chains within the sample.

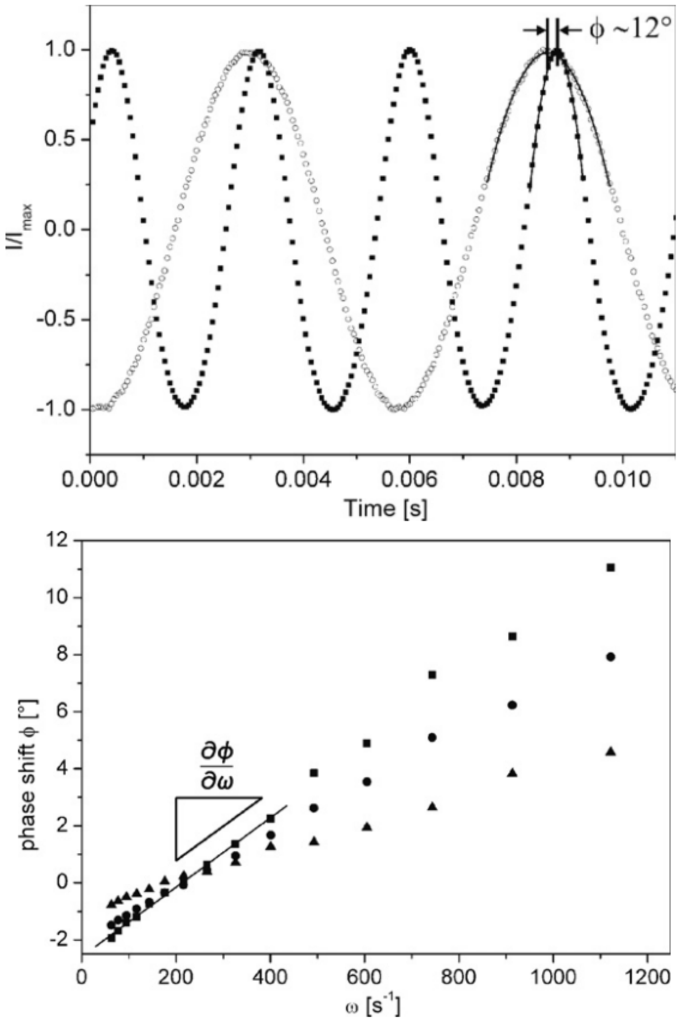

Figure 4.7: Figures from Günther *et al.* [97]. On the top: determination of the phase shift ϕ (denoted as θ in our equations) by comparing the maximum in normalized transmitted light intensity (squares) with the maximum in longitudinal coil current (circle) at $f = 178\,\text{Hz}$ and $\mu_0 H_0 = 2\,\text{mT}$. On the bottom: phase shift as a function of magnetic field frequency for three field amplitudes: $H_0 = 1\,\text{mT}$ (square), $H_0 = 1.636\,\text{mT}$ (circle), and $H_0 = 8\,\text{mT}$ (triangle).

4.4 Implications on Sedimentation

Since aggregates form in a three-dimensional configuration under the influence of a rotating magnetic fiel, we can also expect **sedimentation** to occur more rapidly. This can be understood by coming back to the **Péclet number** discussed in Section 2.3.3, which compares thermal and gravitational effects. Indeed, the aggregation into clusters larger than individual particles leads to a larger Péclet number, indicating that gravitational effects become more significant relative to thermal effects. Single particles with a radius of $1\,\mu$m correspond to $Pe = 10$, meaning that a cluster then corresponds to $Pe > 10$, which indicates instability against sedimentation.

However, it is important to distinguish between the two configurations discussed in the previous chapters. In the case of isolated aggregates, as considered in Section 4.3, the mechanism behind the sedimentation process is referred to as **cluster deposition**. Conversely, the case where connected layers rather form (described in Section 4.2) could correspond to a gel-like structure. This kind of structure is known to undergo a different sedimentation mechanism known as **collective settling**.

When **no external field** is applied [100, 101], aggregation can be induced by adding salt to the suspension, which results in strong van der Waals attraction, or by the absence of an electric double layer. This aggregation is known as *diffusion limited cluster aggregation*, or DLCA. However, when gravity is taken into account, while DLCA remains relevant at short time, sedimentation becomes significant in the clusters growth once aggregates are large enough to settle. The colloidal volume fraction, ϕ, determines the dominant mechanism: cluster deposition occurs at low ϕ, while collective settling is observed at higher ϕ.

At low volume fractions, the suspension initially appears uniform but becomes heterogeneous over time as small clusters form. These clusters settle at different velocities depending on their size, as settling velocity $\vec{v}_s$ is directly proportional to cluster size.

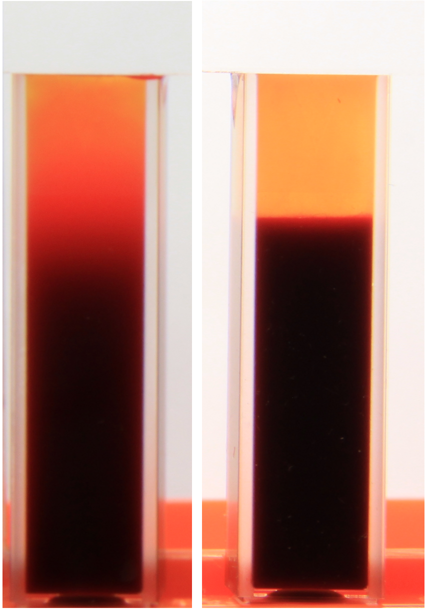

Figure 4.8: Figures obtained from Darras *et al.* [102] illustrating the two types of interface resulting from cluster deposition (left, $\phi = 0.2$) and collective settling (right, $\phi = 0.45$) for an erythrocyte suspension.

Therefore, while settling, larger aggregates sweep up smaller ones underneath, accelerating their growth. The clusters deposit on the bottom of the sample in what is called a sediment, which compacts slowly, and the sample becomes progressively clearer. This results in a diffuse interface illustrated in the left picture of Fig. 4.8.

At higher volume fractions, the aggregates quickly form a network, leading to a gel structure. This gel structure then settles under its own weight, creating a sharp interface between the clear medium fluid above and the settling suspension below [103]. This sharp interface is illustrated by the picture on the right in Fig. 4.8. The height of this interface then decreases until equilibrium is reached. At even higher values of ϕ, the gel may not settle at all, with gravity either limiting aggregate size or inducing sedimentation before network formation can occur. Moreover, if the attraction between the particles is weak ($U \sim k_B T$), the gel may become mechanically unstable and collapse. This leads to various potential stages in gels sedimentation, ranging from slow compression to fast sedimentation or smooth collapse [102, 104–106].

In the case where a **constant and uniform magnetic field** is applied to a very dilute suspension ($\phi < 0.1$), individual chains are observed. These chains are larger than individual particles, but their shape is anisotropic, where individual particles are spherical, thus isotropic. This leads to two different diffusion coefficient : $D_{||}$ for the diffusion parallel to the chain's long axis, and $D_{\perp}$ for the diffusion perpendicular to this axis.

To determine these diffusion coefficient, we model once again the chains as rods with a length $L = 2R\,N$ (with N the number of particles and R their radius) [64, 107, 108]. The hydrodynamic forces on such rods due to the surrounding fluid are derived from solving the Navier-Stokes equations for a long rod composed of individual beads [109, 110]. In this situation, the hydrodynamic forces are approximately identical for all of the beads, at the exception of the ones close to the rod ends. For a sufficiently long rod, these can be neglected, and we find

$$\vec{f_{||}} = \hat{\gamma}_{||}\,\vec{v}_{||}, \tag{4.4}$$

$$\vec{f_{\perp}} = \hat{\gamma}_{\perp}\,\vec{v}_{\perp}, \tag{4.5}$$

where $\gamma_{||}$ and $\gamma_{\perp}$ are the translational friction coefficients of the hydrodynamic forces parallel and perpendicular to the rod's long axis, respectively. Their expressions are [64, 111–113] :

$$\hat{\gamma}_{||} = \frac{4\pi\eta NR}{\ln(N)}, \tag{4.6}$$

$$\hat{\gamma}_{\perp} = \frac{8\pi\eta NR}{\ln(N)}. \tag{4.7}$$

The diffusion coefficient is defined as $D = k_BT/\gamma$, leading to these two diffusion coefficient, parallel or perpendicular to the rod axis (with $N = L/2R$) :

$$D_\parallel = \frac{k_BT}{2\pi\eta L}\ln\left(\frac{L}{2R}\right), \tag{4.8}$$

$$D_\perp = \frac{k_BT}{4\pi\eta L}\ln\left(\frac{L}{2R}\right). \tag{4.9}$$

This means that $D_\parallel \sim 2D_\perp$, which indicates that the diffusion parallel to the rod axis is greater than the diffusion perpendicular to this axis.

We consider the case where the magnetic field, hence the chains/rods, are oriented horizontally, while the sedimentation speed $\vec{v}_s$ is oriented vertically. This sedimentation speed is obtained by considering the force balance on the body of interest, and gives the result in Eq. 2.17 for a spherical particle. We can express this equation using the corresponding friction coefficient for a single sphere in an infinite dilution, $\gamma = 6\pi\eta R$, which gives

$$v_{s,1} = \frac{\frac{4}{3}\pi R^3 \Delta\rho\, g}{\gamma}. \tag{4.10}$$

For a chain made of N particles, when using the friction coefficient $\gamma_\perp$ corresponding to the vertical movement, we have

$$v_{s,N} = N\,\frac{\frac{4}{3}\pi R^3 \Delta\rho\, g}{\gamma_\perp}. \tag{4.11}$$

Using the expression in Eq. 4.9, this becomes

$$v_{s,N} = \frac{R^2 \Delta\rho\, g}{6\eta}\ln(N). \tag{4.12}$$

This confirms that longer chains settle faster than smaller ones, similar to the behavior of larger clusters in the context of DLCA.

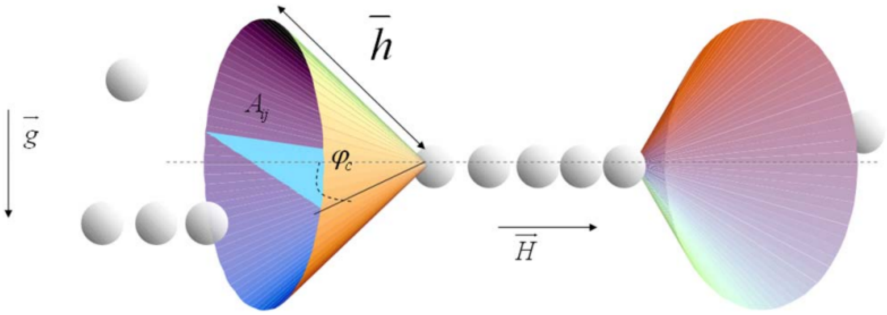

Figure 4.9: Figure from [64] illustrating the attractive zones at the ends of a chain composed of superparamagnetic colloids. The magnetic field direction is indicated by $\vec{H}$, and is perpendicular to $\vec{g}$, hence to the sedimentation speed $\vec{v}_s.h$ denotes the effective range of the net magnetic interactions, while φ_c represents the aperture angle of the attractive zone. A_{ij} stands for the combined crossed section of two aggregates of different size i and j.

As in the 2D case, the particles aggregate head-to-tail and repel each other laterally (see Fig. 3.1). Once aggregated into chains, they exhibit two attractive zones at the chains end, as well as a repelling zone on the sides. In a 3D configuration, the attractive zones can be represented as shown in Fig. 4.9 from [64]. Since longer chains settle faster than smaller ones, these attractive zones sweep a larger portion of the sample, enhancing aggregation for those chains. Consequently, the large chains grow faster, and their sedimentation speed increases, further enhancing differential sedimentation. Therefore, the effects of sedimentation on aggregation become more pronounced over time, while magnetic aggregation prevails initially.

Considering finally a **homogeneous rotating magnetic field** in the plane perpendicular to the sedimentation direction, the two situations mentioned before can occur.

]

First, if the rotational frequency and colloidal volume fraction are sufficiently low, leading to the formation of individual aggregates rather than layers, we enter the cluster deposition regime. In this case, the situation resemble that of a constant magnetic field. Indeed, taking as reference a system rotating at a constant speed with the external magnetic field, the two situations are similar, with the key difference being the viscous drag caused by the rotation of the chain in the surrounding fluid (see Section 3.3). Thus, experimentally, we can expect to observe a **diffuse sedimentation front**. Additionally, based on the results for rotating rods discussed in the previous section, we should also measure a **periodic variation in the transmitted light** through the sample.

On the other hand, if the rotational frequency falls within the range that allows for layer formation, the resulting network structure could lead to collective settling instead. In this scenario, a **sharp sedimentation front** should be observed, with the particles accumulating at the bottom and the medium fluid remaining on top.

As we did for the 2D configuration, we propose a **visual summary** of the structures that emerge when a rotating magnetic field is applied to a three-dimensional system experiencing sedimentation in Fig. 4.10. This overview encapsulates the structures discussed in this section and underscores the pivotal role of the magnetic field's rotational frequency. Alongside the rotational frequency, the colloidal volume fraction and magnetic field intensity, which are held constant in this context, also play crucial roles. The proposed overview is framed within the context of a dilute suspension, where $\phi < 0.1$, and assumes that the magnetic field is sufficiently strong to induce magnetic aggregation.

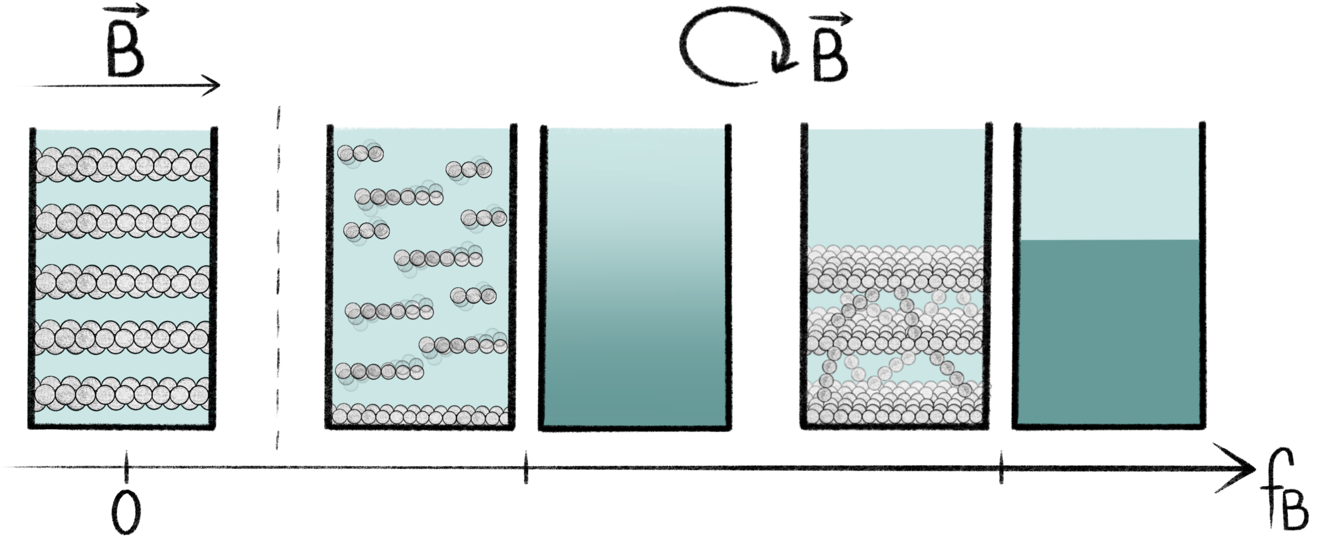

Figure 4.10: Schematic representation of the three-dimensional structures formed in a suspension of superparamagnetic colloids subjected to an external magnetic field $\vec{B}$ confined to the horizontal plane. When $\vec{B}$ is constant, chain-columns are observed. When $\vec{B}$ varies over time, two structures are expected depending on the frequency: rotating chains at low frequencies where the chains can follow the field, and connected sheets at higher frequencies where the interaction potential can be time-averaged. The corresponding sedimentation fronts for each of these two cases are also depicted.

5

From Chains to Disks

Experimental spin on the structural transition

The study of superparamagnetic colloids suspensions under the influence of external magnetic fields has revealed a variety of fascinating behaviors driven by the interplay of magnetic and hydrodynamic interactions. We described in Section 3.3 how these interactions lead to the formation of distinct structures such as chains and disk-like clusters when the magnetic field varies periodically over time. The nature of these structures was found to be primarily governed by the characteristics of the magnetic field and the suspension, particularly the **field rotational frequency** and the **colloidal volume fraction**.

In a constant magnetic field, superparamagnetic colloids align into chains oriented along the field direction. Under the influence of a rotating magnetic field, their behavior changes significantly depending on the rotational frequency of the field. At frequencies lower than 1 Hz approximately, the colloids form rotating chains. As the frequency increases, viscous drag forces cause these chains to shorten and break-up, leading to the formation of disk-like clusters when the frequency exceeds a critical threshold.

This dynamic transition and the resulting structures have been studied extensively, yet several aspects of the process, particularly in the early stages of cluster formation and the transition dynamics, remain poorly understood. In particular, the **transition** between the configurations where chains are supposed to form, and the ones where disk-like clusters are expected, is still challenging to comprehend. For that reason, we chose to investigate experimentally these early-stages in order to better characterize the transition. More specifically, we aim to investigate the **initial aggregation** behavior of colloids before they form disk-like clusters and to eventually **develop a model** to characterize the temporal evolution of the suspension, focusing on the proportion of chains and disk-like clusters over time under various frequencies and volume fractions. By addressing these objectives, this work seeks to fill the existing gap in understanding the transitional dynamics and early aggregation stages in such systems.

In the following chapter, we present the results of these experimental investigations, showing that the colloids aggregate into rotating chains at rotational frequencies larger than expected. Over time, these chains interact and aggregate into disk-like clusters, resulting in a **heterogeneous mixture** of chains and disks within the sample. Additionally to those experimental results, we propose a **model** to describe the temporal evolution of the suspension, providing insights into the proportion of chains and disk-like clusters as a function of time for different rotational frequencies and colloidal volume fractions. The upcoming sections will detail our experimental setup, the observed behaviors of the colloids, and the developed model.

5.1 Experimental Setup

In order to conduct experiments of superparamagnetic colloids subjected to a rotating magnetic field, it is necessary to consider two main elements: the magnetic field and the colloidal suspension. On the ”magnetic” side, we need to produce a tunable magnetic field and ensure its homogeneity at the sample level. On the ”colloidal” side, we require stable suspensions of micrometric superparamagnetic colloids that can be diluted to various volume fractions. Finally, once the experiment is set up, we have to observe the results at the microscopic level. In the following subsections, we detail how we achieved these goals and present the resulting experimental setup.

5.1.1 Magnetic field

First, we consider the generation of the magnetic field. A magnetic field can be obtained using a magnet, or an electric current through a coil. Since we need it to be homogeneous at the sample level, we chose to use a pair of coils in the Helmholtz configuration. This configuration consists of two identical circular coils placed parallel to each other at a distance equal to their radius. Both coils produce an equivalent magnetic field due to the same current going through them, and the resulting magnetic field at the center of the coils is known to be homogeneous. By using two pairs of identical coils, placed perpendicular to one another, we can vary the magnetic field at the center over time. Specifically, we use two phase-shifted alternating currents to generate the rotating magnetic field. The electric current is produced by a programmable function generator AFG3022C from Tektronix, and has a sinusoidal form. A dephasing of 90° is introduced in one of the pair to obtain the rotation of the field.

Since the radius of the coils we used is slightly larger than the distance between them, we measured the magnetic field at the center with a Hall probe to test its homogeneity. Measurements were taken at intervals of 0.25 mm and demonstrate that a sample which size does not exceed 5 mm will experience an homogeneous magnetic field, as required. However, since each coils have a slightly different impedance, we had to adjust the current intensity in each pair in order to obtain the exact same magnetic field intensity at the center.

5.1.2 Colloidal suspension

The superparamagnetic colloids used in our experiments are polystyrene beads with ferrite inclusions. As described in Section 2.3.2, these nano-sized inclusions are at the origin of the particles magnetic properties, while carboxyl groups on the particle surfaces ensure suspension stability, as discussed in Section 2.3.3. The initial suspension of superparamagnetic colloids, commercialized by Merck Millipore (M1-070/60), has a colloidal volume fraction of $\phi = 0.1$. This suspension was diluted in distilled water and phosphate-buffered saline (PBS) to the desired volume fraction for each experiments. PBS is essential to stabilize the suspension's pH value, as the particles can be strongly influenced by ions. This buffer solution was chosen for its mineral composition, which minimizes its impact on the colloid's mobility and reduces the adsorption on the microscope slide [114]. Additionally, the pH value of PBS is close to that of blood plasma, making it a commonly used solution in biochemistry, which may be advantageous for future applications. The PBS volume fraction used in our experiments is 6.10^{-3}.

In Section 2.3.3, we showed how the size of the particles was a determinant factor in the stability against sedimentation. Therefore, we investigated the size distribution in the suspension. The manufacturer specifies a size range for the particles, from diameters of $0.7\,\mu$m to diameters of $1.3\,\mu$m, but does not indicate whether the size distribution is homogeneous. This broad range was chosen intentionally, since a uniform particle size distribution is less likely to occur spontaneously.

To characterize the particle sizes, we used a direct microscope and measured over 2800 particles from different samples. The resulting distribution shows a mean particle diameter of $1.18 \pm 0.54\,\mu$m. Some measurement inaccuracies may occur due to thermal agitation, which makes focusing difficult and can cause particles to appear slightly larger than they are in reality. The large number of objects smaller than $0.2\,\mu$m is attributed to small defects in image capture and have been excluded from the mean diameter calculation. Finally, diffraction effects may influence the size measurement of particles slightly smaller than the wavelength of visible light.

In addition to the volume fraction and the particle size, another relevant parameter to consider is the magnetic susceptibility, which is constant when the magnetic field and the magnetization are linearly related (see Eq. (2.10)). According to Fig. 5.1, provided by the manufac-

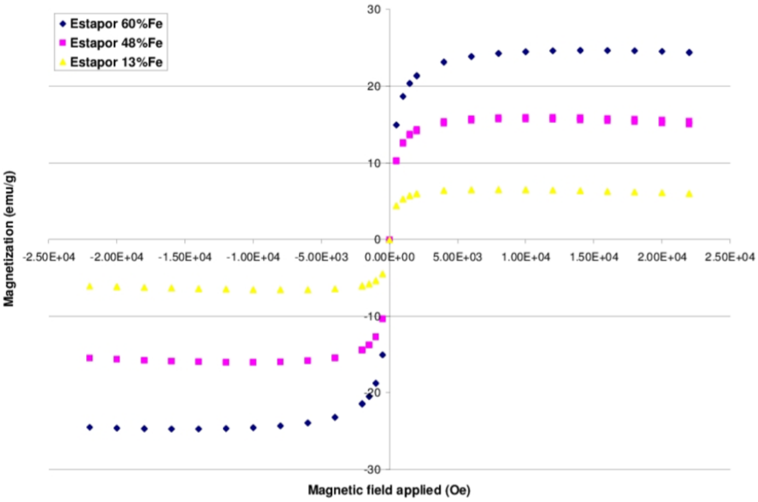

Figure 5.1: Characterization of the magnetization of the superparamagnetic colloids used during our experiments in regards to the applied magnetic field, supplied by Merck Millipore.

turer, this linear relationship holds for magnetic field intensities smaller than 1000, G. Since we will not exceed 25 G in our experiments, we can conclude that χ_m remains constant within our experimental range. Its value has been determined in previous experiments by Alexis Darras using magnetophoresis, yielding a value of 0.11 ± 0.004 [115].

Finally, the density difference between the colloids and the liquid medium is sufficient to ensure stability against settling in the short-term. However, after several hours, we do observe the sedimentation of the colloids. This sedimentation can lead to irreversible aggregation, as the weight of the particles may be sufficient to overcome the repulsion induced by the electric double layer. To prevent this aggregation during storage, we used a slow rotating plate. This rotating plate was placed in a refrigerator at a constant temperature between 4 and 8 degrees Celsius to avoid bacterial proliferation. The temperature could not be smaller than 2, since the surface carboxyl groups would not persist at such low temperatures.

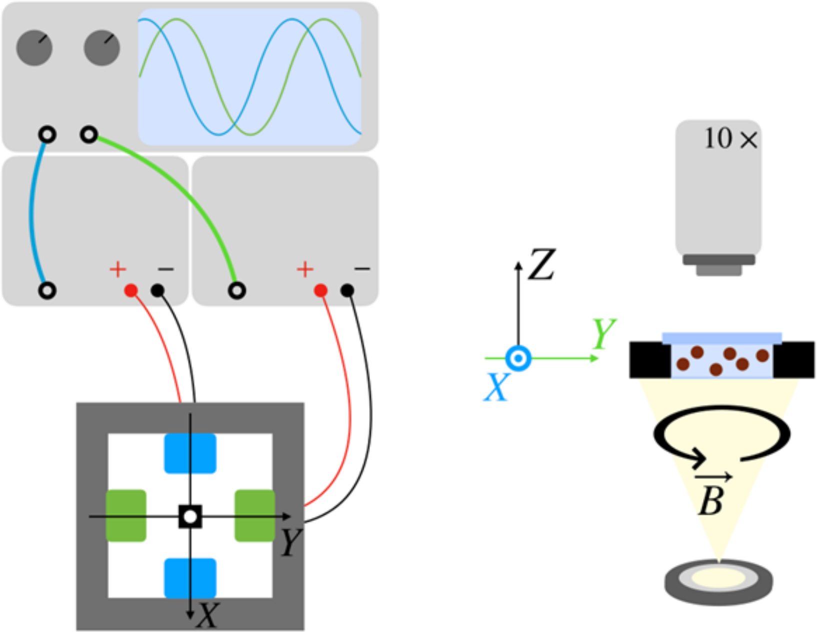

Figure 5.2: Representation of the experimental setup. A signal generator provides an alternating current, and the signal is amplified before being sent to the two pairs of coils. The phase shift between the two signals results in a rotating magnetic field in the X-Y plane. On the other hand, the frame and the sample are placed under the objective of an upright microscope.

5.1.3 Observation at the microscopic level

During the experiments, a droplet of 1 µL of the diluted solution is placed on a glass slide. We used glass slides covered with a 50 µm layer of epoxy at the exemption of a circular region of 5 mm of diameter. Another glass slide, without epoxy, is then placed on top of the first one. In this cell, the colloids' area fraction is linked to the effective volume fraction of the suspension with a linear scaling by a geometrical constant $\phi_E = \frac{2}{3}\phi^{2D}$ (see Appendix A in [115]). This cell is then placed at the center of the two pairs of coils, which are fixed to a custom-made frame. This frame was specifically design to allow the observation of the sample from the top with an upright microscope Nikon Eclipse FN1.

The microscope was connected to a MotionExtra N3 high speed camera and the images were recorded with a frame rate of 200 fps. This set-up, including the cell, the frame and the microscope, is represented in Fig. 5.2.

5.2 Influence of the magnetic field frequency

In a previous experimental study described in Section 3.3, Melle *et al.* observed, using dichroism, that between $f_B = 1\,\mathrm{Hz}$ and $f_B = 10\,\mathrm{Hz}$, the rotating chains decreased in size until they completely broke up and disappeared [78]. Given that our experiment utilizes the same colloids, in a similar concentration range, and with a comparable magnetic field amplitude, we anticipate that **rotating chain**s will form in the sample at rotation frequencies below 10 Hz. These chains are expected to follow the frequency of the field. At rotation frequencies above 10 Hz, chains are no longer expected to form, and **only disk-like clusters** should be observed in the sample. To confirm these expectations, we conducted experiments focusing on the early stages of cluster formation. In those experiments, we applied an homogeneous rotating field with a constant amplitude of 18 G and a rotational frequency f_B between 5 Hz and 30 Hz. The colloidal volume fraction was maintained at 2.10^{-3}.

5.2.1 Observations

Snapshots of the experiments are displayed in Fig. 5.3. Three different magnetic field frequencies are represented in the three lines of the figure, at 5, 15 and 30 s. First, $f_B = 5\,\mathrm{Hz}$, where **only chains** are supposed to form, which is indeed what we observed. This rotational frequency will be used as a benchmark to compare the case where there is only chains and others. Two other frequencies are displayed in the figure, $f_B = 20\,\mathrm{Hz}$ and $f_B = 30\,\mathrm{Hz}$. For this range of frequencies, we expect to observe disk-like clusters. However, it appears that chains first form before the disks, and that for the lower frequency, they last longer (at least 15 s for $f_B = 20\,\mathrm{Hz}$ compared to maximum 5 s for $f_B = 30\,\mathrm{Hz}$). At some point, **both chains and disk-like clusters** coexist in the sample, while after 30 s, only disk-like clusters seem to remain in both cases.

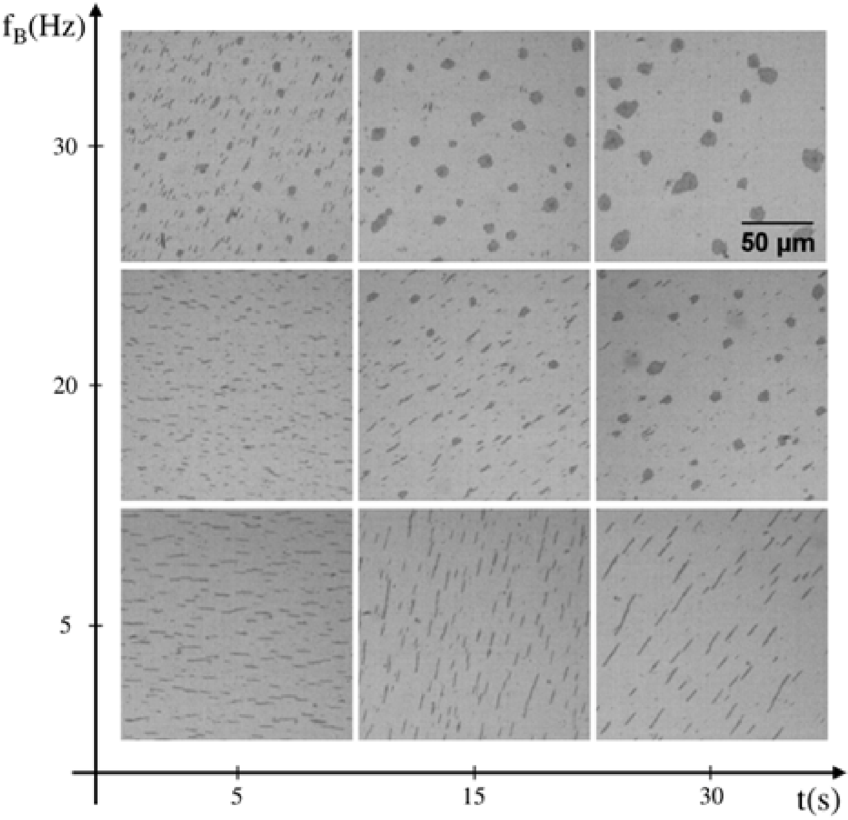

Figure 5.3: Snapshots of 3 samples under a magnetic field with a frequency of rotation of 5, 20 and 30 Hz. The activation of the magnetic field corresponds to $t = 0$ s. For the 5 Hz magnetic field, chains are observed with no significant change during the 30 first seconds. For the 20 Hz one, there is a transition from chains to a mixture of chains and disks at 15 s, and after 30 s mainly disklike clusters remain in the sample. In the sample with a 30 Hz field frequency, we observe first a mixture of disks and chains, then, after 15 s, mainly disks.

The experiments show that chains first form due to the rotating magnetic field, increase in length then break up and interact with one another along time, resulting in the increase of the proportion of disk-like clusters comparing to chains.

Figure 5.4: QR code leading to a movie that illustrates the aggregation from chains to disk-like clusters at $f_B = 10\,\text{Hz}$.

These observations are consistent with the experiments and simulations led by Abdi *et al.* [79] on a single chain made of 4 particles (see Section 3.3). In those experiments and simulations, they showed that a chain submitted to a magnetic field rotating at a high enough frequency breaks up in two subchains, which also break up at one point, leading to a chaotic motion that results in the formation of a rotating cluster. This behavior is highlighted in the movie of our experiments in [116] (see also Fig. 5.4). Moreover, we observed that the chains not yet aggregated in the sample are rotating at the exact same speed of rotation than the field at any time of the experiment, which is not the case for the disk-like clusters, that are rotating slower. This aligns with the previous observations and simulations presented in Section 3.3.

These first qualitative observations show that the time during which the sample is submitted to the rotating magnetic field will have an impact on the type of clusters, linear, disk-like or both. Therefore, we studied the evolution of the proportion of disk-like clusters with time.

5.2.2 Aggregates discrimination model

To distinguish chains from clusters in the same experiment, we used the **circularity** of the clusters. Circularity is a dimensionless number that is defined as followed

$$c = \frac{4\pi A}{P^2}, \tag{5.1}$$

where A is the area of the object and P is its perimeter. The circularity c is equal to 1 when the object has a perfect circular shape, and lower than 1 when the object is not perfectly circular or when its edges are irregular. In other words, the circularity is a measurement of both the object **shape** and **roughness**.

We measured the circularity of the clusters in the sample along time for a variety of rotational frequencies. The results of this measurements are displayed in the Fig. 5.5. Since c gives us indications not only on the form of the cluster, but also on its roughness, we do not expect to observe circularities of 1, even for the disk-like clusters, because of their irregular shape. Concerning the chains, as a first approximation to establish a quantitative evaluation, we will consider here that particles are perfectly aligned and with only one contact point with each other. Then, the area of a chain is $A = N\pi r^2$, and its perimeter $P = N2\pi r$ (with N the number of particles in the chain and r their radius). Consequently, the circularity of a chain such as described here should scale as $c = 1/L$ (where L is the length of the chain). Knowing this, a long **linear chain** is expected to have a circularity close to **0**, while a **disklike cluster** circularity should be close to **1**. Ribbons, which are chains with a thickness of two or more colloids, are also observed, and their circularity can differ largely with their length and width. Single colloids are not considered neither as a chain nor as a cluster, and they should be excluded from the data. In this respect, we excluded all detected clusters of an area smaller than the area of two colloids (this allows us as well to remove stains and impurities eventually found in the sample).

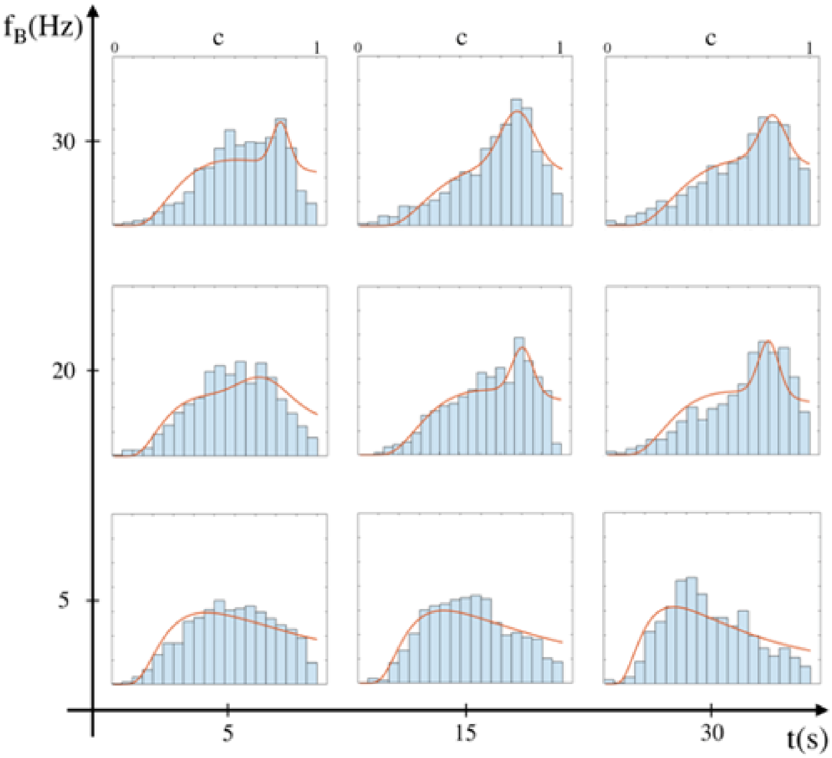

Figure 5.5: Circularity c distributions for $f_B = 5, 20, 30\,\text{Hz}$. With time, clusters are formed and chains disappear for frequencies of 20 Hz and 30 Hz, resulting in a larger proportion of clusters with a circularity close to 1, which is not the case for $f_B = 5\,\text{Hz}$. Histograms are experimental data, while solid curves are fitted from Eq.(5.3).

The distributions displayed in Fig. 5.5 allow us to identify whether the sample contains mainly chains or disk-like clusters. Indeed, for $f_B = 5\,\text{Hz}$, no matter the time of experimentation, the circularity distributions stay approximately the same, with a small peak for small circularities (closer to 0 than 1). On the contrary, for $f_B = 30\,\text{Hz}$, we observe a high number of large circularities (closer to 1 than 0). This conforms to the images of Fig. 5.3, where only chains are observed for $f_B = 5\,\text{Hz}$ at any time and mainly disk-like clusters for $f_B = 30\,\text{Hz}$.

Considering the distributions of the circularity for a magnetic field rotational frequency of $f_B = 20\,\mathrm{Hz}$, we can observe the transition from chains to disks between 15 s and 30 s of experimentation. For $t = 5\,\mathrm{s}$, the distribution in Fig. 5.5 is similar to distributions for a frequency of 5 Hz, indicating that there is mainly **chains** in the sample, as displayed in Fig. 5.3.For $t = 30\,\mathrm{s}$, the distribution in Fig. 5.5 is similar to distributions for $f_B = 30\,\mathrm{Hz}$, leading to the conclusion that there are mainly **disk-like clusters** in the sample, as confirmed in the snapshots of Fig. 5.3. We can therefore consider c as a good indicator of the clusters shape in the sample.

In order to find a relevant parameter to determine the proportion of chains compared to disk-like clusters in the sample at a given time, we present a model for the circularity distribution. To do so, we use a model for the circularity distribution of a sample with only chains and another one for the circularity distribution of a sample with only disk-like clusters, and we merge those two models to describe the circularity distribution of a sample with chains and disk-like clusters.

For a sample containing **chains** only, we used well-known results for the length of chains under a constant magnetic field at thermodynamic equilibrium. In these conditions, the probability density function of the chains length can be approximated by an **exponential** $f_N = \frac{1}{L^*}\frac{e^{-N/L^*}}{e^{-1/L^*}}$, where L^* is the normalized characteristic length of the chains expressed in number of particles, related to the average length $\langle l \rangle$ of the chains by $L^* = \langle l \rangle - 1$, with $\langle l \rangle \in \,]1;\infty[$ [65, 115]. Given f_N, with a continuous approximation for N, one can deduce the probability density function of the chains circularity

$$\begin{aligned} f_c(c) &= f_N(N)\left|\frac{dN}{dc}\right| \\ &= \frac{K}{c^2}\frac{e^{-\frac{K}{c}}}{e^{-K}} \end{aligned}, \tag{5.2}$$

with $K = 1/L^*$ and $c = 1/N$.

For the distribution of **disks** circularity, we use a **normal** distribution, with an average μ that lies between 0.6 and 1, since a disk-like cluster should have a circularity close to 1, but the actual value is lowered by their roughness and eccentricity.

The combination of those two populations leads to the following distribution :

$$f_c(c) = C\frac{K}{c^2}\frac{e^{\frac{-K}{c}}}{e^{-K}} + D\frac{1}{\sigma\sqrt{2\pi}}e^{-\frac{1}{2}\left(\frac{c-\mu}{\sigma}\right)^2}. \tag{5.3}$$

In this equation, the first term describes the behavior of the chains, and has two parameters : the amplitude of the distribution C and its characteristic circularity K. The second one is linked to the disk-like clusters and has 2 parameters : the average μ and the standard deviation σ. Given the normalization of the total distribution, the amplitude D of the second term is linked to the first one by the constraint $C + D = 1$. This model is fitted to the distributions in Fig. 5.5.

Once this model is fitted to our data, we plot the ratio D/C after 120 s of experimentation in Fig.5.6 in order to describe the proportion of disk-like clusters compared to chains. **The higher this ratio, the more disk-like clusters there are in the sample**. After 120s of experimentation, we observe a significant gap between the value of this ratio for $f_B = 5\,\text{Hz}$ and the ones for $f_B = 20\,\text{Hz}$ and $f_B = 30\,\text{Hz}$, suggesting that there is higher proportion of disk-like clusters in the sample for $f_B = 20\,\text{Hz}$ and $f_B = 30\,\text{Hz}$ than for $f_B = 5\,\text{Hz}$. The time evolution of this ratio D/C can be seen in the insert of Fig. 5.6, and shows that there is a transition time to reach the equilibrium with higher proportion of disk-like aggregates. This transition time can be assessed to be approximately 30 s at $f_B = 20\,\text{Hz}$ and 5 s at $f_B = 30\,\text{Hz}$. We can also see that there is a transition value between 10 Hz and 15 Hz for the formation of a high quantity of disks since the ratio D/C is close to 0 at 10 Hz while it saturates after 15 Hz.

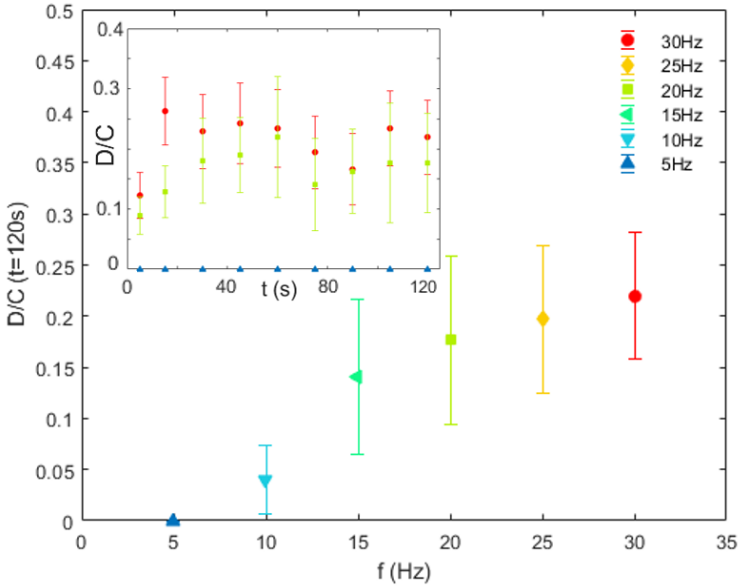

Figure 5.6: D/C ratio for a range of frequencies from 5Hz to 30Hz at an experimentation time of 120s. In the insert, the same ratio is plotted against time for $f_B = 5, 20, 30Hz$.

Another interesting parameter is the parameter K. **The smaller this critical parameter, the longer the characteristic length of the chain clusters**. Hence, a small value of K indicates a solution with a majority of long chains, while a higher value suggests clusters with a less linear form. This parameter K is plotted against the frequency of the magnetic field at 120s of experimentation in Fig.5.7. The evolution of K leads to the same conclusions as the ratio D/C. Indeed, K is significantly larger for $f_B = 20\,\text{Hz}$ and $f = 30\,\text{Hz}$ than for $f_B = 5\,\text{Hz}$ after 120s. This difference subsist for times above 30s. For a time of experimentation of 5s, we clearly see that the K value for $f_B = 5\,\text{Hz}$ and $f_B = 20\,\text{Hz}$ are similar, just as snapshots at this time for these frequencies. All of this confirms that the D/C ratio and the K value from our model allow us to discriminate the type of clusters in the studied solution.

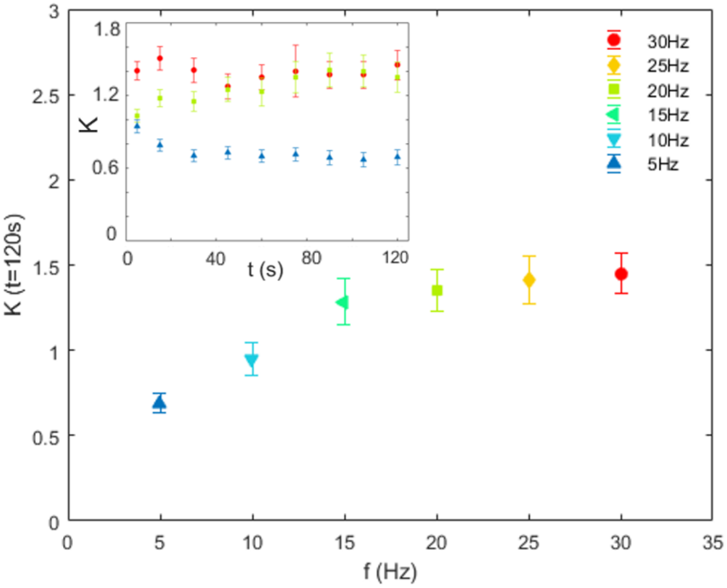

Figure 5.7: Value of the K parameter for a range of frequencies from 5 Hz to 30 Hz at an experimentation time of 120 s. In the insert, K is plotted against time for $f_B = 5, 20, 30\,\mathrm{Hz}$.

Thanks to those parameters, we were able to identify a **critical time** t_c at which the sample can be considered as in the "disk-like clusters" regime. This critical time is plotted against f_B in Fig 5.8. The critical time t_c is obtained by using as a benchmark value the lower D/C ratio for $f_B = 30\,\mathrm{Hz}$ after a minimum of 10s of experimentation. We know from the snapshots in Fig.5.3 that at 5s of experimentation, there is a mixture of chains and disk-like clusters for $f_B = 30\,\mathrm{Hz}$. After 10s of experimentation, we can observe mainly disk-like clusters in the same conditions. Then, for the other magnetic field frequencies, we can consider than any D/C ratio close to the one of $f_B = 30\,\mathrm{Hz}$ indicates that the suspension contains a majority of disk-like clusters. Therefore, t_c is the time at which the D/C ratio of the sample exceeds the chosen benchmark value of $D/C = 0.1655$.

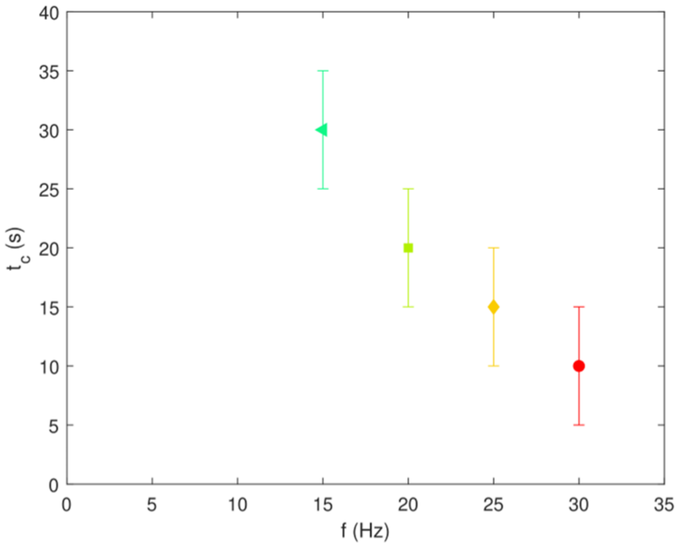

Figure 5.8: The critical time between the ”chains” regime and the ”disks” regime for frequencies ranging from 15 Hz to 30 Hz. Below 5 Hz, there is no transition and the system remains in the ”chains” regime.

5.3 Influence of the suspension volume fraction

In the previous section, we observed and characterized the influence of the **magnetic field frequency** on the aggregates formed consequently to the magnetic and hydrodynamic interactions taking place in the sample. While the magnetic field amplitude was kept constant, its effects were qualitatively assessed (see Section 5.5). This analysis concerns the ”magnetic” side of the system.

Now, we turn our attention to the ”colloidal” side. The key parameter governing this colloidal side is the **volume fraction**. Previous studies, discussed in Section 3.3, have demonstrated its significant impact on aggregation. It appears thus pertinent to test our model with different volume fractions, both lower and higher than the one used in the previous section. However, we will remain within a dilute regime, since highly concentrated colloidal suspension exhibit a totally different behavior. Indeed, in highly concentrated suspensions, a rotating magnetic field induces highly ordered two-dimensional particle clusters, regardless of the rotational frequency [117–119], rather than forming chains or disk-like clusters.

We present here the results of experiments in the exact same condition as previously, with $f = 20\,\mathrm{Hz}$, at values of volume fraction of $\phi = 5.10^{-4}$ and $\phi = 3.10^{-3}$, in addition to the one used before, $\phi = 2.10^{-3}$. Snapshots of the experiments are displayed in Fig. 5.9. We can see from this figure that the aggregation into disk-like clusters is **faster** for a **higher** volume fraction, and almost **nonexistent** for the **lower** volume fraction. This is confirmed when looking at the distributions of the aggregates circularity, which are shown in Fig. 5.10. When fitted to our data, this gives us the two parameters studied previously, K and D/C. The temporal evolution of those parameters are displayed in Fig. 5.11.

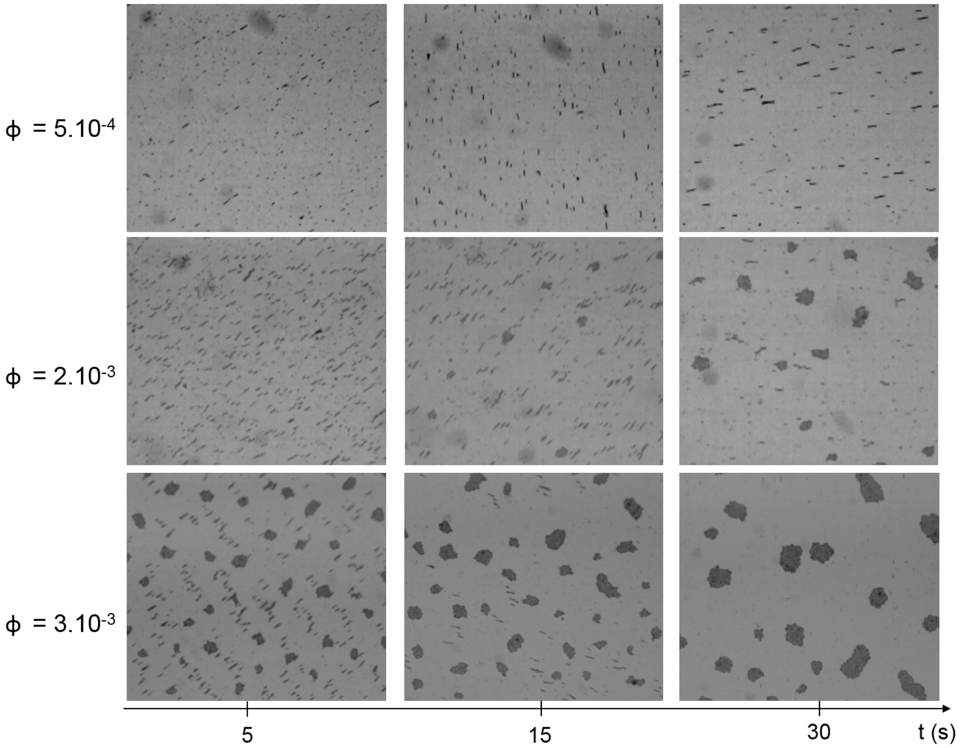

Figure 5.9: Snapshots of 3 samples under a magnetic field with a frequency of rotation of 20 Hz. The activation of the magnetic field corresponds to $t = 0\,\mathrm{s}$. Along time, particles aggregate into chains. At volume fractions of 2.10^{-3} and 3.10^{-3}, the chains then interact and eventually aggregate into disklike clusters. Such disklike aggregates are not observed at $\phi = 5.10^{-4}$.

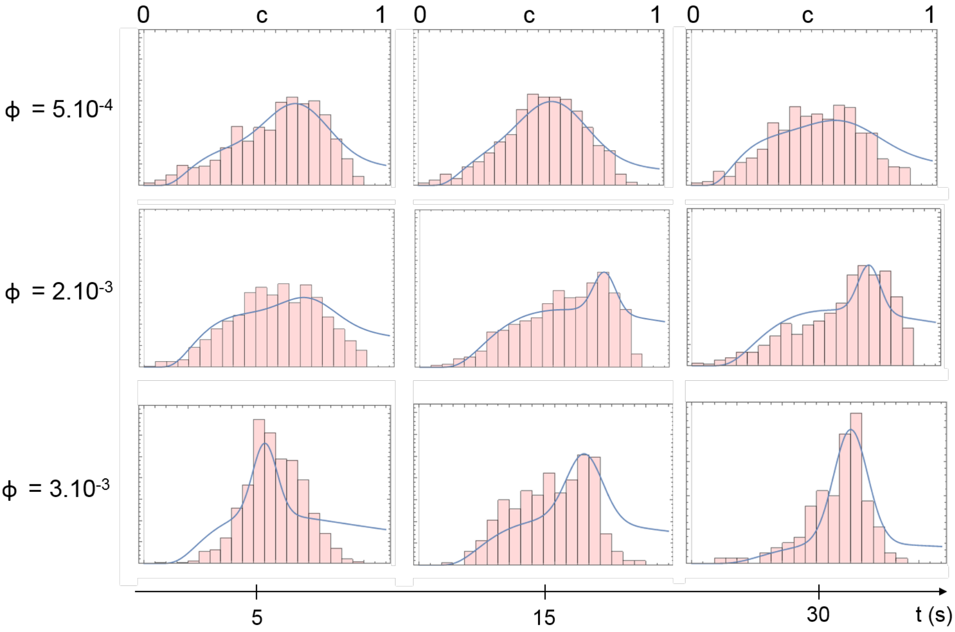

Figure 5.10: Circularity c distributions for $f_B = 20\,\mathrm{Hz}$. With time, clusters are formed and chains disappear for a volume fraction of 2.10^{-3} and 3.10^{-3}, resulting in a larger proportion of clusters with a circularity close to 1, which is not the case for $\phi = 5.10^{-4}$. Histograms are experimental data, while solid curves are fitted from our model.

Looking at the parameter K in Fig. 5.11, we can notice a clear distinction between cases where only chains form (blue and yellow) and those where they aggregate into disk-like clusters (green and red). At a higher volume fraction, the behavior of K over time mirrors that at $\phi = 2.10^{-3}$, but with a **faster saturation**. Indeed, K reaches a constant value after 30 s for $\phi = 3.10^{-3}$, compared to 45 s for $\phi = 2.10^{-3}$. For $\phi = 5.10^{-4}$, K evolves **similarly** to the case where $f_B = 5Hz$ and $\phi = 2.10^{-3}$, which corresponds to the benchmark situation where only chains are formed. This is consistent with the observations from Fig. 5.9.

From Fig. 5.11, we can also observe observe a gap between the D/C value for $\phi = 3.10^{-3}$ and $\phi = 2.10^{-3}$, showing that the proportion of disk-like clusters is **larger** for a **high** volume fraction. This gap being already visible after 5 s of experimentation, the transition between chains to disk-like clusters appears to be much **quicker** in this case. The critical time defined in the previous section is consequently lower than 5 s for this volume fraction. Concerning the results for a **lower** volume fraction, $\phi = 5.10^{-4}$, they indicate that the D/C ratio is **constant** along time, which is consistent with the observations made from the snapshots in Fig. 5.9. Indeed, only chains form in this sample, and it does not change over time. However, the value of this more or less constant ratio would indicate that disk-like clusters have form, while we know from Fig. 5.11 that this is not the case. We make the hypothesis that this could be due to the **thickness** of the chains, compared to the chains observed at higher volume fraction. Since K gives an information about the **length** of the chains, and not its width, it is not surprising that this parameter seems more consistent than D/C in this case.

The thickness of chains formed at lower volume fractions may be attributed to the greater distance between rotating chains, which hinders their interaction and prevents the formation of disk-like clusters. Since the number of particles is not high enough to form disk-like clusters from the chains already aggregated, it forms thick chains instead. When larger aggregates are formed by diffusion-aggregation from smaller particles, thicker chains are indeed expected [27, 63].

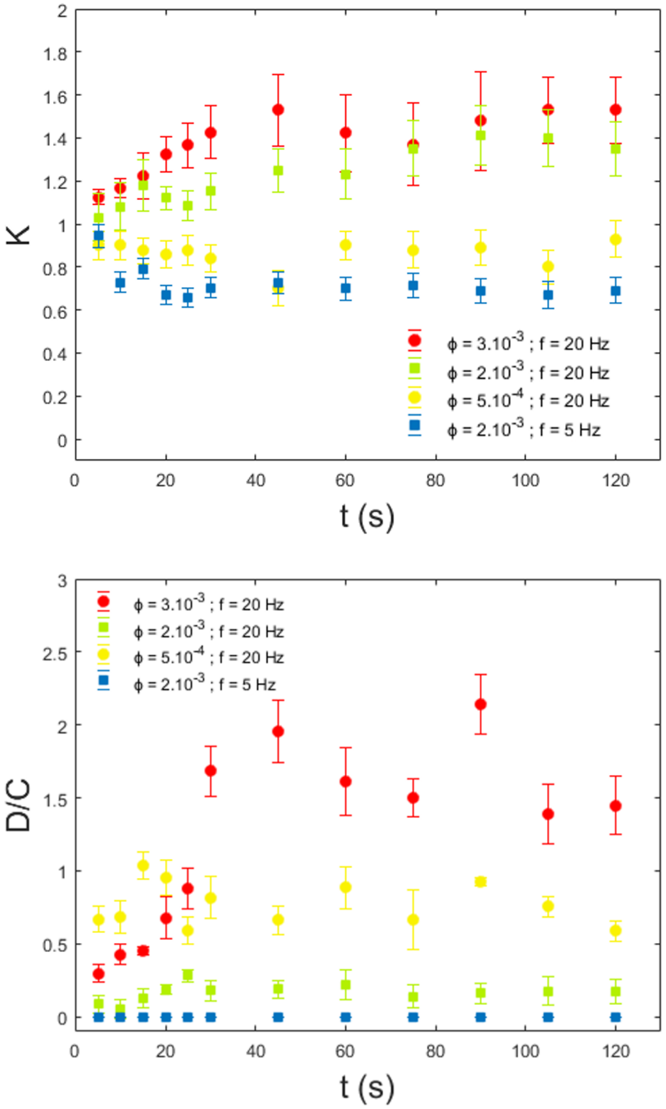

Figure 5.11: Values of K and D/C for $f_B = 20\,\text{Hz}$ plotted against time. The different colors refer to different volume fractions. The blue squares correspond to a frequency of 5 Hz and has been added in order to give a point of comparison to a scenario where only chains are observed.

This thickness can result in a higher circularity, even if the object remains linear. As a reminder, a circularity close to 0 indicates that colloids are perfectly aligned with only one contact point, a condition not met by these chains. Consequently, our method for detecting disk-like clusters may not be suitable for this lower volume fraction.

5.4 Alternative method

To address the limitation of the model, we developed an additional method to differentiate chains from disk-like clusters based on a range of **arbitrary morphological criteria**. This method allowed us to compare the areas of chains and disk-like clusters, and therefore to deduce the chains to disks proportion.

To achieve this discrimination, we used the *Feret diameter* F [120, 121]. Given the variety of aggregate shapes, directly comparing their sizes is challenging. The Feret diameter provides a standardized mean to compare different aggregates by measuring the distance between two parallel lines tangent to the particle and averaging these measurements in all directions. Therefore, F offers a more consistent measurement for **irregularly shaped aggregates** compared to linear dimensions like length or width. In this context, the maximum Feret diameter represents the length, while the minimum Feret diameter corresponds to the width. The ratio of F_{max} to F_{min} is then comparable to the aspect ratio, AR. For a **chain**, which is typically long and thin, F_{max} is large relative to F_{min}, which cannot be smaller than the diameter of a particle, resulting in a **high aspect ratio**. On the opposite, a **disk-like cluster**, being roughly equal in length and width (but larger than a single particle), will exhibit a large F_{min} and an aspect ratio **close to 1**. In between lies the case of a **thick chain**, for which F_{min} can be larger and AR **approaches one**.

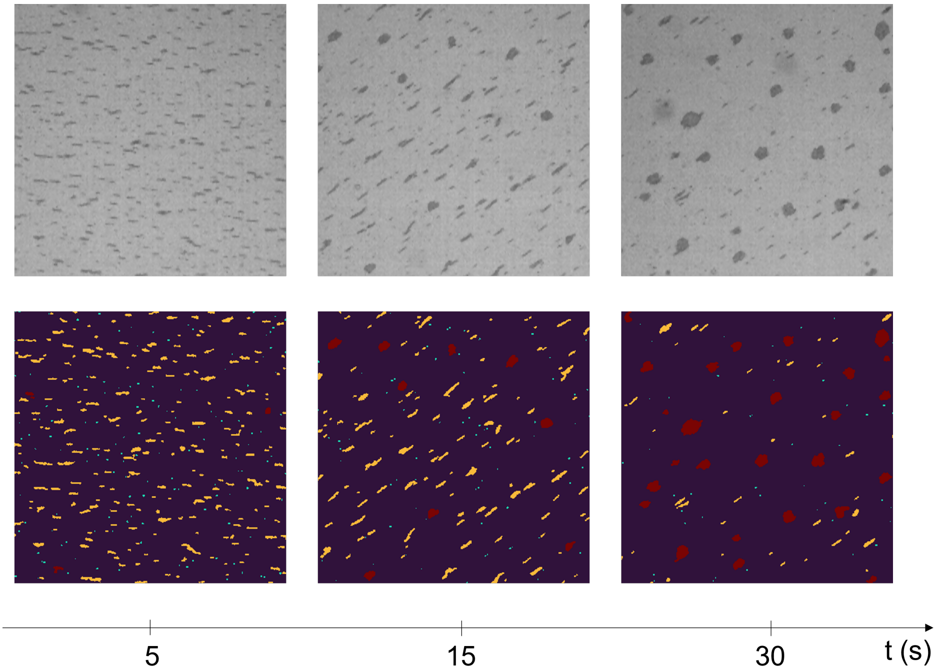

Figure 5.12: Results of the morphological analysis compared to the original images for a magnetic field frequency $f_B = 20\,\text{Hz}$ and a volume fraction $\phi = 2.10^{-3}$. The aggregates identified as chains are colored in yellow while the ones classified as disks are indicated in red. The unidentified aggregates and the background are respectively displayed in blue and purple.

Following those requirements, we first classified objects as disks if their minimal Feret diameter exceeded an arbitrary threshold of 3.22 µm, and their aspect ratio was smaller than 2. If their minimal Feret diameter was greater than 8.26 µm, the objects were also classified as disks if their aspect ratio reached up to 2.5. Otherwise, objects were considered as chains if their maximal Feret diameter was greater than 1.84 µm, and their minimal Feret diameter smaller than 8.26 µm. Remaining objects, which were mostly single colloids, dimers or stains, were considered as unidentified. An example of the resulting images are displayed in Fig. 5.12.

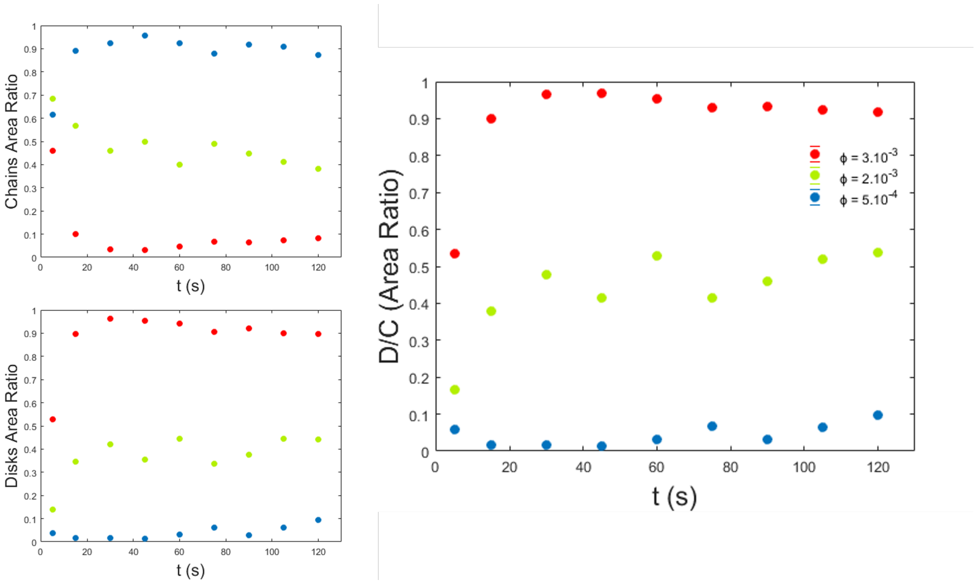

Figure 5.13: Morphological analysis of chains and disks area ratio in regards to the total aggregates area for a range of frequencies and a volume fraction $\phi = 2.10^{-3}$. The figures on the left display this ratio for chains and disks, while the figure on the right shows the proportion of disks compared to the proportion of chains.

Once the aggregates are sorted out, we measure their total area and compare it to the area of the detected disks and chains. This gives us an area ratio that we can use to track the quantity of disks and chains over time in the sample. Dividing the disks and chains area results to a ratio that should be similar to the parameter D/C of our model. These different ratios are displayed on the right in Fig. 5.13 for a range of volume fractions with a frequency $f_B = 20\,\text{Hz}$. Comparing those results to the snapshots in Fig. 5.9, we can confirm that this method is **efficient** when thicker chains are formed, but it is based on **arbitrarily** fixed criteria, while the model we developed is based on **theoretical** considerations and does not depend on arbitrary decisions.

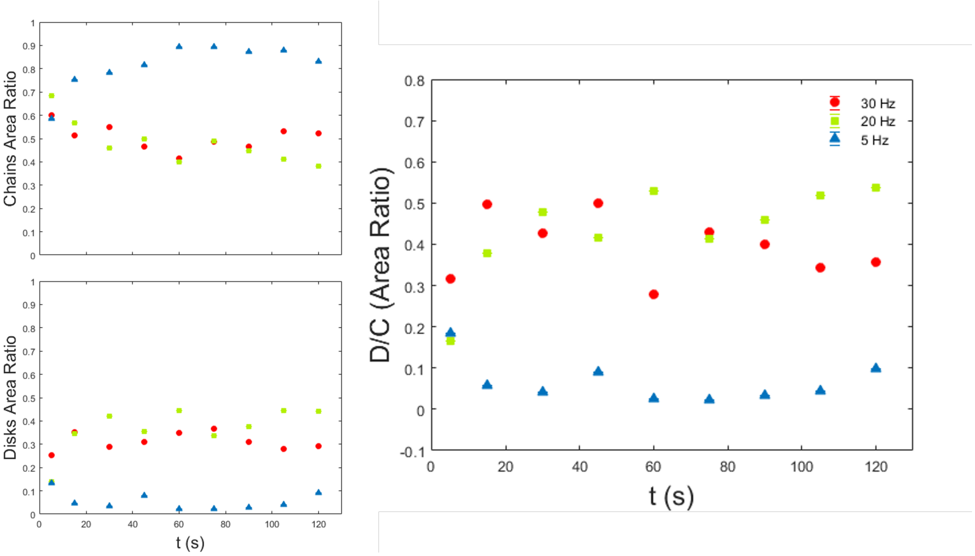

Figure 5.14: Morphological analysis of chains and disks area ratio in regards to the total aggregates area for a range of frequencies and a volume fraction $\phi = 2.10^{-3}$. The figures on the left display this ratio for chains and disks, while the figure on the right shows the proportion of disks compared to the proportion of chains.

Finally, we compared this method to the results from our model when $\phi = 2.10^{-3}$ for three different magnetic field **frequencies**. From Fig.5.14, we can see that the disks to chains proportion has the **same** evolution with time that the parameter D/C obtained from our model. Indeed, for $f_B = 5\,\mathrm{Hz}$, the area ratio remains very low at all times. This corresponds to the benchmark scenario where only chains are formed. On the contrary, for $f_B = 20\,\mathrm{Hz}$ and $f_B = 30\,\mathrm{Hz}$, the area ratio increases in the 30 first seconds of experimentation then remains constant, indicating that the chains first formed are interacting and aggregating into disk-like clusters. These results clearly **confirm the outcomes of our model**, thereby validating its relevance.

5.5 Conclusions and perspectives

In this chapter, we specifically tackled the topic of the **early stages** of colloid clustering in a **quasi-2D** suspension subsequent to the application of a **rotating magnetic field** in the plane of the suspension. For this purpose, we experimentally investigated the dynamics of disk-like clusters formation. Rather than clustering directly into disk-like structures, we observed that colloids initially aggregate into chains, even at frequencies where chains are not expected. These chains then interact and eventually form the anticipated disk-like clusters. This finding adds a new step to the visual overview presented previously in Fig. 3.10, which is updated in Fig. 5.15.

We focused on the time dependency of this phenomenon and observed both chains and disk-like clusters at the same time in the sample. In order to measure the aggregation process duration, and to characterize the proportion of chains and disk-like structures in the suspension, we used the circularity. Indeed, chains and disks should have a very distinct circularity, allowing us to differentiate the type of clusters detected. Once the distribution of circularities obtained for the sample, we proposed a model to fit to the data. From this model, we obtained two key parameters : the proportion of disk-like clusters to elongated aggregates, D/C, and K, the inverse of the chains normalized characteristic length. Looking at the temporal evolution of D/C and K, we studied the influence of two experimental parameters, the rotational frequency of the magnetic field, f_B, and the volume fraction ϕ. Concerning the frequency, we were able to identify a critical time t_c at which the clusters in the suspension are largely predominant. Investigating the influence of the volume fraction, we noticed that our model was not fit to measure efficiently the number of disks and chains in a sample when the chains were thick. Consequently, we developed an additional method to discriminate chains and disk-like clusters. This method revealed itself to be efficient in all situations, but is based on arbitrarily fixed criteria, while the model we developed is based on theoretical considerations. The results show that at the same frequency, a lower volume fraction foster chain formation, while its the opposite for larger volume fraction.

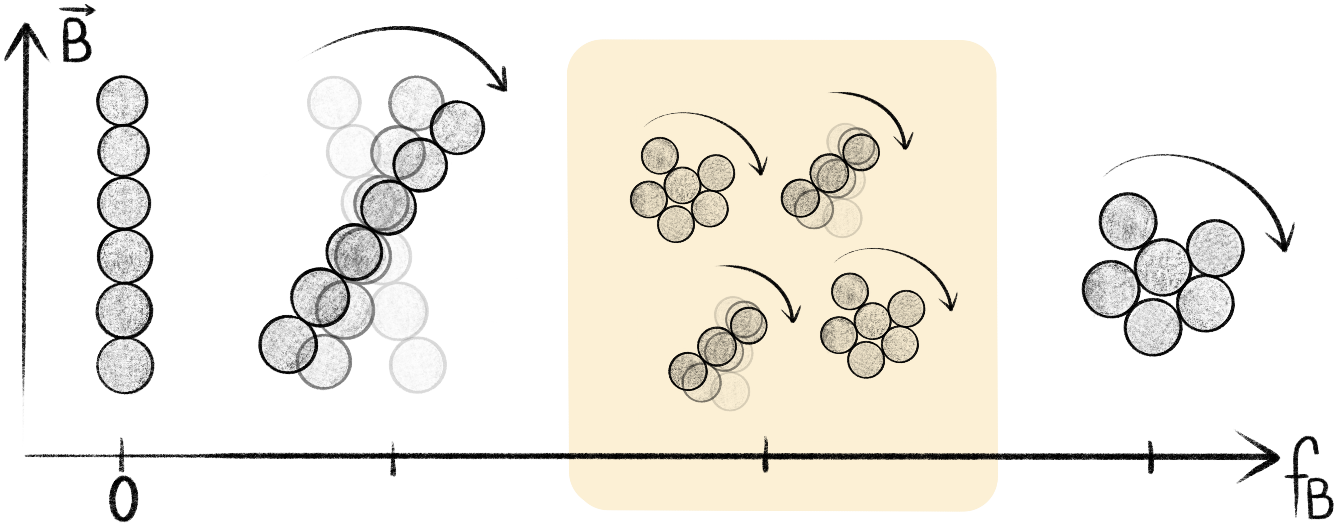

Figure 5.15: Updated schematic drawing of the various structures formed when a rotating magnetic field is applied to superparamagnetic colloids. Our personal contribution is highlighted in yellow and consists of the observation and characterization of a mixture of chains and disk-like clusters during some time for intermediate frequencies.

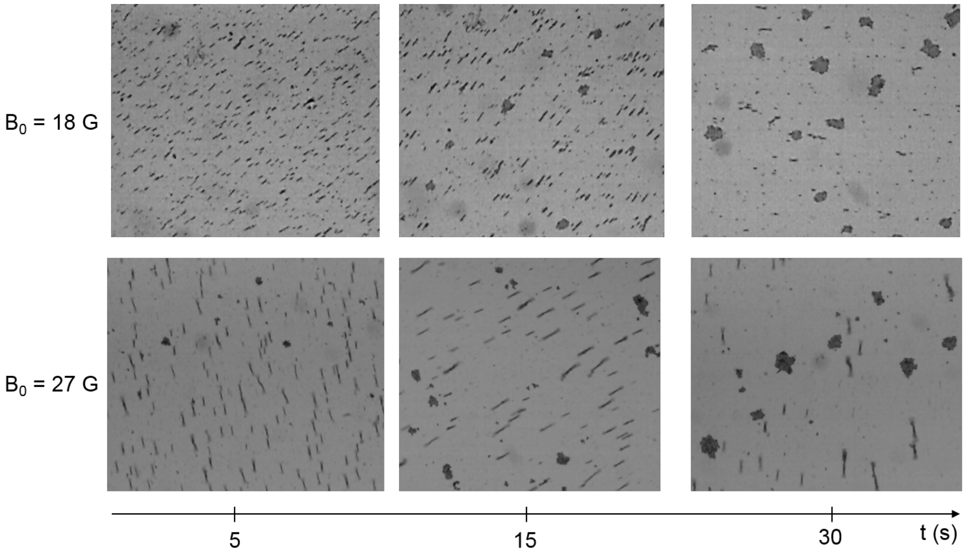

Figure 5.16: Snapshots of two samples under a magnetic field with a frequency of rotation of 20 Hz and a volume fraction $\phi = 2.10^{-3}$. The activation of the magnetic field corresponds to $t = 0\,\mathrm{s}$. Along time, particles aggregate into chains, then interact and eventually aggregate into disklike clusters. For a magnetic field of a higher intensity, the chains first formed are thicker and the aggregation into disklike clusters seems to be delayed.

Thanks to the parameters mentioned above, we are able to characterize the transition state from chains to disk. However, a number of questions remains open in order to fully comprehend this process. As an example, another parameter has potentially an influence on the transition : the **magnetic field amplitude**. We performed some experiments with a higher magnetic field intensity, and as a result the formation of the disk-like clusters seems to be delayed, while the chains are thicker, as pictured in Fig. 5.16. To perform those experiments, we chose a field with an intensity of 27 G, to compare to the 18 G intensity used through our previous experiments.

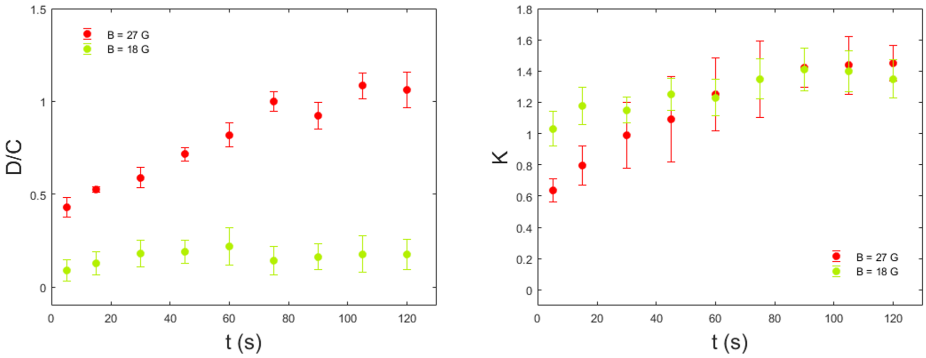

Figure 5.17: On the left, the parameter D/C, and on the right, the parameter K, both deduced from our model for a magnetic field frequency of 20 Hz and a volume fraction $\phi = 2.10^{-3}$. Both parameters are displayed along time. Those parameters have been plotted for two different magnetic field intensities.

We applied the model developed in the previous section to analyze those images, and the results are shown in Fig. 5.17. From the results for the parameter K, we can confirm that the aggregation into disk-like clusters seems to be delayed. For both magnetic field intensities, K increases with time to reach a similar constant value, which indicates that the aggregates have the same length at the end of the clustering process. Concerning the other parameter, D/C, we observe that it always have a larger value for $B = 27$ G. This can be linked to the fact that, as it was the case for a lower volume fraction, the chains formed are thicker and thus can be wrongly identified as disk-like clusters when looking at their circularity. To go beyond this limitation, we used the morphological analysis developed in the precedent section. The corresponding area ratios are shown in Fig. 5.18.

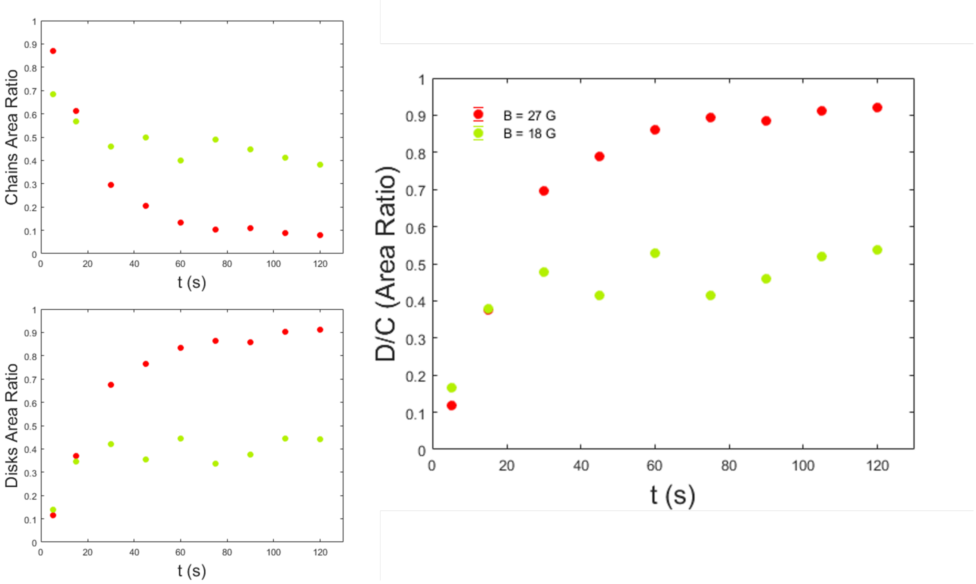

Figure 5.18: Morphological analysis of chains and disks area ratio in regards to the total aggregates area for two different magnetic field intensities, a magnetic field frequency of 20 Hz and a volume fraction $\phi = 2.10^{-3}$. The figures on the left display this ratio for chains and disks, while the figure on the right shows the proportion of disks compared to the proportion of chains.

From Fig. 5.18, we can observe that the area ratios between disk-like clusters and chains is not always larger for $B = 27\,\mathrm{G}$. Indeed, we rather observe that this ratio is quite similar in the 15 first seconds, and then becomes larger for $B = 27\,\mathrm{G}$ after 30 s. This indicates that the aggregation from chains to disk-like clusters is **more important** for a larger magnetic field. Moreover, the D/C ratio reaches its saturation value later for the larger magnetic field amplitude, which confirms a **longer aggregation process**. Further experiments with a wider range of intensities are required in order to clarify the influence of the field strength on the aggregation process itself.

The interest of studying the elementary case presented in this chapter is notably to allow a better understanding of more complex systems. Indeed, by grasping the fundamental principles at play in simpler configurations, we can better predict and analyze the behavior of more intricate scenarios, such as the **coupling** of the magnetic field with other fields, or colloids with an **anisotropic** shape for instance.

The coupling of the magnetic field with other ones can be achieved for example with an **electric** field, in which case it is possible to control the particles through the dielectric permeability contrast between the colloids and their suspending liquid [122, 123]. Magnetic and **acoustic** fields can also be combined, resulting in ordered crystals [124] or 3D assemblies [59]. Another possible coupling is the coupling of a magnetic field with a **hydrodynamic** one. In this case, structures like translating microrollers [125], colloidal swarms [126], or colloidal vortices [127, 128] appear and exhibit organized patterns and synchronized motion. On the other hand, recent developments in the synthesis of **anisotropic** colloids such as ellipsoids [129, 130], dumbbells [131], or peanut-shaped particles [132], led to the emerging of new structures and applications.

Rather than exploring additional parameters, such as varying the magnetic field amplitude or using different particles, we chose to focus on our existing system and investigate its behavior in **three dimensions**. The key questions are whether the same structures observed in the quasi-2D configuration will manifest in 3D, and how this aggregation will affect sedimentation. By comparing our experimental observations with the scenarios presented in Chapter 4, we aim to identify the microscopic structures resulting from aggregation and evaluate how they align with the findings discussed in this chapter.

6

Settling the Scene

Linking microscopic assemblies to macroscopic effects

When confined in two dimensions and subjected to a rotating magnetic field, superparamagnetic colloids are known to aggregate into well-defined structure depending on the field rotational frequency f_B. Below a critical frequency, rotating chains are observed, while above this frequency, disk-like clusters rather form due to the interparticle potential becoming isotropic. However, we showed in our experiments that chains also form above this rotational frequency at the beginning of the aggregation process, coexisting at some point with disk-like clusters. Those chains interact with one another and end by aggregating into the expected isotropic clusters. This process gets quicker and quicker when f_B increases. Jumping into a three dimensional system, will those same structures appear ? And if so, what will be the consequences on the sedimentation process ?

6.1 Experimental Method

In order to compare effectively our results to those presented in Chapter 5, our experimental set-ups in both cases should be as close as possible. The one used in this chapter is presented below, and compared to the previous set-up detailed in Section 5.1.

To produce the **magnetic field**, we used the same equipment as in the previous experiments, with the exception of the two pairs of coils, which are larger but allow for the same magnetic field amplitude. As a reminder, those coils are placed in the Helmholtz configuration in order to produce an homogeneous time-varying magnetic field between them, with the use of a sinusoidal alternating current. As previously, we measured the magnetic field at the center of the two pairs of coils with a Hall probe to test its homogeneity, with 1 mm steps. Those measurement show that the magnetic field has a variation smaller than 6% over 1 cm at the center of the coils, in the two directions.

The **colloids** as well as their preparation also remain exactly the same as presented in Section 5.1.2. We focused on the same volume fraction, $\phi = 2.10^{-3}$, and used a volume of $200\,\mu$L for the experiments. The suspension was placed into a clear rectangular container measuring 1 cm to 0.5 cm.

The main difference with the previous experiments lies in the **observation of the suspension**. Indeed, using a ”large” volume of colloids with such a volume fraction makes it difficult to examine the suspension at the microscopic level. Thus, instead of a microscope, we chose a simple Thorlabs digital camera to record the sedimentation of our samples with time.

The whole set-up is represented in Fig. 6.1. For the sake of clarity, we will refer to the pair of coils parallel to the axis between the light source and the camera as *longitudinal*, noted L in the figure, and to the other pair as *transversal*, T in the figure. On the left of the longitudinal coils, we placed a diffuse backlight LED from Thorlabs (reference : LEDBW1), and on the right, the camera. The coils are hollow at their center and

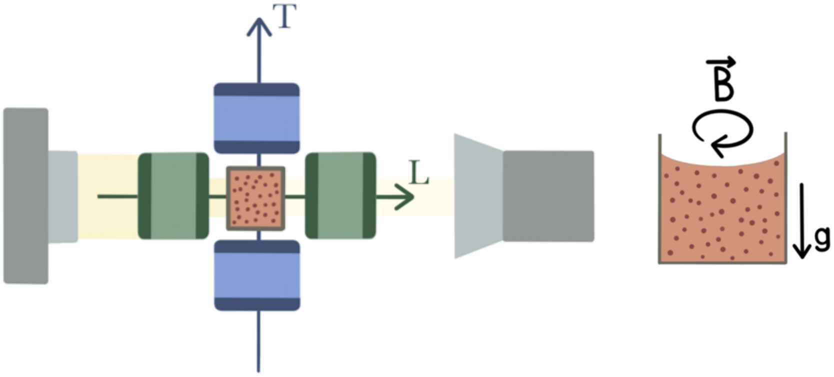

Figure 6.1: Diagram of the experimental setup, with a top view on the left and a front view on the right. The axis labeled T represents the *transversal* direction, while the label L corresponds to the *longitudinal* direction. The transversal pair of coils is shown in blue, and the longitudinal pair in green. The light path through the sample to the camera is illustrated in light yellow. The rotating magnetic field, denoted by $\vec{B}$, is depicted on the right, with its orientation varying over time in the plane defined by the T and L axes.

allow the light to go from the light source to the camera through the sample. The light path is schematized in light yellow in Fig. 6.1. The resulting images are processed with ImageJ and Matlab to extract the transmitted light intensity in respect with time, $I(t)$.

6.2 Influence of the magnetic field frequency

In Section 4.4, we described two potential sedimentation processes. The first is cluster deposition, which occurs when isolated aggregates form, resulting in a diffuse sedimentation interface. The second is collective settling, where a gel forms within the sample, leading to a sharp sedimentation interface.

A simple observation of the interface should allow us to determine which of these two mechanisms is at play in our experiments. To this end, we conducted experiments across a range of rotational frequencies,

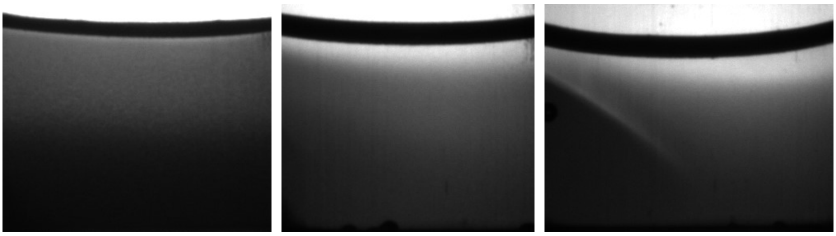

Figure 6.2: Snapshots of the experiments at different times with a magnetic field rotational frequency respectively of 1 Hz, 8 Hz and 10 Hz. In the three snapshots, we notice the diffuse sedimentation profile.

from $f_B = 0.01\,\mathrm{Hz}$ to $f_B = 30\,\mathrm{Hz}$, and monitored the sedimentation during several hours. Some snapshots of those experiments are presented in Fig. 6.2. It is clear from these snapshots, and for all the other frequencies tested, that the interface is **diffuse**, which indicates that **individual aggregates** are formed. In the following, we first attempt to determine the structure of these aggregates and compare them to the ones observed in two dimensions. Then, we investigate the influence of this aggregation on the sedimentation mechanisms.

6.2.1 Aggregates structure

Because the sedimentation interface is diffuse in all of our experiments, we can conclude that individual aggregates form rather than gel-like structures such as the connected layers described in Section 4.2. Based on our two-dimensional results, we expect three distinct scenarios, each corresponding to different types of aggregates depending on the field's rotational frequency. As a reminder, these three 2D scenarios are illustrated in the 'after' section of the annexed card.

Firstly, for **low frequencies** such as $f_B < 5\,\mathrm{Hz}$, we expect **rotating chains**. In this case, the chains can be assimilated to rotating rods, and the resulting transmitted light should vary periodically, as presented in Section 4.3. The period of this light variation corresponds to the chains rotation period and should be half of the magnetic field's.

Secondly, **intermediate frequencies** ranging as $5 < f_B < 10\,\mathrm{Hz}$ falls within the **transition** spectrum. In two dimensions, this corresponds to the point where chains can no longer follow the rotational speed of the magnetic field, inducing the transition to disk-like clusters. The resulting transmitted light period should then be smaller than the magnetic field period.

Lastly, **high frequencies** larger than 10 Hz should induce **isotropic clusters** or even **layers** if sufficient. However, for the latter configuration, the fact that the interface is diffuse, not sharp, seems to indicate that there is no layering with our particles, which is consistent with the approximate minimum frequency required to effectively observe such a structure ($f_B = 500\,\mathrm{Hz}$, see Section 4.2). If the structures that form are isotropic, no periodic variation in transmitted light should be recorded. If such periodic variations are observed nevertheless, it would potentially indicate the presence of chains along with the isotropic clusters, as it was the case for the 2D system.

For the sake of clarity, we will refer to these three scenario as follows: S_1 for $f_B \leq 5\,\mathrm{Hz}$, S_2 for $5\,\mathrm{Hz} < f_B < 10\,\mathrm{Hz}$, and S_3 for $f_B \geq 10\,\mathrm{Hz}$. Those scenarios are depicted in Fig. 6.4

Given these considerations, transmitted light proves to be an effective method for monitoring the formation of microscopic structures in the sample through macroscopic observation. Our experimental investigation thus begins by tracking variations in transmitted light and comparing their frequency to that of the magnetic field. If no variation is observed, the aggregates are isotropic. In contrast, a variation with a frequency double that of the magnetic field indicates anisotropic structures, such as chains or ribbons, rotating in synchronization with the field. Each time these chains align with the light path, twice per magnetic field cycle, the transmitted light reaches its maximum. If the variation frequency is lower, it suggests the chains are no longer following the field's rotation.

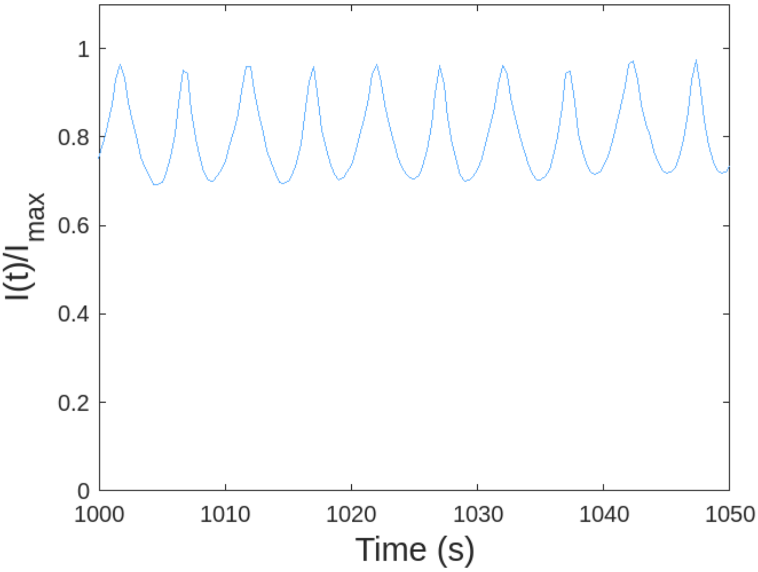

Figure 6.3: Time evolution of $I(t)/I_{max}$ at $f_B = 0.1\,\mathrm{Hz}$, highlighting the periodic variations.

To measure the transmitted light across time, we recorded images with a frame rate high enough to capture the light variations. We measured the mean gray level of each image, which is directly proportional to the transmitted light and thus has the same period if varying. Typical results for $f_B = 0.1\,\mathrm{Hz}$ are depicted in Fig. 6.3. From these results, we can see that the transmitted light **periodically varies with time** at this frequency. This periodic variation is also observed for the other frequencies in S_1 and S_2. Along with those measurements, an original film for $f_B = 1\,\mathrm{Hz}$ is accessible through the QR code in Fig. 6.5 (see also [133]), showcasing the bright light flashes that are observed in these frequency ranges.

From these images, we measured the period of each signal and plotted it regarding the frequency in Fig. 6.4. In this figure, we can see that the light flash frequency is the **double** of the magnetic field frequency for $f_B < 5\,\mathrm{Hz}$. The critical frequency where the light flashes no longer follow the magnetic field frequency is within the $5\,\mathrm{Hz}$ to $10\,\mathrm{Hz}$ range,

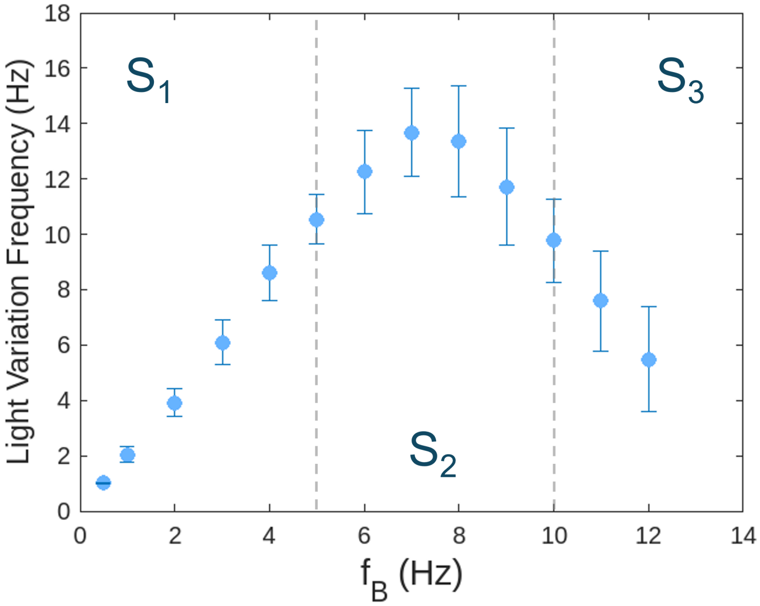

Figure 6.4: Frequency of the transmitted light variation regarding the magnetic field frequency. Below the transition phase S_2, the transmitted light period is twice the magnetic field's, indicating that chains form in the sample and follow the magnetic field rotation at the same speed. For frequencies in the S_2 range, the transmitted light still varies periodically, but slower. This is due to the fact that the chains can no longer follow the magnetic field rotation. For frequencies in S_3, the transmitted light still varies with time, but the amplitude of these variations becomes very small. The error bars correspond to the standard deviation of the time between two light flashes.

which corresponds to the **transition range** in two dimensions. Those observations are consistent with the hypothesis that the same structure are forming in 3D and in 2D, as explained in the preceding paragraph. The light variation measures indicate that the chains formed below 5 Hz follow exactly the magnetic field rotation, while they start to go slower between $f_B = 5\,\mathrm{Hz}$ and $f_B = 10\,\mathrm{Hz}$, which is exactly what was observed in 2D. It is interesting to note that light variations are also observed above $f_B = 10\,\mathrm{Hz}$, and even at $f_B = 30\,\mathrm{Hz}$.

Figure 6.5: QR codes leading to movies of the experiments. On the left, we highlight the light flashes due to the chains rotation at $f_B = 1\,\mathrm{Hz}$. On the right, we showcase the settling of the large aggregates, corresponding to the first phase of sedimentation at $f_B = 10\,\mathrm{Hz}$

However, the transmitted light variations become more and more erratic as the frequency increases, as well as hardly visible. This indicates that chains still form for these frequencies, but **mixed with other aggregates**. Indeed, if the colloids aggregate in a mixture of chains and disk-like clusters in the early-stages of the experimentation as in 2D, the isotropic clusters can mask the rotation of the chains, blocking the light even if the chains are oriented longitudinally. Moreover, if the chains are small, the light variation they induce should also be small. Note that a similar scenario could also occur in a mixture made of short chains and single colloids. Nevertheless, this could also indicate that no chain form, but rather large and short ribbons, that would not induce a large variation of transmitted light when rotating, since their width would be close to their length.

With these results, we can conclude that the first two scenarios observed in 2D, S_1 and S_2, correspond also **to the structures that form in three dimensions**. Regarding S_3, it appears that some of the colloids aggregate into chains or large ribbons, but this is likely not the case for a majority of them. Whether the remaining particles aggregate into isotropic clusters or do not aggregate at all cannot be determined at this point.

Next, to assess the impact of these different structures and their dynamics on the sedimentation mechanism, we performed the same experiments over a **complete sedimentation time**.

6.2.2 Sedimentation

To assess the impact of the aggregation on the sedimentation process, we observed the transmitted light through the sample over an extended period. We used two different methods to characterize this transmitted light. The first method, as described in the previous section, involves calculating the **mean gray value** of each image, which is directly proportional to $I(t)$. The second one consists of **local luminosity profiles** from the top to the bottom of the sample, at successive times. In both cases, the measures are normalized by the maximum light intensity reached, I_{max}. In the following, we will first consider the results for a magnetic field free sedimentation. This will then allow us to compare this baseline case to each of the three scenarios mentioned before.

We measured $I(t)/I_{max}$ every 5 minutes for a sample with no external magnetic field applied, as shown in Fig. 6.6. Initially, **no light** passes through the sample, as the particles are homogeneously suspended. As the particles start to settle, the transmitted light steadily increases, until it reaches a **saturation value** when all of the particles rest at the bottom. As it is the case with a rotating magnetic field in our frequency ranges, the sedimentation interface is diffuse, indicating that the mechanism behind the sedimentation is the cluster deposition. Since the suspension is originally designed to be stable against settling (see Section 2.3.3), the sedimentation takes a long time to complete, around **20 hours** in this case. If the application of a magnetic field induces a different sedimentation mechanism, it should affect this sedimentation time. We first tested this hypothesis for f_B ranging in S_1, then considered the scenario S_3 as well as the transition between the two, S_2.

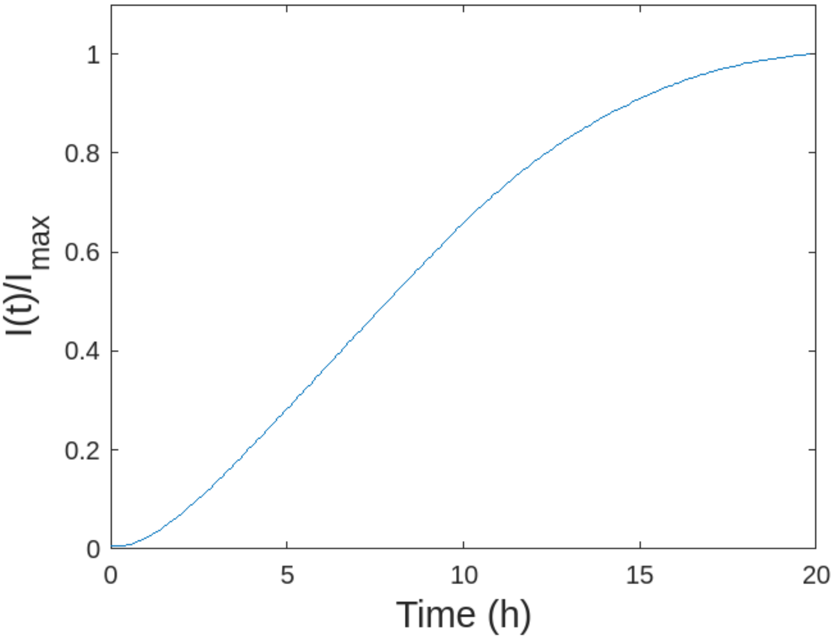

Figure 6.6: Time evolution of $I(t)/I_{max}$ when no magnetic field is applied. The transmitted light increases steadily as particles settle, eventually clearing the sample. The process takes approximately 20 hours.

SCENARIO 1

Let's consider the results for S_1, where we showed that the colloids aggregate into chains that follow the magnetic field rotation. In Fig. 6.7, the normalized transmitted light, $I(t)/I_{max}$, is represented during a complete sedimentation for $f_B = 0.01\,\text{Hz}$.

The first conclusion to emerge is that the sedimentation is indeed **largely faster** when such a magnetic field is applied, compared to the case with no magnetic field. The process takes about **1 or 2 hours** with the slowly rotating magnetic field, and 20 hours with no magnetic field. Besides this obvious difference, the transmitted light also steadily increases in this case, until it reaches a saturation value.

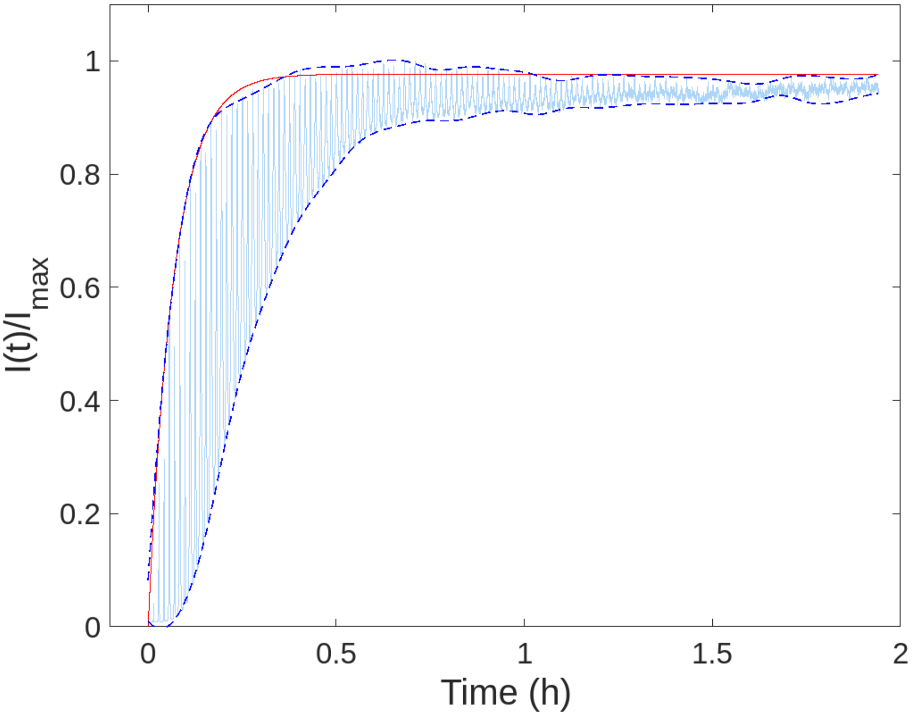

Figure 6.7: Time evolution of $I(t)/I_{max}$ at $f_B = 0.01\,\text{Hz}$, plotted in light blue and showing both the periodic light variations and a complete sedimentation process. In dark blue, the upper and lower envelopes of the signal, that exclude the periodic variations. In red, the fitted exponential for the upper envelope, that allow us to obtain a characteristic sedimentation time.

The periodic light variations are clearly visible, as in the previous measurements. Since our focus in this section is on the sedimentation process as a whole, we plotted the two signal envelopes, namely the two smooth curves outlining the peaks due to the chains rotation. The upper envelope corresponds to the case where the chains are oriented parallel to the longitudinal coils, and the lower to the perpendicular direction. Both envelopes (dotted blue lines), along with the original signal (light blue), are shown in Fig 6.7. From those results, we can monitor at once aggregation and sedimentation.

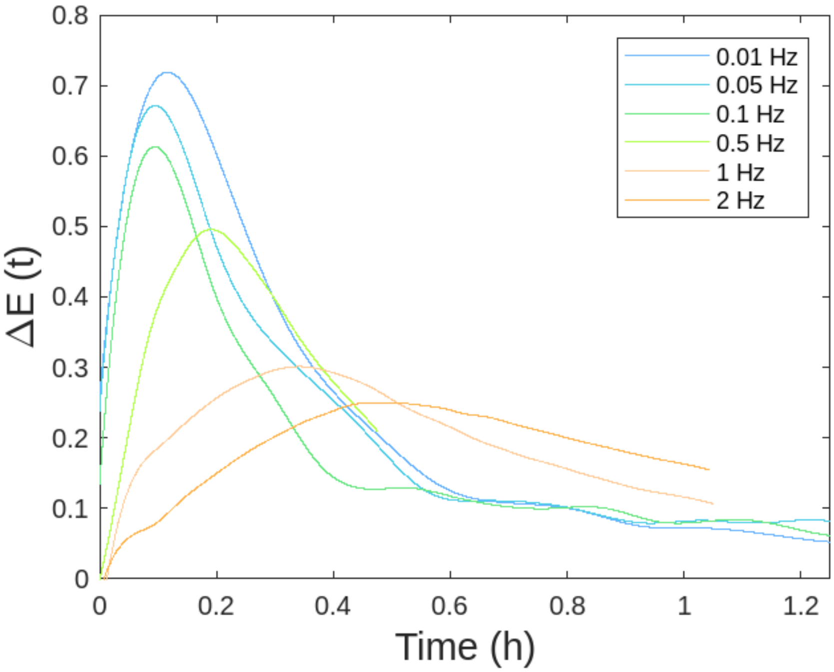

Figure 6.8: Difference in transmitted light regarding time between the parallel configuration (chains along the L axis) and the perpendicular configuration (chains along the T axis) for all S_1 frequencies. These results highlight the contrast between those two situations.

The two configurations where chains are parallel or perpendicular to the longitudinal coils are highly contrasted. To quantify this contrast, we measured the difference between the two envelopes, ΔE, and plotted it over time for a range of frequencies, as shown in Fig. 6.8. When this difference increases, it indicates that more and more particles are aggregated into the rotating chains, enhancing the contrast between the two configurations. Our results show that this aggregation into chains occurs **faster** for **lower frequencies**. When the difference decreases, it reflects the fact that fewer chains remains in the sample, since they have settled, resulting in a lower contrast. From our measures, we can deduce that the settling of the rotating chains is also **faster** for **lower frequencies**.

Additionally, the contrast amplitude decreases with the frequency as well, which can be explained by the length of the chains being smaller for higher frequencies. Considering the perpendicular configuration, this makes no difference. On the opposite, for the parallel configuration, one long chain containing many colloids is letting light pass through more than many short chains containing few particles, leading to a higher contrast between the two situations. These observations confirm that aggregation plays a significant role in the mechanism that takes place.

To go further in the characterization of the parallel situation compared to the perpendicular, we plotted the normalized transmitted light $I(t)/I_{max}$ in regards to the the height in the sample. To do so, we considered horizontal lines of 1 pixel from the top to the bottom of the sample, and measured the mean gray level along each line, excluding the meniscus. Doing so for each frame, we were able to plot the transmitted light profiles according to the vertical position in the sample. We differentiated the frames corresponding to the upper envelope, thus to the parallel case, and those corresponding to the lower envelope, thus to the perpendicular case. Both plots are depicted in Fig. 6.9 for $f_B = 0.01\,\mathrm{Hz}$ and reveal two drastically different behaviors.

The results for the case where the chains are oriented **along the longitudinal axis**, in green, show that the profiles are horizontal. This indicates that $I(t)/I_{max}$ increases uniformly along the sample height, whereas we would expect sedimentation to create a transmitted light gradient, given the diffuse sedimentation front. This behavior suggests that the initial aggregation of single colloids into chains has a more significant impact on transmitted light compared to sedimentation in the early times of the process. This can be understood as follows, from the start of the aggregation to the end of the sedimentation.

Initially, as particles are homogeneously suspended, their progressive aggregation into chains influences light transmission uniformly across the sample height. When colloids aggregate into chains, their combined projected area is reduced to that of a single colloid, leading to less ob-

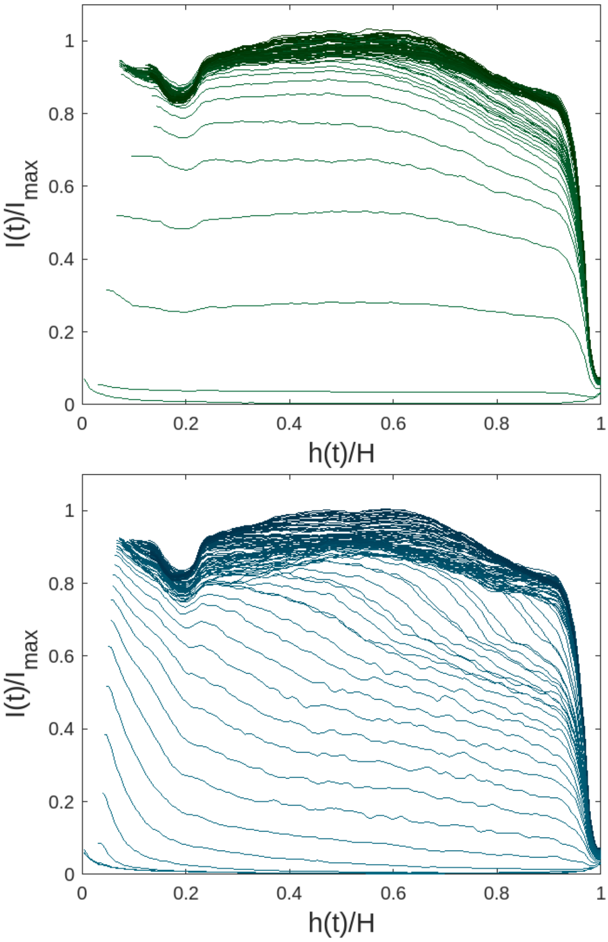

Figure 6.9: Normalized transmitted light profiles according to the vertical position in the sample, from top to bottom, for $f_B = 0.01\,\mathrm{Hz}$. On the left, the analyzed frames correspond to the upper envelope of the signal, or the case where the chains are parallel to the longitudinal axis. On the right, the graph corresponds to the lower envelope, or the case where the chains are perpendicular to this axis. The vertical position is divided by the total height of the sample. The color of the curves goes darker with time. One profile is plotted every 50 seconds.

struction compared to isolated particles. This is illustrated in the first step of the top part of Fig. 6.10. Once the chains are large enough to settle, further aggregation of multiple chains into one, as well as the capture of remaining colloids, has the same effect on $I(t)$ as chain sedimentation. This is represented as the second step of the top representation in Fig. 6.10. In this stage, a chain occupies the same projected area as a single colloid, making the impact on transmitted light from the aggregation of two chains or the settling of a chain equivalent. Consequently, both aggregation and sedimentation have a similar overall impact. However, since sedimentation should still induce a luminosity gradient, which is not observed in this configuration, we rely on the perpendicular orientation to study the sedimentation itself.

The results for the case where the chains are **perpendicular to the longitudinal axis**, in blue, reveal a gradient in the normalized transmitted light along the sample height. This indicates that sedimentation, rather than aggregation, is the primary mechanism affecting the measurement. Additionally, sedimentation appears to occur significantly slower than aggregation, as observed by comparing both plots.

Following the same reasoning as previously, we first consider colloids homogeneously suspended in the sample. When aggregating into chains, these colloids still block the light in the same manner than before, meaning that this initial aggregation should have **no effect** on the transmitted light, as represented in the first step of the bottom Fig. 6.10. When chains are large enough to settle, the influence of their settling on the transmitted is no longer equivalent to that of further aggregation of multiple chains into one, conversely to the previous configuration. Indeed, settling drastically reduces the projected area covered by the chain, whereas further aggregation does not modify it, as illustrated in the second step of the bottom Fig. 6.10. This reasoning can be confirmed by looking at t close to 0 in Fig. 6.7, where it is clear that $I(t)$ remains null for the lower envelope, translating the **absence of sedimentation**, while it already starts increasing for the upper envelope, **confirming the particles aggregation**.

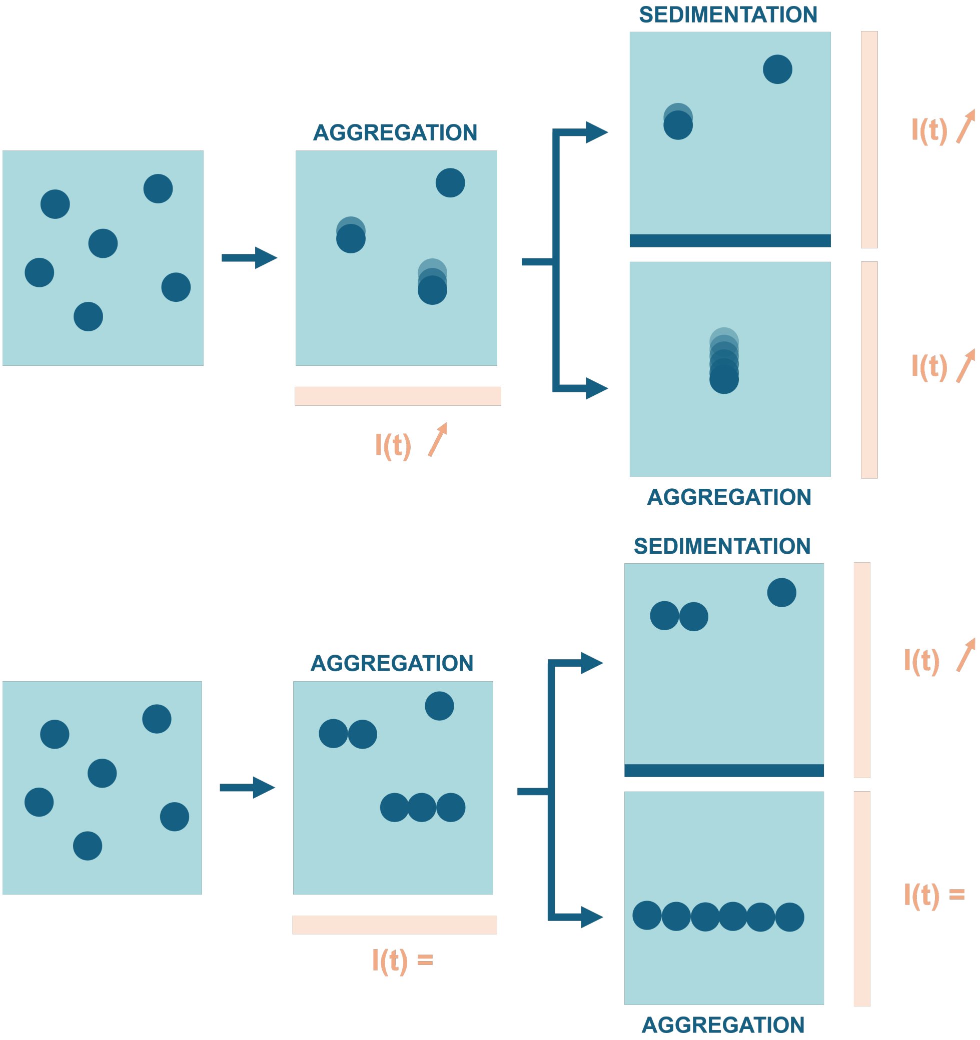

Figure 6.10: Comparison between the parallel configuration (on the top) and the perpendicular configuration (on the bottom). In the parallel configuration, both aggregation and sedimentation lead to an increase of $I(t)$. In the perpendicular configuration, only sedimentation does. In orange, we specify the impact of each stage on the transmitted light.

These results clearly show that **aggregation dominates at the beginning, and sedimentation after the initial clustering**. The same tendencies were observed for frequencies ranging in S_1.

Looking back at the time evolution of $I(t)/I_{max}$ in Fig. 6.7, it is indeed consistent with the hypothesis that the chains first aggregate then settle quickly, leading the suspension to drastically lighten, until saturation is reached. Such systems, where a rapid initial change is followed by a gradual stabilization at a saturation value, can typically be modelled by using an exponential function of the form

$$I(t) = I^*_{max}\left(1 - \mathrm{e}^{-\frac{t}{\tau_s}}\right). \tag{6.1}$$

This modelling allow us to determine a characteristic sedimentation time τ_s and a saturation value I^*_{max}. Fitting it to the upper envelope thus gives us both the saturation value and the characteristic sedimentation time for each rotational frequency. The obtained saturation value is naturally very close to I_{max}, and the resulting characteristic time is plotted against f_B in Fig. 6.11.

These results show that the characteristic sedimentation time increases with f_B, which indicates that the sedimentation speed is greater for smaller rotational frequencies. This is consistent with the expression of $v_{s,N}$ given in Eq. (4.12), that indicates that v_s is greater for longer chains (and the smaller the rotational frequency the longer the chains, as shown in Fig. 3.4 in Section 3.3.2).

However, following Eq. 4.12, $v_{s,N}$ is expected to be proportional to $\ln(N)$. If we approximate that all the chains in the suspension have the same length, hence contains the same number of beads N, corresponding to the maximal length possible at this rotational frequency, and that N is high, then N should scale as $1/\sqrt{\omega}$, from Eq. (3.23). Therefore, v_s should be proportional to $-\frac{1}{2}\ln(\omega)$. Instead, we find that $\tau_s \sim \omega$, meaning that $v_s \sim 1/\omega$. The expression of v_s in Eq. (4.12) thus does not seem well-suited in the context of a sedimentation influenced by magnetic aggregation.

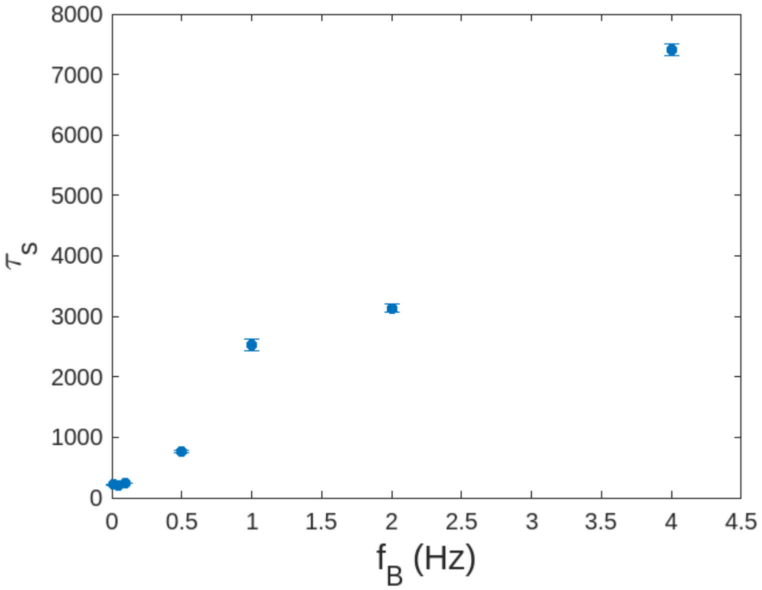

Figure 6.11: Values of τ_s for the S_1 frequency range. The value of τ_s is obtained from the fitted saturating exponential of the upper envelope.

This discrepancy can be due to the fact that this sedimentation speed does not take into account the **”swipe” effec**t. Indeed, it considers only one chain settling in a fluid, while we have actually many chains that can interact with one another. When f_B is small, long chains form and settle faster than smaller ones still aggregating. Doing so, they swipe the space below them, as explained in Section 4.4, resulting in a **faster sedimentation**. The effect of this phenomenon becomes smaller as f_B increases and as the chains length decreases, leading to a longer sedimentation process.

This reasoning is valid because colloids aggregate into chains. Therefore, the behavior of isotropic cluster, such as those observed in S_3 (corresponding to $f_B > 10\,\text{Hz}$), is expected to be drastically different.

SCENARIOS 2 AND 3

As in the no field case in Fig. 6.6 and in the S_1 case in Fig. 6.7, we plotted the normalized transmitted light $I(t)/I_{max}$ against time during a complete sedimentation for $f_B = 10, 20, 30\,\text{Hz}$ in Fig. 6.12, and compared those signal with S_1 as well as S_2 frequencies. Since the sedimentation was significantly longer than in the previous experiments, we were unable to fully reach the saturation before the coils we used began to overheat. However, comparing these results with the ones obtained in other scenarios still allow some conclusions to be drawn. First, we can notice that the sedimentation time increases with the applied frequency, and become closer to the case where no field is applied for $f_B > 20\,\text{Hz}$.

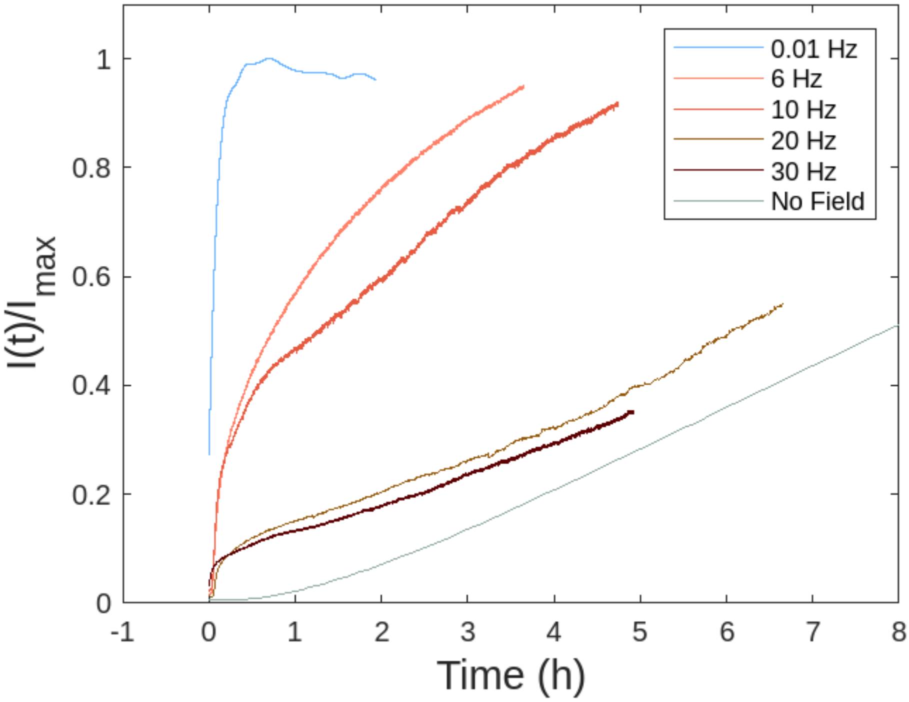

Figure 6.12: $I(t)/I_{max}$ for $f_B = 10\,\text{Hz}$ in orange, $f_B = 20\,\text{Hz}$ in light brown, and $f_B = 30\,\text{Hz}$ in dark brown. They are compared to S_1 with the upper envelope of $f_B = 0.01\,\text{Hz}$ in light blue, to S_2 with $f_B = 6\,\text{Hz}$, and to the case where no field is applied in grey.

Unlike the results in S_1, the frame rate here is insufficient to capture the light variations, which are very small. This makes the discrimination between parallel and perpendicular configurations as well as the use of envelopes irrelevant. As a reminder, we established in Section 6.2.1 that the resulting aggregates were mainly isotropic (i.e disk-like) for S_3 or ribbon-like, instead of chain-like, explaining the small amplitude of the transmitted light variations.

Instead of steadily reaching the saturation, it appears that two different phases occur for frequencies ranging in S_3. During the first one, $I(t)$ quickly increases. Then, the sedimentation slows down, and $I(t)$ continues to increase at a slower rate. There should be of course a last phase, corresponding to the saturation at the end of the sedimentation process. Since the saturation is not captured by our experiments, I_{max} is taken as the maximal gray level in the luminosity profile.

In order to characterize those different steps, we plotted the same profiles as in Fig. 6.9 for the S_2 frequencies. The results for $f_B = 10Hz$ are represented in Fig. 6.13, with a time difference between each frame of 10 min. In the early times of this figure, we can notice a similar behavior to the one occurring when the chains are aligned along the longitudinal axis for f_B in S_1. That is to say that the luminosity profile show no gradient, but instead increases homogeneously across the sample height. After this transient behavior, a light gradient is established, as it was the case for the perpendicular configuration in S_1. As explained before, this indicates that aggregation dominates at first, then, the sedimentation takes the upper hand. In the first phase, we observe the consequences of the first aggregation and the sedimentation of the large aggregates. In the second phase, we rather observe the sedimentation of the aggregates that remains. In S_1, due to the size of the chains and to the consequent swipe effect, we do not observe a second phase.

Looking at the movie of the experiments in Fig. 6.5 (see also [134]) corroborates these hypothesis, as the movements of the aggregates reaching the bottom of the sample in the first times of experimentation are clearly visible. The time during which this phenomenon is observed cor-

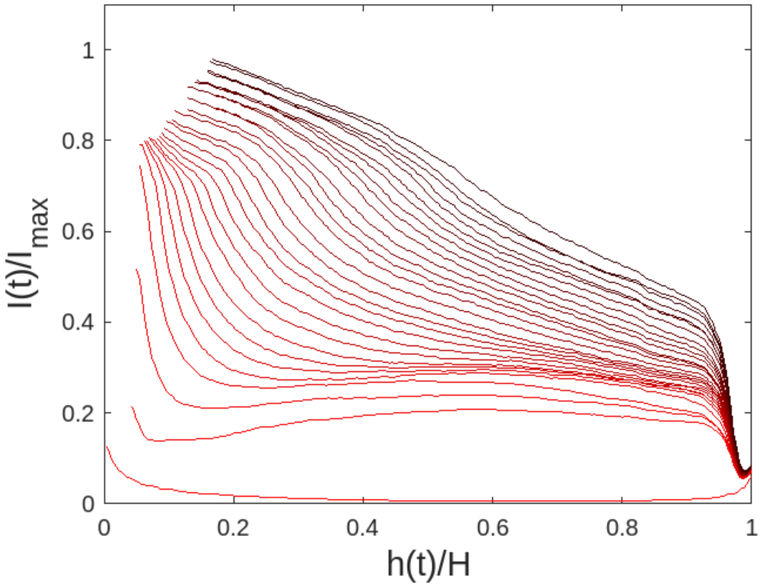

Figure 6.13: $I(t)/I_{max}$ for $f_B = 10\,\text{Hz}$ along the sample height. A profile is plotted every 10 minutes.

respond to the horizontal profiles in Fig. 6.13. This confirms that the first phase of increase in $I(t)$ corresponds both to aggregation and to a quick settling of the resulting aggregates. During the second phase, no movements are observed, and the settling steadily continues, only slower.

Comparing these phases to the observations in S_1, the first seems to match the increase of $I(t)$ for smaller frequencies, since it corresponds both to aggregation and settling of large aggregates. This link between S_1 and S_3 make the comparison between the two scenarios possible. To compare the characteristic time of sedimentation for S_1 and the characteristic time of the first phase for S_3, we fitted the saturating exponential in Eq. 6.1 to the first phase, and a linear function to the second one. The fitting functions are represented in dotted lines in Fig. 6.14 or the upper envelope of $f_B = 0.01\,\text{Hz}$ and the complete signal of $f_B = 10\,\text{Hz}$. The blue dotted line correspond to exponential fit, and the red one the linear fit.

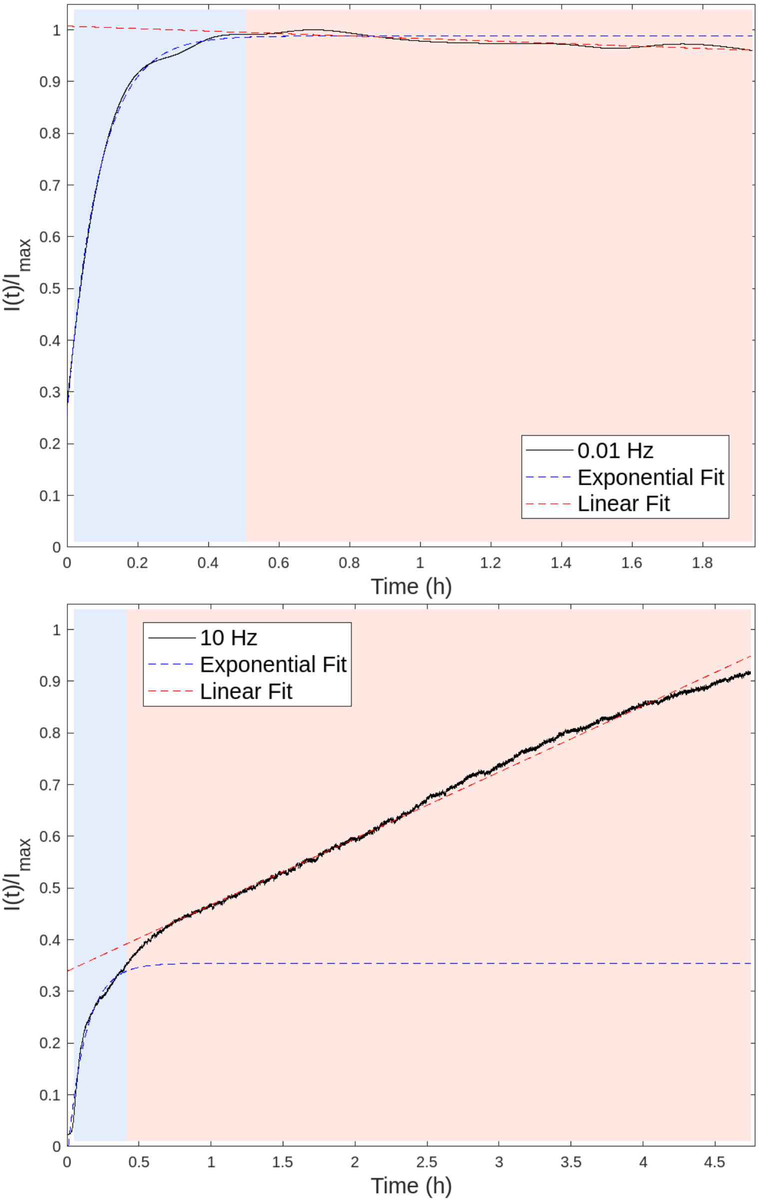

Figure 6.14: Time evolution $I(t)/I_{max}$ for $f_B = 0.01\,\mathrm{Hz}$ on the top (upper envelope), and $f_B = 10\,\mathrm{Hz}$ on the bottom. The background colors matches the fit used for the corresponding time range. In both graph, the blue color denotes the first phase of aggregation and quick settling of the aggregates.

The blue exponential fit correspond to the same phase for S_1 and S_3, but the red linear fit represents the saturation for S_1, and the settling of smaller isolated aggregates or single colloids for S_3. The change point between the two fitting functions is highlighted by the two background colors.

From those fitting functions, we were able to complete the plot of τ_S in Fig. 6.11 with the characteristic time of the first phase for f_B ranging in S_3, denoted τ_1. The results are shown in Fig. 6.15. For S_1, τ_S increases linearly. For S_2 and S_3, τ_1 decreases, and reaches a value equivalent to τ_S for f_B between 0.1 Hz and 1 Hz. It indicates that the large aggregates, while not of the same shape, self-assemble and settle in a similar time in both scenarios. Since the magnetic field amplitude does not change between each scenario, we can conclude from this observation that those aggregates are likely containing the same amount of particles, but in an anisotropic setting in S_1, and in a configuration close to isotropic in S_3.

Concerning the transition, S_2, it should occur at $f_B = 7\,\mathrm{Hz}$ according to the results displayed in Fig. 6.4. This corresponds to the frequency where the chains forming in the sample are no longer following the magnetic field rotation at the same rate. The results shown in Fig. 6.15 confirm this value of transition frequency. Indeed, for $f_B = 6\,\mathrm{Hz}$, the evolution of $I(t)/I_{max}$ with time is quite similar to the one observed for f_B in S_1. On the other hand, for $f_B = 8\,\mathrm{Hz}$, this evolution present the same two phases behavior as for f_B ranging in S_3. The consequent values of τ_S for $f_B = 6\,\mathrm{Hz}$ and τ_1 for $f_B = 8\,\mathrm{Hz}$ are also plotted in Fig. 6.15. We can thus conclude that the three scenarios expected from the 2D results are observed, with the same values of transition f_B between each of them as in the previous chapter.

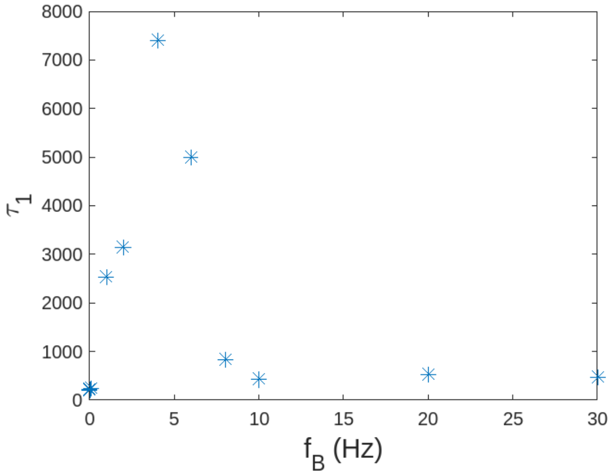

Figure 6.15: Characteristic time obtained from the fitting of a saturating exponential on the first phase of the increase in transmitted light. The results for S_3 and S_2 are added to the results of S_1. The characteristic time τ_1 corresponds to the sedimentation characteristic time τ_s for f_B ranging in S_1.

6.3 Concluding remarks and perspectives

In this chapter, we focused on the **three-dimensional aggregation** of superparamagnetic colloids under the influence of a rotating magnetic field and its impact on the suspension **sedimentation process**. By comparing our findings with the results presented in Chapter 5, we identified notable parallels between the **microscopic structures** observed in the earlier experiments and the **macroscopic effects** revealed in this study. As a main result, we found the sedimentation time to increase with f_B, the rotational frequency of the magnetic field.

To investigate the **3D microscopic structures** formed with the aggregation induced by the magnetic field rotation, we monitored the light transmitted through the sample over short time intervals with a high frame rate. For frequencies such as $f_B \leq 7\,\text{Hz}$, the transmitted light varies **periodically** with time, with a frequency **double** that of f_B. This behavior is similar to the one observed with magnetic nanorods subjected to a rotating magnetic field (see Section 4.3), indicating that the colloids aggregate into **chains** at these frequencies. For $f_B > 7\,\mathrm{Hz}$, the period of light variation **decreases**, showing that while chains still form, they **no longer** rotate synchronously with the magnetic field. Finally, as f_B increases to $30\,\mathrm{Hz}$, the amplitude of the light variations becomes very **small** and **erratic**. This could correspond to a mixture of small chains and disk-like clusters, that might shield the effect of chains rotation on the transmitted light, which would be consistent with the results of Chapter 5. However, this could also be explained by the presence of short and wide ribbons, or by a combination of chains and single colloids.

Given the three distinct frequency regimes identified in our first experiments, we considered separately 3 scenarios, corresponding as well to the frequencies studied in Chapter 5 : S_1 for $f_B \leq 5\,\mathrm{Hz}$, S_2 for $5\,\mathrm{Hz} < f_B < 10\,\mathrm{Hz}$, and S_3 for $f_B \geq 10\,\mathrm{Hz}$. After determining the microscopic structures for each scenario, as described above, we then assessed their impact on **sedimentation**. To achieve this, we captured the entire sedimentation process to the greatest extent possible and compared it to the case where no magnetic field is applied.

For $f_B \leq 5\,\mathrm{Hz}$, or S_1, sedimentation is clearly **faster** compared to the case with no magnetic field, and the light transmitted through the sample follows a **saturating exponential function** (see Eq. 6.1 and Fig. 6.7). Fitting this function to the signal allowed us to define a characteristic time, τ_S, which increases linearly with f_B. This linear relationship appears to contradict the sedimentation speed of a single rod in a viscous fluid, v_S, given by Eq. 4.12. This discrepancy may arise from chains influencing each other's sedimentation, likely through the **swipe effect** described in Section 4.4. Specifically, when chains are longer, they settle faster, and can therefore swipe the smaller chains still forming beneath them. This effect leads to a faster overall settling process, and is more pronounced at lower frequencies. Additionally, we plotted the transmitted light profiles from the top to the bottom of the sample over time in Fig. 6.9, for both the **parallel** and **perpendicular** chain orientations relative to the longitudinal axis.

From these plots, we concluded that aggregation is the predominant mechanism driving the particles initially, with sedimentation taking over after the initial clustering phase.

For $f_B \geq 10\,\mathrm{Hz}$, or S_3, we no longer observe the saturating exponential behavior seen at lower frequencies. Instead, **two distinct phases** emerge, as highlighted in Fig. 6.12. During the first one, the transmitted light **increases rapidly**, and we observe numerous aggregates settling to the bottom of the sample. In the second phase on the other hand, the transmitted light continues to **rise steadily**, but at a much slower rate, similar to the behavior observed when no magnetic field is applied. Looking at the light profiles from top to bottom along time in Fig. 6.13 reveals an initial **rapid aggregation**, followed by **slow sedimentation**. From these results, we infer that the first phase involves the same mechanisms as the entire sedimentation process for smaller f_B, that is to say, fast aggregation followed by sedimentation of large aggregates. This phase can be fitted with a saturating exponential as previously, yielding a **characteristic time** for this phase comparable to the sedimentation times observed for f_B between $0.1\,\mathrm{Hz}$ and $1\,\mathrm{Hz}$. This suggests that the aggregates formed in both frequency ranges may contain a similar number of colloids.

At the transition, $5\,\mathrm{Hz} < f_B < 10\,\mathrm{Hz}$ (or S_2), we observed behaviors characteristic of both frequency ranges described earlier. More precisely, at $f_B = 6\,\mathrm{Hz}$, the signal evolves similarly to what was observed in S_1, while at $f_B = 8\,\mathrm{Hz}$, we rather detect the two-phase behavior detailed for S_3.

These results are consistent to the conclusions of Chapter 5 and suggest that similar microscopic structures form in both 2D and 3D for $f_B \leq 10\,\mathrm{Hz}$. Above this frequency, we cannot formally identify the shape of the aggregates. They may consist of a mixture of chains and disk-like clusters, as in 2D, or a combination of chains and individual colloids. Another possible structure is short, wide ribbons. Nonetheless, we can confirm the presence of structures other than disk-like clusters, wether chains or ribbons, which also aligns with our previous findings.

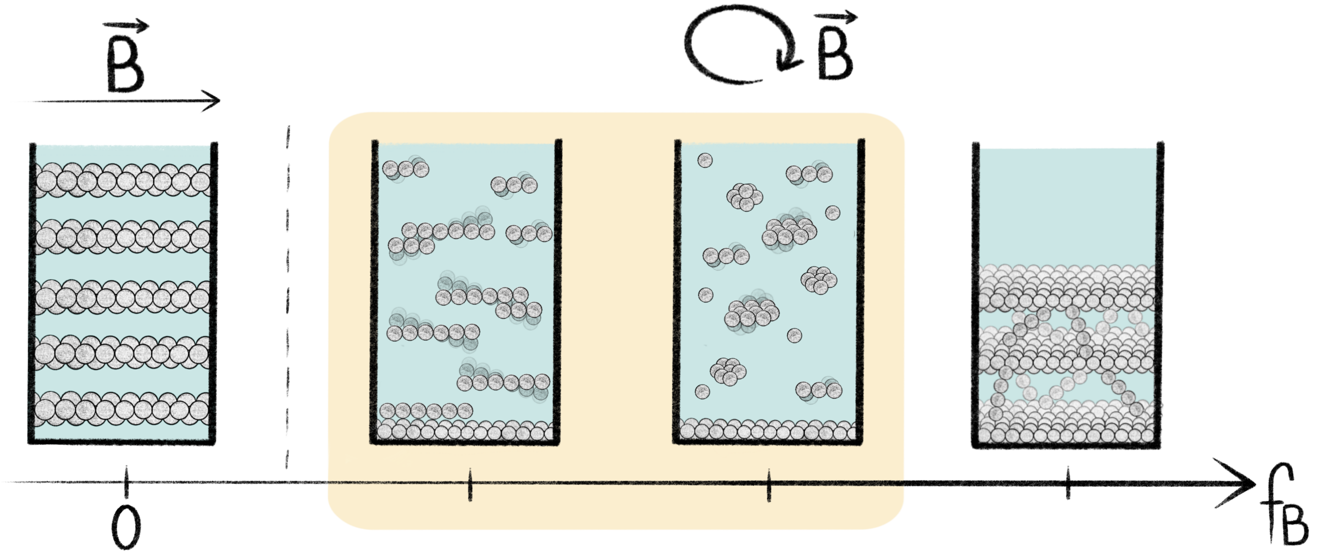

Figure 6.16: Schematic representation of the three-dimensional structures formed in a suspension of superparamagnetic colloids subjected to an external magnetic field $\vec{B}$ confined to the horizontal plane. Structures highlighted in yellow are based on our experimental findings. For frequencies below 10 Hz, chains form in the sample, causing periodic light flashes as they align with the light axis during rotation. The swipe effect, which accelerates sedimentation, is also illustrated. At frequencies above 10 Hz, light flashes appear with reduced amplitude, indicating the presence of chains or ribbons, possibly shielded by single colloids or isotropic clusters. All these structures are depicted together.

Our results are represented in the updated visual summary in Fig. 6.16, which highlights our contribution in light yellow.

However, several questions remain unanswered. While we explored the influence of the magnetic field's rotational frequency, other parameters, such as the colloidal volume fraction discussed in Chapter 5, or the magnetic field amplitude, were not investigated in the context of sedimentation.

Regarding the **volume fraction**, exploring the same experimental range as in the previous chapter could help identify the aggregates that form at $f_B \geq 10\,\mathrm{Hz}$. For example, at $\phi = 5.10^{-4}$, only chains were observed for $f_B = 20\,\mathrm{Hz}$ in 2D, whereas isotropic clusters predominantly formed for $\phi = 3.10^{-3}$ at the same frequency. As a reminder, a volume fraction of 2.10^{-3} was used in the experiments discussed in this chapter. Therefore, identifying the microscopic structures under these conditions could offer valuable insights to the questions still remaining in this chapter.

Similarly, the **magnetic field amplitude** could also influence the aggregated microscopic structures in 3D, as noted in Section 5.5, where it was found to affect the 2D structures as well. Comparing different magnetic field amplitudes with those used in this chapter could better our understanding of the underlying mechanisms.

Overall, **any modifications to the experimental conditions** that would alter the aggregated microscopic structures may potentially impact the sedimentation process and provide deeper insights into the observations presented in this chapter.

Finally, an unexplored aspect of the results is the **fluid flux** through the sample that may be induced by the movement of the aggregates. For instance, at f_B within S_3, the initial collective movement of aggregates towards the bottom of the sample suggests the formation of a convection cell. Such fluid flux could be driven by both interactions with the container walls [135, 136] and hydrodynamic interactions among the aggregating or settling microstructures [137, 138]. This phenomenon could be further investigated using Particle Image Velocimetry, which would enable tracking the particles throughout the sedimentation process.

7

The Final Act

Concluding insights and future prospects

As we conclude this thesis, it's worth reflecting again on the theme we began with. From the moment we wake up, through the many tools that shape our day, we manifest a constant desire to extend our abilities, simplify tasks, and push the boundaries of what we can achieve. Likewise, the subject of this thesis centers on a powerful yet microscopic set of tools: superparamagnetic colloids. Though far from the everyday tools we interact with, these tiny particles have the potential to transform fields such as medicine, environmental science, and engineering.

Just as tools have evolved from simple stone axes to advanced robotics and nanotechnology, **superparamagnetic colloids** open a wide range of opportunities to control and harness microscopic systems. These particles, manipulated by different types of external magnetic fields, exhibit both **self-assembly** and **locomotion** at scales too small for the naked eye. What we have explored in this thesis is a snapshot of the next generation of tools that may one day operate autonomously in our bodies or in remote, hazardous environments, continuing humanity's long tradition of extending our reach and capabilities.

To understand the nature and relevance of superparamagnetic colloids, we began by exploring the concepts of **magnets** and **magnetic fluids**, drawing comparisons with **ferrofluids** in Chapter 2. Both ferrofluids and superparamagnetic colloids consist of magnetic particles suspended in a fluid, often oils for ferrofluids and water for colloids, and rely on thermal agitation to maintain zero magnetization when no external magnetic field is applied. The key difference is that ferrofluid particles are **permanent** magnets on the **nanometer** scale, while superparamagnetic particles are **non-permanen**t magnets on the **micrometer** scale. This non-permanent nature means that superparamagnetic colloids do not exhibit magnetic interactions in the absence of an external magnetic field, which can be advantageous for developing specific applications, such as water depollution.

Then, in Chapter 3, we explored the **self-assembly** of superparamagnetic colloids under the influence of constant and rotating magnetic fields, focusing on **two-dimensional** systems. When subjected to a constant magnetic field, the particles aggregate into **chains** aligned with the field. Under a slowly rotating magnetic field, with a frequency below 1 Hz, these chains **rotate** along with the field, at the same rate. As the frequency increases, the viscous drag on the particles causes the chains to **break** into shorter segments, and for higher frequencies, the magnetic interactions become isotropic, leading to the formation of **disk-like clusters** instead.

Under the influence of a rotating magnetic field, the aggregation process is influenced by both **magnetic** and **hydrodynamic** interactions. The former govern the formation of chains and clusters, while the latter drive chains breakup, enhance the aggregation of disk-like clusters, and induce their rotation. These results highlight how the characteristics of the magnetic field, particularly its **rotational frequency** f_B, dictate the structural transitions and dynamics of colloidal aggregates.

Given the importance of the rotational frequency f_B in the aggregation process, we investigated its influence by conducting **experiments** in a **quasi-2D** suspension. During these experiments, detailed in Chapter 5, we focused on the the **early stages** of colloid clustering, which had yet to be unraveled. We discovered that, contrary to expectations, **colloids initially form chains** even at frequencies where disk-like clusters are anticipated ($f_B \geq 10\,\mathrm{Hz}$). These chains interact and eventually transition into disk-like clusters, adding a new step to the existing model of cluster formation for numerous particles. To quantify this transition, we introduced a **model** based on cluster circularity, allowing us to track the proportion of chains and disk-like clusters over time and to identify a critical time for the formation of disk-like clusters, which decreases with f_B. Alongside with the influence of magnetic field rotational frequency, we also investigated the impact of colloidal **volume fraction**, showing that at the same frequency, a lower volume fraction foster chain formation, while its the opposite for larger volume fraction.

Our results offer new insights into the **dynamics of clustering** in rotating magnetic fields and highlight the importance of further studying the impact of other parameters, such as the magnetic field amplitude. These findings not only advance our understanding of colloidal aggregation in simple systems, but also pave the way for future investigations into more complex scenarios, such as coupling magnetic fields with other forces or using anisotropic colloids.

After investigating the microscopic structures in quasi-2D suspensions, we shifted our focus to **three-dimensional systems** in Chapter 4, where aggregation could have a macroscopic impact, particularly on **sedimentation**. To approach this matter, we compiled current knowledge on 3D aggregation of magnetic colloids, following the same reasoning applied for the 2D case and beginning with a constant magnetic field. In this scenario, **columns** form instead of chains, but they remain oriented along the magnetic field. For a rotating field, when the frequency is sufficiently high, the interaction potential becomes isotropic, much like in the 2D case. This leads to the layering of the suspension, forming **large interconnect sheets**. It is conceivable that, at lower frequencies, layering might not occur, and instead, rotating chains or columns may form. This would be analogous to systems where magnetic nanorods rotate in response to the field, causing periodic variations in the light transmitted through the sample. Observing such light variations experimentally would thus support the hypothesis of rotating chains.

Examining the macroscopic effects of these microscopic structures, we discussed two possible types of sedimentation process. The first, termed *cluster deposition*, involves the colloids aggregating into discrete clusters that settle individually, resulting in a **diffuse sedimentation front**. The second, referred to as *collective settling*, occurs when colloids form a networked gel structure that settles as a cohesive unit, producing a **sharp sedimentation front**. By looking at the sedimentation front, we can thus expect to identify the settling regime. An open question that remains is how aggregation influences sedimentation, and more specifically, what role the microscopic structures aggregating in the suspension play in this process.

We tackled this question in Chapter 6 by observing experimentally the sedimentation of suspensions subjected to a rotating magnetic field in the horizontal plane, for a range of rotation frequencies. Right away, we found that the sedimentation front was diffuse in all of our experiments, indicating that colloids aggregate into **individual clusters** that then settle.

Next, we used high-frame-rate light transmission measures to identify the microscopic structures aggregating within the sample, as direct observation through a microscope was not feasible in this configuration. These experiments revealed **three distinct frequency regimes**. In the first regime, corresponding to $f_B \leq 5\,\mathrm{Hz}$, we observed light flashes with a period double that of the magnetic field. This indicates that **chains** are rotating in the sample **at the same rate** as the magnetic field. In the second regime, spanning $5\,\mathrm{Hz} < f_B < 10\,\mathrm{Hz}$, the period of the light flashes decreased, showing that the chains **no longer follow** the magnetic field rotation precisely. In the final regime, $f_B \geq 10\,\mathrm{Hz}$, the amplitude of light variations became very small and erratic, suggesting the formation of either **fewer chains** or larger, shorter **ribbons**, potentially shielded by single colloids or **isotropic clusters**. These observations align with the results of Chapter 5, suggesting that similar microscopic structures form in 2D and 3D.

Following the identification of these microscopic structures, we studied their impact on the sedimentation process. We found that **lower magnetic field rotation** frequencies correspond to **faster sedimentation**. We attribute this to the presence of longer chains at lower frequencies, which settle more quickly. Additionally, the **swipe effect**, where longer chains settle faster and displace smaller, still-aggregating chains underneath, further accelerates sedimentation. We finally observed a **two-phase** sedimentation process for frequencies above 10 Hz: initially, a rapid aggregation and settling of large aggregates, followed by a slower settling phase for the remaining smaller aggregates or single colloids, which does not occur at lower frequencies.

Our findings in 3D align well with the structures brought to light by our 2D results, which improves our understanding of how microscopic structures influence macroscopic phenomena like sedimentation. They are summarized in the card annexed to this thesis, with our contribution highlighted in yellow. Looking ahead, future research could explore how other variables such as colloidal volume fraction or magnetic field amplitude impact the sedimentation, as we showed that both of these parameters influenced the structure forming in two dimensions. More broadly, any parameter that affects the aggregating microscopic structures will also impact the sedimentation process, such as the colloids shape or the coupling of the magnetic field with other external fields. Ultimately, the scope for further exploration is vast, limited only by our creativity and technological advancements.

While our experiments consistently showed a **diffuse** sedimentation front, there is room to explore the possibility of transitioning to a **sharp** sedimentation interface at higher magnetic field rotational frequencies. Such a transition would signify that colloids aggregate into large, interconnected sheets, potentially altering sedimentation dynamics significantly as well as the sedimentation time. This shift from cluster deposition to collective settling would also be influenced by factors like volume fraction and magnetic field amplitude, and could potentially allow to **transform a homogeneous suspension** into a **gel-like structure** using only an external field.

Additionally, we examined sedimentation under a magnetic field in the horizontal plane. However, flipping the field to the **vertical plane** could introduce significant effects due to gravity, influencing both the microscopic structure formation and the sedimentation process itself in novel ways.

While these considerations may seem distant from our initial focus on microscopic robots, it is crucial to remember that understanding the interactions and aggregation of superparamagnetic colloids is fundamental to their development. These particles are not just the **building blocks** of micrometric robots but also their **driving force**, controlled by external fields. By comprehending how they interact and self-assemble in various configurations, we pave the way for designing **versatile self-constituting** robots tailored to specific tasks. Do we need to swim in a viscous environment, deliver drugs to targeted cells, capture and retrieve pollutants from water, or mix hazardous fluids? Each of these scenario demands a specific form of self-assembly and control, which requires to first address foundational configurations that will serve as a **baseline** for further, more complex layouts. **This thesis aimed to establish this foundation, and I hope it has not only achieved that goal but also provided an engaging overview of the wonders we can achieve thanks to superparamagnetic colloids.**

Bibliography

[1] D. Cahen et al. “Stone tools, toolkits, and human behavior in prehistory”, *Current Anthropology* 20, 1979.

[2] T. Wynn. “Piaget, stone tools and the evolution of human intelligence”, *World archaeology* 17, 1985.

[3] J. Zhang et al. “Oldest playable musical instruments found at Jiahu early Neolithic site in China”, *Nature* 401, 1999.

[4] Isaac Asimov. *I, robot.* Vol. 1. Spectra, 2004.

[5] R. Bogue. “Exoskeletons and robotic prosthetics: a review of recent developments”, *Industrial Robot: an international journal* 36, 2009.

[6] V. Mendez et al. “Current solutions and future trends for robotic prosthetic hands”, *Annual Review of Control, Robotics, and Autonomous Systems* 4, 2021.

[7] D. Babu et al. “Holding, grasping and sensing of prosthetic robot arm like a real human hand, a journey beyond limits: an extensive review”, *Human-Centered Technology for a Better Tomorrow: Proceedings*, 2022.

[8] U. Kim et al. “Integrated linkage-driven dexterous anthropomorphic robotic hand”, *Nature communications* 12, 2021.

[9] U. Saranli, M. Buehler, and D.E. Koditschek. “RHex: A simple and highly mobile hexapod robot”, *The International Journal of Robotics Research* 20, 2001.

[10] S. Kim, J.E. Clark, and M.R. Cutkosky. “iSprawl: Design and tuning for high-speed autonomous open-loop running”, *The International Journal of Robotics Research* 25, 2006.

[11] D. Santos et al. “Gecko-inspired climbing behaviors on vertical and overhanging surfaces”. In: *2008 IEEE International Conference on Robotics and Automation.* 2008, pp. 1125–1131.

[12] S. Coyle et al. “Bio-inspired soft robotics: Material selection, actuation, and design”, *Extreme Mechanics Letters* 22, 2018.

[13] J. Cornejo et al. “Bio-inspired design of hard-bodied mobile robots based on arthropod morphologies: a 10-year systematic review and bibliometric analysis”, *Bioinspiration & Biomimetics*, 2024.

[14] M. De Manabendra et al. “Bio-inspired flapping wing aerodynamics: a review”, *Journal of the Indian Institute of Science*, 2024.

[15] S. Palagi and P. Fischer. “Bioinspired microrobots”, *Nature Reviews Materials* 3, 2018.

[16] L. Zhang et al. “Artificial bacterial flagella: Fabrication and magnetic control”, *Applied Physics Letters* 94, 2009.

[17] Y. Collard, G. Grosjean, and N. Vandewalle. “Magnetically powered metachronal waves induce locomotion in self-assemblies”, *Communications Physics* 3, 2020.

[18] C. Mavroidis and A. Ferreira. “Nanorobotics: past, present, and future”. In: *Nanorobotics: current approaches and techniques*. Springer, 2012, pp. 3–27.

[19] M. Sun et al. “Bioinspired self-assembled colloidal collectives drifting in three dimensions underwater”, *Science Advances* 9, 2023.

[20] H. Huang et al. “3D Motion Manipulation for Micro-and Nanomachines: Progress and Future Directions”, *Advanced Materials* 36, 2024.

[21] S. Klumpp et al. “Swimming with magnets: from biological organisms to synthetic devices”, *Physics Reports* 789, 2019.

[22] T. Yang et al. “Reconfigurable microbots folded from simple colloidal chains”, *Proceedings of the National Academy of Sciences* 117, 2020.

[23] I.K. Ogemdi. “Properties and uses of colloids: a review”, *Colloid and Surface Science* 4, 2019.

[24] A. Spatafora-Salazar et al. “Hierarchical assemblies of superparamagnetic colloids in time-varying magnetic fields”, *Soft Matter* 17, 2021.

[25] V. Liljeström et al. “Active structuring of colloids through field-driven self-assembly”, *Current Opinion in Colloid & Interface Science* 40, 2019.

[26] A. Vázquez-Quesada, T. Franke, and M. Ellero. “Theory and simulation of the dynamics, deformation, and breakup of a chain of superparamagnetic beads under a rotating magnetic field”, *Physics of fluids (1994)* 29, 2017.

[27] J. Faraudo et al. “Predicting the Self-Assembly of Superparamagnetic Colloids under Magnetic Fields”, *Advanced Functional Materials* 26, 2016.

[28] K.J.M. Bishop, S.L. Biswal, and B. Bharti. “Active colloids as models, materials, and machines”, *Annual Review of Chemical and Biomolecular Engineering* 14, 2023.

[29] K. Han. “Electric and magnetic field-driven dynamic structuring for smart functional devices”, *Micromachines* 14, 2023.

[30] D. Jin and L. Zhang. “Collective behaviors of magnetic active matter: recent progress toward reconfigurable, adaptive, and multifunctional swarming micro/nanorobots”, *Accounts of Chemical Research* 55, 2021.

[31] J. Law et al. “Micro/nanorobotic swarms: from fundamentals to functionalities”, *ACS nano* 17, 2023.

[32] B. Rohrig. “The Mesmerizing Pull of Ferrofluids”, *ChemMatters* 2021, 2021.

[33] M. Kole and S. Khandekar. “Engineering applications of ferrofluids: A review”, *Journal of Magnetism and Magnetic Materials* 537, 2021.

[34] D. Susan-Resiga and L. Vekas. “From high magnetization ferrofluids to nano-micro composite magnetorheological fluids: properties and applications”, *Rom. Rep. Phys* 70, 2018.

[35] W. Yang et al. “Systematic analysis of ferrofluid: a visualization review, advances engineering applications, and challenges”, *Journal of Nanoparticle Research* 24, 2022.

[36] Y. Zhang et al. “A comparative study of ferrofluid seal and magnetorheological fluid seal”, *IEEE Transactions on Magnetics* 54, 2018.

[37] C. Scherer and A.M. Figueiredo Neto. “Ferrofluids: properties and applications”, *Brazilian journal of physics* 35, 2005.

[38] S. Genc and B. Derin. “Synthesis and rheology of ferrofluids: a review”, *Current Opinion in Chemical Engineering* 3, 2014.

[39] D.Y. Borin et al. “Magnetoviscous effect in ferrofluids with different dispersion media”, *Journal of Magnetism and Magnetic Materials* 416, 2016.

[40] A. Darras et al. “Superparamagnetic colloids in viscous fluids”, *Scientific reports* 7, 2017.

[41] R.E. Rosensweig. *Ferrohydrodynamics.* Courier Corporation, 1997.

[42] K. Seleznyova, M. Strugatsky, and J. Kliava. “Modelling the magnetic dipole”, *European Journal of Physics* 37, 2016.

[43] J. Philip. “Magnetic nanofluids (Ferrofluids): Recent advances, applications, challenges, and future directions”, *Advances in Colloid and Interface Science* 311, 2023.

[44] F. Babick. *Suspensions of colloidal particles and aggregates.* Vol. 20. Springer, 2016.

[45] D.H. Everett. *Basic principles of colloid science.* Royal society of chemistry, 2007.

[46] B.V. Derjaguin, N.V. Churaev, and V.M. Muller. “The Derjaguin—Landau—Verwey—Overbeek (DLVO) theory of stability of lyophobic colloids”, *Surface forces*, 1987.

[47] I. Medvedeva et al. “Sedimentation and aggregation of magnetite nanoparticles in water by a gradient magnetic field”, *Journal of nanoparticle research* 15, 2013.

[48] J. Faraudo and J. Camacho. “Cooperative magnetophoresis of superparamagnetic colloids: theoretical aspects”, *Colloid and polymer science* 288, 2010.

[49] C. Mikkelsen, M. F. Hansen, and H. Bruus. “Theoretical comparison of magnetic and hydrodynamic interactions between magnetically tagged particles in microfluidic systems”, *Journal of Magnetism and Magnetic Materials* 293, 2005.

[50] M. Huysmans and A. Dassargues. “Review of the use of Péclet numbers to determine the relative importance of advection and diffusion in low permeability environments”, *Hydrogeology Journal* 13, 2005.

[51] C.T. Yavuz et al. “Magnetic separations: From steel plants to biotechnology”, *Chemical Engineering Science* 64, 2009.

[52] C.T. Yavuz et al. “Low-field magnetic separation of monodisperse Fe3O4 nanocrystals”, *science* 314, 2006.

[53] T. Franke et al. “Magneto-mechanical mixing and manipulation of picoliter volumes in vesicles”, *Lab Chip* 9, 2009.

[54] J.T Lee et al. “Superparamagnetic particle dynamics and mixing in a rotating capillary tube with a stationary magnetic field”, *Microfluidics and Nanofluidics* 13, 2012.

[55] F. Wittbracht et al. “Enhanced fluid mixing and separation of magnetic bead agglomerates based on dipolar interaction in rotating magnetic fields”, *Applied physics letters* 100, 2012.

[56] R. Dreyfus et al. “Microscopic artificial swimmers”, *Nature* 437, 2005.

[57] F. Martinez-Pedrero et al. “Colloidal Microworms Propelling via a Cooperative Hydrodynamic Conveyor Belt”, *Phys. Rev. Lett.* 115, 2015.

[58] P.J. Vach et al. “Pattern formation and collective effects in populations of magnetic microswimmers”, *Journal of physics. D, Applied physics* 50, 2017.

[59] D. Ahmed et al. “Neutrophil-inspired propulsion in a combined acoustic and magnetic field”, *Nature communications* 8, 2017.

[60] F. Wittbracht et al. “On the direct employment of dipolar particle interaction in microfluidic systems”, *Microfluidics and nanofluidics* 13, 2012.

[61] A. Darras. “Evaporation of superparamagnetic colloids”, *Bulletin de la Société Royale des Sciences de Liège*, 2021.

[62] J.H.E Promislow, A.P Gast, and M. Fermigier. “Aggregation kinetics of paramagnetic colloidal particles”, *The Journal of chemical physics* 102, 1995.

[63] A. Darras et al. “Ribbons of superparamagnetic colloids in magnetic field”, *The European Physical Journal E* 39, 2016.

[64] F. Martinez-Pedrero et al. “Kinetic study of coupled field-induced aggregation and sedimentation processes arising in magnetic fluids”, *Physical Review E—Statistical, Nonlinear, and Soft Matter Physics* 78, 2008.

[65] J.S. Andreu, J. Camacho, and J. Faraudo. “Aggregation of superparamagnetic colloids in magnetic fields: the quest for the equilibrium state”, *Soft Matter* 7, 2011.

[66] I. Petousis et al. “Transient behaviour of magnetic micro-bead chains rotating in a fluid by external fields”, *Lab Chip* 7, 2007.

[67] S. Melle and J.E. Martin. “Chain model of a magnetorheological suspension in a rotating field”, *The Journal of chemical physics* 118, 2003.

[68] Y. Gao et al. “Numerical and experimental study of a rotating magnetic particle chain in a viscous fluid”, *Physical review. E, Statistical, nonlinear, and soft matter physics* 86, 2012.

[69] A.K. Vuppu, A.A. Garcia, and M.A Hayes. “Video Microscopy of Dynamically Aggregated Paramagnetic Particle Chains in an Applied Rotating Magnetic Field”, *Langmuir* 19, 2003.

[70] S. Melle et al. “Polarizable particle aggregation under rotating magnetic fields using scattering dichroism”, *Journal of Colloid and Interface Science* 247, 2002.

[71] S.L. Biswal and A.P. Gast. “Rotational dynamics of semiflexible paramagnetic particle chains”, *Physical Review E—Statistical, Nonlinear, and Soft Matter Physics* 69, 2004.

[72] M. Doi and S.F.F Edwards. *The theory of polymer dynamics.* Vol. 73. oxford university press, 1988.

[73] S. Jäger, H. Schmidle, and S.H.L. Klapp. “Nonequilibrium condensation and coarsening of field-driven dipolar colloids”, *Physical review. E, Statistical, nonlinear, and soft matter physics* 86, 2012.

[74] S. Jäger, H. Stark, and S.H.L. Klapp. “Dynamics of cluster formation in driven magnetic colloids dispersed on a monolayer”, *Journal of physics. Condensed matter* 25, 2013.

[75] Y. Nagaoka, H. Morimoto, and T. Maekawa. “Dynamics of disklike clusters formed in a magnetorheological fluid under a rotational magnetic field”, *Physical review. E, Statistical, nonlinear, and soft matter physics* 71, 2005.

[76] J. Yan, S.C. Bae, and S. Granick. “Rotating crystals of magnetic Janus colloids”, *Soft Matter* 11, 2015.

[77] E. Hilou et al. “Interfacial energetics of two-dimensional colloidal clusters generated with a tunable anharmonic interaction potential”, *Physical Review Materials* 2, 2018.

[78] S. Melle et al. “Microstructure evolution in magnetorheological suspensions governed by Mason number”, *Physical review. E, Statistical, nonlinear, and soft matter physics* 68, 2003.

[79] H. Abdi et al. “Paramagnetic colloids: Chaotic routes to clusters and molecules”, *Physical review. E* 97, 2018.

[80] J.E. Martin, R.A. Anderson, and C.P. Tigges. “Simulation of the athermal coarsening of composites structured by a uniaxial field”, *The Journal of chemical physics* 108, 1998.

[81] J.E Martin, R.A. Anderson, and C.P. Tigges. “Simulation of the athermal coarsening of composites structured by a biaxial field”, *The Journal of chemical physics* 108, 1998.

[82] J.E. Martin, R.A. Anderson, and C.P. Tigges. “Thermal coarsening of uniaxial and biaxial field-structured composites”, *The Journal of chemical physics* 110, 1999.

[83] T. Chen, R.N. Zitter, and R. Tao. “Laser diffraction determination of the crystalline structure of an electrorheological fluid”, *Physical review letters* 68, 1992.

[84] T.C. Halsey and J.E. Martin. “Electrorheological fluids”, *Scientific American* 269, 1993.

[85] W.M. Winslow. “Induced fibration of suspensions”, *Journal of applied physics* 20, 1949.

[86] J.E. Martin, J. Odinek, and T.C. Halsey. “Evolution of structure in a quiescent electrorheological fluid”, *Physical review letters* 69, 1992.

[87] G. Bossis and A. Cebers. “Effects of the magnetodipolar interactions in the alternating magnetic fields”, *Journal of magnetism and magnetic materials* 201, 1999.

[88] O. Volkova et al. “Flow-induced structures in magnetorheological suspensions”, *Journal of magnetism and magnetic materials* 201, 1999.

[89] F. Smallenburg and M. Dijkstra. “Phase diagram of colloidal spheres in a biaxial electric or magnetic field”, *The Journal of chemical physics* 132, 2010.

[90] S. Jäger and S.H.L. Klapp. “Pattern formation of dipolar colloids in rotating fields: layering and synchronization”, *Soft Matter* 7, 2011.

[91] V.V. Murashov and G.N. Patey. “Structure formation in dipolar fluids driven by rotating fields”, *The Journal of Chemical Physics* 112, 2000.

[92] T. Klein et al. “Magnetic-field-dependent optical transmission of nickel nanorod colloidal dispersions”, *Journal of Applied Physics* 106, 2009.

[93] M. Gratz and A. Tschöpe. “Optical transmission versus ac magnetization measurements for monitoring colloidal Ni nanorod rotational dynamics”, *Journal of Physics D: Applied Physics* 50, 2016.

[94] G. Korneva et al. “Carbon nanotubes loaded with magnetic particles”, *Nano letters* 5, 2005.

[95] A. Tokarev et al. “Multifunctional magnetic rotator for micro and nanorheological studies”, *Review of Scientific Instruments* 83, 2012.

[96] P. Aprelev et al. “Synthesis and characterization of nanorods for magnetic rotational spectroscopy”, *Journal of Applied Physics* 118, 2015.

[97] A. Günther et al. “Rotational diffusion of magnetic nickel nanorods in colloidal dispersions”, *Journal of Physics: Condensed Matter* 23, 2011.

[98] T. Yoshida et al. “Magnetic fluid dynamics in a rotating magnetic field”, *Journal of Applied Physics* 111, 2012.

[99] S. Schrittwieser et al. “Direct protein detection in the sample solution by monitoring rotational dynamics of nickel nanorods”, *Small* 10, 2014.

[100] C. Allain, M. Cloitre, and M. Wafra. “Aggregation and sedimentation in colloidal suspensions”, *Physical review letters* 74, 1995.

[101] M.L. Broide and R.J. Cohen. “Experimental evidence of dynamic scaling in colloidal aggregation”, *Physical review letters* 64, 1990.

[102] A. Darras et al. “Erythrocyte sedimentation: collapse of a high-volume-fraction soft-particle gel”, *Physical Review Letters* 128, 2022.

[103] S. Manley et al. “Gravitational collapse of colloidal gels”, *Physical review letters* 94, 2005.

[104] Y. Li et al. “Impact of granular inclusions on the phase behavior of colloidal gels”, *Soft Matter* 19, 2023.

[105] A.K. Dasanna et al. “Erythrocyte sedimentation: Effect of aggregation energy on gel structure during collapse”, *Physical Review E* 105, 2022.

[106] J.R. Weeks, J.S. van Duijneveldt, and B. Vincent. “Formation and collapse of gels of sterically stabilized colloidal particles”, *Journal of Physics: Condensed Matter* 12, 2000.

[107] J.L.C. Domingos, E.A. de Freitas, and W.P. Ferreira. “Steady states of non-axial dipolar rods driven by rotating fields”, *Soft Matter* 16, 2020.

[108] J. Jezek and S.A. Gilder. “Competition of magnetic and hydrodynamic forces on ellipsoidal particles under shear: Influence of the Earth’s magnetic field on particle alignment in viscous media”, *Journal of Geophysical Research: Solid Earth* 111, 2006.

[109] R. Zwanzig. “Hydrodynamic fluctuations and Stokes’ law friction”, *J. Res. Natl. Bur. Std.(US) B* 68, 1964.

[110] G.K. Batchelor. “Sedimentation in a dilute dispersion of spheres”, *Journal of fluid mechanics* 52, 1972.

[111] K. Zahn, R. Lenke, and G. Maret. “Friction coefficient of rod-like chains of spheres at very low Reynolds numbers. I. Experiment”, *Journal de Physique II* 4, 1994.

[112] L.N. Donselaar and A.P. Philipse. “Interactions between silica colloids with magnetite cores: diffusion, sedimentation and light scattering”, *Journal of colloid and interface science* 212, 1999.

[113] S.F Maramizonouz and S. Nadimi. “Drag force acting on ellipsoidal particles with different shape characteristics”, *Powder Technology* 412, 2022.

[114] H. Kim et al. “Controlled uniform coating from the interplay of Marangoni flows and surface-adsorbed macromolecules”, *Physical review letters* 116, 2016.

[115] A. Darras et al. “Effect of volume fraction on chains of superparamagnetic colloids at equilibrium”, *The European physical journal. E, Soft matter and biological physics* 42, 2019.

[116] F. Mignolet. *Transition From Chains to Disks at 10 Hz.* 2024. URL: `https://zenodo.org/search?q=metadata.creators.person_or_org.name%3A%22Florence%2C%20Mignolet%22&l=list&p=1&s=10&sort=bestmatch`.

[117] D. Levesque and J.J. Weis. “Orientational and structural order in strongly interacting dipolar hard spheres”, *Physical Review E* 49, 1994.

[118] A. Ghazali and J-C Lévy. “Two-dimensional arrangements of magnetic nanoparticles”, *Physical Review B* 67, 2003.

[119] A. Weddemann et al. “Magnetic Field Induced Assembly of Highly Ordered Two-Dimensional Particle Arrays”, *Langmuir* 26, 2010.

[120] Z.Q. Yue and I. Morin. “Digital image processing for aggregate orientation in asphalt concrete mixtures”, *Canadian Journal of Civil Engineering* 23, 1996.

[121] W.H. Walton. “Feret‘s statistical diameter as a measure of particle size”, *Nature* 162, 1948.

[122] B. Bharti et al. “Multidirectional colloidal assembly in concurrent electric and magnetic fields”, *Soft Matter* 12, 2016.

[123] A.F. Demirörs, P.J. Beltramo, and H.R. Vutukuri. “Colloidal Switches by Electric and Magnetic Fields”, *ACS Applied Materials & Interfaces* 9, 2017.

[124] Y. Yang et al. “Assembly of Colloidal Molecules, Polymers, and Crystals in Acoustic and Magnetic Fields”, *Advanced materials (Weinheim)* 27, 2015.

[125] M. Driscoll et al. “Unstable fronts and motile structures formed by microrollers”, *Nature physics* 13, 2017.

[126] B. Yigit, Y. Alapan, and M. Sitti. “Cohesive self-organization of mobile microrobotic swarms”, *Soft Matter* 16, 2020.

[127] G. Kokot and A. Snezhko. “Manipulation of emergent vortices in swarms of magnetic rollers”, *Nature communications* 9, 2018.

[128] T. Mohorič et al. “Dynamic Assembly of Magnetic Colloidal Vortices”, *Langmuir* 32, 2016.

[129] H. Kim et al. “Structural coarsening of magnetic ellipsoid particle suspensions driven in toggled fields”, *Journal of physics. D, Applied physics* 52, 2019.

[130] M. Abbas and G. Bossis. “Separation of two attractive ferromagnetic ellipsoidal particles by hydrodynamic interactions under alternating magnetic field”, *Physical review. E* 95, 2017.

[131] J. Baudry et al. “Chiral colloidal clusters”, *Nature* 455, 2008.

[132] A.A. Pal et al. “Anomalous Dynamics of Magnetic Anisotropic Colloids Studied by XPCS”, *Small* 14, 2018.

[133] F. Mignolet. *Transmitted Light Variations at 1 Hz.* 2024. URL: `https://zenodo.org/search?q=metadata.creators.person_or_org.name%3A%22Florence%2C%20Mignolet%22&l=list&p=1&s=10&sort=bestmatch`.

[134] F. Mignolet. *First Aggregation and Settling at 10 Hz.* 2024. URL: `https://zenodo.org/search?q=metadata.creators.person_or_org.name%3A%22Florence%2C%20Mignolet%22&l=list&p=1&s=10&sort=bestmatch`.

[135] C.W.J. Beenakker and P. Mazur. “Is sedimentation container-shape dependent?”, *The Physics of fluids (1958)* 28, 1985.

[136] E.M. Tory, M.T. Kamel, and C.F. Chan Man Fong. “Sedimentation is container-size dependent”, *Powder Technology* 73, 1992.

[137] N. Goyal and J.J. Derksen. “Direct simulations of spherical particles sedimenting in viscoelastic fluids”, *Journal of Non-Newtonian Fluid Mechanics* 183-184, 2012.

[138] E. Guazzelli and J. Hinch. “Fluctuations and Instability in Sedimentation”, *Annual Review of Fluid Mechanics* 43, 2011.